Two-Dimensional Modeling of a Klystron Traveling-Wave-Type Output Structure and its Empirical Justification

Hiroshi Tsutsui

Department of Accelerator Science
School of Mathematical and Physical Science
The Graduate University for Advanced Studies

1999

Contents

List of Figures

List of Tables

Abstract

This thesis reports on a method to conduct two-dimensional modeling of a klystron traveling-wave-type output structure. In the klystron, the input and output couplers violate axial symmetry. To design a klystron with a 2.5-dimensional particle-in-cell simulation code, we should make two-dimensional models for these two parts. An input cavity can be simulated by applying on RF voltage at the gap. For the output cavity, since a traveling-wave-type output structure is used to reduce the maximum electric field, the port approximation method is not applicable.

In this report, the output coupler is considered to be a mode converter between the TE10 mode of the rectangular waveguide and the cavity cell mode. The scattering matrix is calculated using a frequency-domain code. In a particle-in-cell simulation, a finite conducting material is set in the coupler region so as to match the reflection coefficient of the scattering matrix. The output powers, which are calculated using the Poynting vector, agree with the measured values of the KEK XB72K No.8,9 and the SLAC XL-4 klystrons within a 10% error.

Using the above method, we designed a new KEK klystron (XB72K No. 10). A bunching cavity is added to increase the RF current. The $2\pi/3$ mode is used for the output structure to reduce the maximum electric field. As a result of two-dimensional simulations, we obtained the design of a 120MW klystron.

Chapter 1

Introduction

1.1 Brief Overview of Klystrons

The klystron was invented by R. H. Varian, and the first device was developed by S. F. Varian in 1937 for high-frequency (GHz) power generation. During World War II, many low-power klystrons were manufactured for radar systems. After the war, M. Chodorow and E. L. Ginzton developed the first high-power (3GHz,20MW) klystron amplifier in 1949 as an RF power source for an electron linac. Since then, many high-power klystrons have been developed and used in many particle accelerators.

Triodes and tetrodes are also used as the RF power source for particle accelerators. However, these tubes are not suitable for high-frequency operation because the transit time of the electrons between the electrodes cannot be made much smaller than the inverse of the operation frequency. For example, if one applies a voltage of 10 kV between a gap of 1 cm, the inverse of the transit time amounts to 3 GHz. Also, the inductance of the leads to the electrodes reduces the frequency upper limit. Consequently, for practical use, the upper limit of the frequency for tetrodes is a few hundred MHz.

A klystron amplifier has a simple structure. In a typical klystron amplifier, a beam from an "electron gun" is accelerated up to several hundred keV. The beam then passes through an "input cavity", where each electron receives acceleration depending on the phase of the gap voltage. The beam then passes through idler cavities called "gain cavities". In the gain cavity, the RF current of the beam generates the RF voltage, which gives additional velocity modulation to the beam. The beam then traverses a "drift space",

where the velocity variations of the electrons in the beam are converted to density modulation. The bunched beam passes through idler cavities, called "bunching cavities" or "penultimate cavity", which provide additional bunching to the beam. Finally, the bunched beam passes through an "output cavity", where the RF energy created by RF current of the bunched beam is transmitted to the outside through a "coupler".

With this structure, the transit time of the electron is used to obtain the density modulation of the beam; this mechanism makes klystrons high-frequency devices.

Klystrons have been developed by people mainly in the field of particle accelerators for high-energy physics. This study is also for the high-energy physics. We briefly describe high-energy physics and particle accelerators in the next section.

1.2 High-Energy Physics and Particle Accelerators

As the ancient Chinese thinker Confucius (551? – 479 B.C.) said, 'I would agree to die in the evening, if I understand the truth of life in the morning', every person in the world is eager to understand universal truth and the meaning of life. Descartes examined it by using the reduction method. His philosophy has influenced people to examine everything microscopically, which has helped to science, especially physics. Since many scientific researches have been successful, which means that they have helped people to do good things, science has been recognized by people and funded. Meanwhile, owing to the origin of science, there have been many scientists who want to divide materials and to find things which cannot be divided; they are called elementary-particle physicists or high-energy physicists. To divide material, they need to hit it with accelerated particles. The energy of such accelerated particles should be higher to find unknown things. They obtained funding funded from governments and constructed many high-energy particle accelerators using a lot of ideas. (One idea is to also accelerate the target particle, and to collide it against the another accelerated particle; these particle accelerators are called 'colliders'. If the target particle and the accelerated particle have the same mass (m), and the energy of the accelerated particle is E, the center of mass energy is $\sqrt{2(mc^2)^2 + 2mc^2E}$. If the target particle

also has kinetic energy of $E - mc^2$, the center of mass energy is $2E$.) They experienced good days from the 1930's to the 1980's while searching for new particles. One brilliant effort resulted in the discovery of W and Z bosons by using SPS in 1983, which verified the unified theory of electromagnetic and weak interactions by S. Weinberg and A. Salam. Although their aim was not directly related to people's daily life, they provided many useful by-products, such as isotopes, synchrotron-radiation sources, and ion beams for cancer treatment. Unfortunately, the progress of the high-energy particle accelerator physics seems to have become slow since the 1990's. One reason is that no phenomena which violate the 'standard theory' have been found since the 1980's. The neutrino-oscillation phenomenon may be the only exception. Another reason is that the construction and operation cost of particle accelerators with energies high enough to check sophisticated theories are very expensive. Besides, the high-energy particle accelerator physicists themselves, will hardly help people in the world. In any case, since the particle accelerator is the only way to make a large amount of high-energy particles, several machines will be constructed in the future in order to understand the truth of nature.

1.3 Japan Linear Collider

Proton synchrotrons have presently been taking the initiative in the search for new particles, because protons can be accelerated with little energy loss by synchrotron radiation. The particle energy loss(ΔU) per turn by synchrotron radiation is

$$\Delta U(\mathrm{keV/turn}) \simeq 88.5 \left(\frac{m_e}{m}\right)^4 \frac{(E(\mathrm{GeV}))^4}{\rho(\mathrm{m})}, \tag{1.1}$$

where m_e, m, ρ are the electron mass, particle mass, and radius of the particle orbit in bending magnets, respectively. For a 0.5 TeV proton synchrotron with $\rho = 1$ km, ΔU is 0.5 eV/turn, which can be neglected.

One disadvantage of proton accelerators in the search for unknown particles is that the proton is a composite particle of three quarks. Accordingly, any analysis of events is extremely complicated. If one needs a clean result, one must accelerate elementary particles instead of protons.

The available elementary charged particles are leptons, such as the electron, muon, and tau. Quarks cannot be used, because they cannot be extracted from nuclei due to the strong interaction.

If a muon or tau lepton is accelerated, the energy loss is $\Delta U = 3.0$ keV/turn or 0.04 eV/turn for $E = 0.5$ TeV, $\rho = 1$ km. One of the difficult problems in this scheme is how to accumulate a sufficient number of low-temperature particles.

In this regard, electrons are desirable, because plenty of electrons exist in materials and a good-quality electron beam can be easily obtained by an elctron gun. However, since the mass of the electron is small, the energy loss due to synchrotron radiation is quite large for an electron ring. For example, if a 0.5 TeV electron is running in a ring with a radius of 1 km, the energy loss is 5.5 TeV/turn. Even if the radius of curvature is increased to 100 km, the energy loss is still 55 GeV/turn, which means 10% of the energy is lost with every turn. To reduce the energy loss, say to $\Delta U < 100$ MeV/turn, ρ should be greater than 5.5×10^7 m, which is nearly the radius of the equater of the earth. The construction of a TeV electron synchrotron is almost impossible. Hence, electrons should be accelerated by linear accelerators. Thus, the Japan Linear Collider (JLC) [4] program was proposed for TeV-energy physics.

In this scheme, electrons are to be accelerated to 500 GeV by an 11 km linac and to collide with positrons having the same energy. The electric-field gradient is higher (500 GeV / 11 km $\sim$ 50 MeV/m) than that of the existing linear accelerators ($\sim$ 20 MeV/m) in order to reduce the cost. To obtain a higher electric field gradient, JLC proposes to use the C-band (5.712 GHz) or the X-band (11.424 GHz) for the main linear accelerators, because, according to Kilpatrick [6], the threshold electric field is nearly proportional to the square root of the frequency. Since these frequencies have not been used before, RF components at these frequencies are now under development by KEK and SLAC.

This study is for the development of X-band klystrons. To see the reason why we chose klystron as the power source, we briefly review the X-band RF power sources in the next section.

1.4 X-band RF Power Sources for Accelerators

High-power X-band RF power sources have been reviewed by S. H. Gold and G. S. Nusinovich [3]. According to [3], there are three types:

- Relativistic klystrons
- Gyroklystrons
- Magnicons

Klystrons were briefly discussed in Section 1. The two-beam accelerator (TBA) is a kind of relativistic klystron. A high-energy (4-10 MeV) electron beam is reused many times in this device. A small fraction ($< 10\%$) of the kinetic energy is extracted at each stage, and the beam is reaccelerated. The advantages of this device are:

- The overall efficiency can be high because the beam is reused.
- The space-charge force is small because the beam energy is high.
- Smaller number of electron guns are needed. This may reduce problems with the electron guns.

One problem with this scheme is how to maintain good quality of the beam while reusing it. Experiments of the two-beam accelerators for the X-band were conducted by LBNL; they obtained 180 MW peak power in 25 nsec pulses. Since it will take time to put this system to practical use, it will be developed for the future electron collider CLIC (The Compact Linear Collider Study) by CERN.

The gyroklystron is a kind of gyrodevice. The electron gun of this device is a magnetron injection gun (MIG), from which a hollow beam with some transverse velocity is emitted. Then, the electrons of the hollow beam begin to rotate in a strong axial static magnetic field. The beam couples to the TE011 mode. The development of X-band gyroklystrons is under way at the University of Maryland, where 32 MW of output power has been obtained.

The magnicon uses a rotating TM110 mode to deflect the electron beam. Since all electrons of the beam are in phase with the field in the output cavity, the efficiency of the magnicon can be very high. Two groups are developing magnicons: one at BINP, and the other at NRL. One of the BINP magnicons has emitted a 46MW, 1μsec pulse at 7GHz.

Although these devices may become better suited for linear colliders than the klystron in the future, it takes a longer time to develop them. That is the reason why we are developing the X-band klystrons for JLC.

Operating Frequency	11.424 GHz
Peak Output Power	120 MW
RF Pulse Width	$\sim$ 500 nsec
Pulse Repetition Rate	50 $\sim$ 100 pps
Beam Voltage	550 kV
Beam Current	490 A
Efficiency	45 %
Saturated Gain	53 $\sim$ 56 dB
Focusing Field	6.5 kG
Beam Areal Compression	110:1
Cathode Diameter	72 mm
Max. Cathode Current Density	17 A/cm^2
Max. Surface Grad. in Gun	273 kV/cm
Max. Surface Grad. in Output Gap	720 kV/cm

Table 1.1: Design specifications of XB72K

1.5 Development of X-band Klystrons for JLC

The development of X-band klystrons, which is called the XB72K series[4, 2], started at KEK for JLC in 1990. The design specifications of XB72K are given in Table 1.1. Figure 1.1 shows a schematic view of the XB72K electron gun and cavities. The electron gun was designed with 1.2 micro perveance. The gun design has not been changed during the development of the XB72K series. There are two gain cavities and one penultimate cavity in the (No. 1 through No. 9) klystrons. Four solenoid coils and one bucking coil are used to obtain a 7 kG axial magnetic field.

The output cavities of the XB72K (No. 1 through No. 5) klystrons were of the single-cell type, without any nose cone[12]. These klystrons were designed using the FCI 2.5-dimensional simulation code written by T. Shintake[13].

The No. 1 klystron used a short-pillbox-type RF window for each rectangular waveguide. At the test, the RF windows were broken at around 40-50 MW. Since both sides of the window were in a vacuum, the test continued and the cathode voltage was raised to obtain 90 MW at a 50 nsec output pulse. After the test, it was found that the surface of the edge of the output cavity has not been damaged. The edge radius of the output cavity of the No. 1 klystron was 2mm.

From the No. 2 klystron, the edge radius of the output cavity was changed from 2mm to 1mm in order to increase the efficiency. New long pillbox-type RF windows were used, and were not broken during a test. After the test, an autopsy of the No. 2 klystron showed that the output cavity had melted down. It seemed that the RF discharge in the output cavity was the main problem for these klystrons. Another example of evidence of RF discharge is that the threshold output power of the No.2 klystron reached 90 MW at 50 nsec pulse duration, whereas the threshold output power was 40 MW when the pulse duration was 300 nsec. This was because the threshold of the RF discharge depends on the pulse duration.

From the experience of the No. 2 klystron test, we come to understand that the electric field in the output structure should be reduced so as to avoid a RF discharge. Two requirements are effective to reduce the electric field:

- To make the interaction length in the output structure longer
- To make the bore radius larger

Multi-cell traveling-wave-type structures satisfy these requirements. From the No. 7 klystron, traveling-wave-type output structures have been designed and tested.

The existing klystron simulation codes could not be used to design a traveling-wave-type structure because they use the port approximation method to simulate the output structure. One method used to simulate the traveling-wave structure was developed by S. Kazakov of Branch of Institute of Nuclear Physics (BINP)[5]. This method was included in the one-dimensional simulation code DISKLY[16] written by V. Teryaev of BINP. The DISKLY code was used to design the traveling-wave-type structures of the No. 7 through the No. 9 klystrons.

For the No. 7 klystron, they designed a five-cell structure with an output coupler at the fourth cell. Since the modes of the fifth cell and the collector were coupled, the RF output is unstable for pulses longer than 100-200 nsec.

The No. 8 klystron has a five-cell output structure with an output coupler at the fifth cell. Although the RF output is stable, the output power reached only 60MW, which was much smaller than 110MW obtained by a DISKLY simulation.

The No. 9 klystron has a four-cell structure with an output coupler at the fourth cell. This klystron is also stable. The output power of No. 9 is

around 80MW, which is also smaller than the expected value by a DISKLY simulation.

Figure 1.2 shows the saturated output power of the No. 8 and No. 9 klystrons.

The large discrepancy in the output power between measurements and simulations is due to the limitation of a one-dimensional simulation. To obtain a better simulation of the klystron efficiency, MAGIC2D[8], a 2.5-dimensional (2D fields and 3D particle kinamatics) particle-in-cell code, was introduced at KEK in 1997.

Various klystron simulation codes will be listed in the next section.

1.6 Comparison of Klystron Simulation Codes

Table 1.2 compared various klystron simulation codes.

The electron gun is usually designed by using EGUN. This program solves the Poisson equation with the finite-difference method. It has been reported that the perveance calculated by EGUN is by several percent smaller than the measured value[10]. DGUN also uses the finite-difference method to solve the Poisson equation. In the case of an X-band klystron gun, the perveance calculated by DGUN agrees with the measured value within a few percent.

The cavities are simulated in many codes by using the port-approximation method[15]. The 'port approximation' is defined in [15] as the replacement of a full cavity by the RF voltage across the corresponding port. Practically, a single mode is assumed, and the following equation is used:

$$0 = -i\left(\frac{\omega}{\omega_r} - \frac{\omega_r}{\omega}\right) + \frac{1}{Q_0} + \frac{2R/Q}{V_g^2}\left(\frac{1}{2}\int dV\,\vec{J}\cdot\vec{E}^* - P_{ext}\right), \qquad (1.2)$$

where ω,ω_r,Q_0, R, V_g, $\vec{J}$, $\vec{E}$, P_{ext} are the frequency, the resonant frequency, the unloaded quality factor, the shunt impedance, the gap voltage, the RF current density of the electron beam, the RF electric field in the cavity, and the complex transmitted power from the outside of the cavity, respectively. The amplitude and phase of the RF electric field are solved using the above equation and an iteration method. This method saves simulation time because the steady state is found directly.

A drawback of this method is that it is not applicable to a multi-cell cavity, such as a traveling-wave-type output cavity, since the excitation of only a single mode is assumed in Eq.(1.2). To simulate multi-cell structures,

Table 1.2: Comparison of klystron simulation codes

Name	Author(s)	Dim.	Method	Gun	Multi mode	Remarks
EGUN	W. B. Herrmannsfeldt	2	FD	○	×	Gun design
DGUN	A. Larionov	2	FD	○	×	Gun design
JAPANDISK	H. Yonezawa, Y. Okazaki	1	PA	×	×	
DISKLY	V. Teryaev	1	PA	×	○ by Kazakov	XB72K#7-9
ARSENAL	V. E. Rodyakin, A. N. Sandalov	2	PA,FD	○	×	
FCI	T. Shintake	2	PA	×	△	XB72K#1-5
CONDOR	K. Eppley	2	PA,FDTD?	×	○	SLAC klystrons
MAGIC	B. Goplen, L. Ludeking, D. Smithe	2,3	FDTD	○	○	XB72K#10
MAFIA	T. Weiland	2,3	FDTD	×	○	

FD: Finite Difference Method
FDTD: Finite Difference Time Domain Method
PA: Port Approximation Method

some codes use other methods. The DISKLY code uses S. Kazakov's method to simulate a multi-cell structure. FCI uses a method to simulate a 3-cell structure.

MAGIC and MAFIA are general-purpose time-domain codes, which use a finite-difference time-domain method. Since these codes solve the discretized Maxwell's equations, they can simulate a multi-cell structure without any approximations. The drawbacks of this method are:

- Time consuming
- Difficult to set parameters exactly, such as the resonant frequencies of the cavities

Among the codes in Table 1.2, MAGIC is the only one used to simulate from the electron gun to the multi-cell output structure.

1.7 X-band Klystron Simulation by MAGIC2D

As described in the previous section, MAGIC can simulate almost all electromagnetic problems, including an electron gun. A two-dimensional version of MAGIC (MAGIC2D) was used to simulate klystrons because the CPU speed of computers are not presently enough to make precise three-dimensional simulations.

Since the couplers of the input and output structures break the axial symmetry, these parts cannot be simulated directly by MAGIC2D.

The input cavity can be simulated by applying some RF voltage at the gap. The saturated output power can be obtained by varying the gap voltage. However, in order to calculate the gain (output RF power / drive RF power), the relation between the gap voltage and the drive RF power should be known. This issue is discussed in Chapter 3.

Making a two-dimensional model of the traveling-wave-type output structure seems to be difficult because there are many modes near to the operating frequency, and their contributions to the output power are not negligible. The main purpose of the present study was to obtain a reasonable two-dimensional model of the traveling-wave-type output structure.

First of all, we looked at the coupler region locally, and found that if the cell width is small, the electric field pattern in the cell is almost like the TM010 mode in a pill-box cavity. We call this the 'TM0*0 mode' in

this report because the traveling waves of this mode propagate in the radial direction. The output coupler can be considered to be a mode converter between the TM0*0 mode of the cavity cell and the TE10 mode of the rectangular waveguide. We defined the scattering matrix of the TM0*0 mode and the TE10 mode. The scattering matrix was calculated numerically by a new method which uses a frequency-domain codes.

To conduct a simulation of the output cavity using the reflection coefficient at the coupler calculated by our new method, we put a material with finite conductivity in the coupler region and adjusted the inner and outer radii and the conductivity. The output power was calculated using the Poynting vector. The details of the procedure are given in Chapter 2.

We made full simulations of the XB72K No. 8, 9 and the SLAC XL-4 klystrons using MAGIC2D. The saturated output power by MAGIC2D agree well with the measured value. The details of the simulation are given in Chapter 3.

Using the method described in Chapter 2, we designed the XB72K No. 10 klystron. A MAGIC2D simulation shows that this klystron attains 120MW output power with a low maximum electric field in the output structure. The design process is described in Chapter 4.

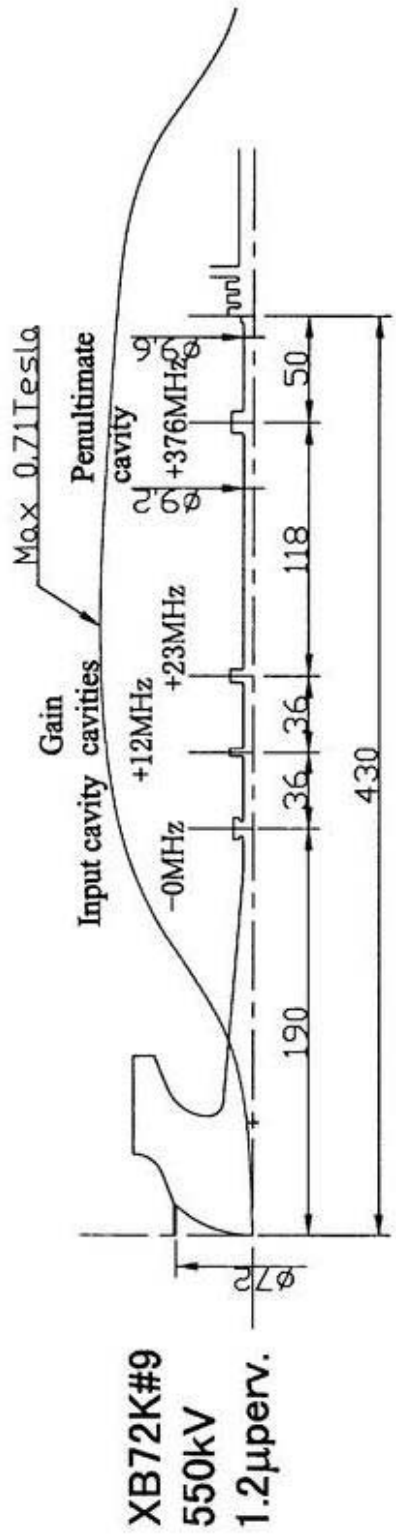

Figure 1.1: Schematic view of the XB72K No. 1 - No. 9 klystron electron gun and cavities.

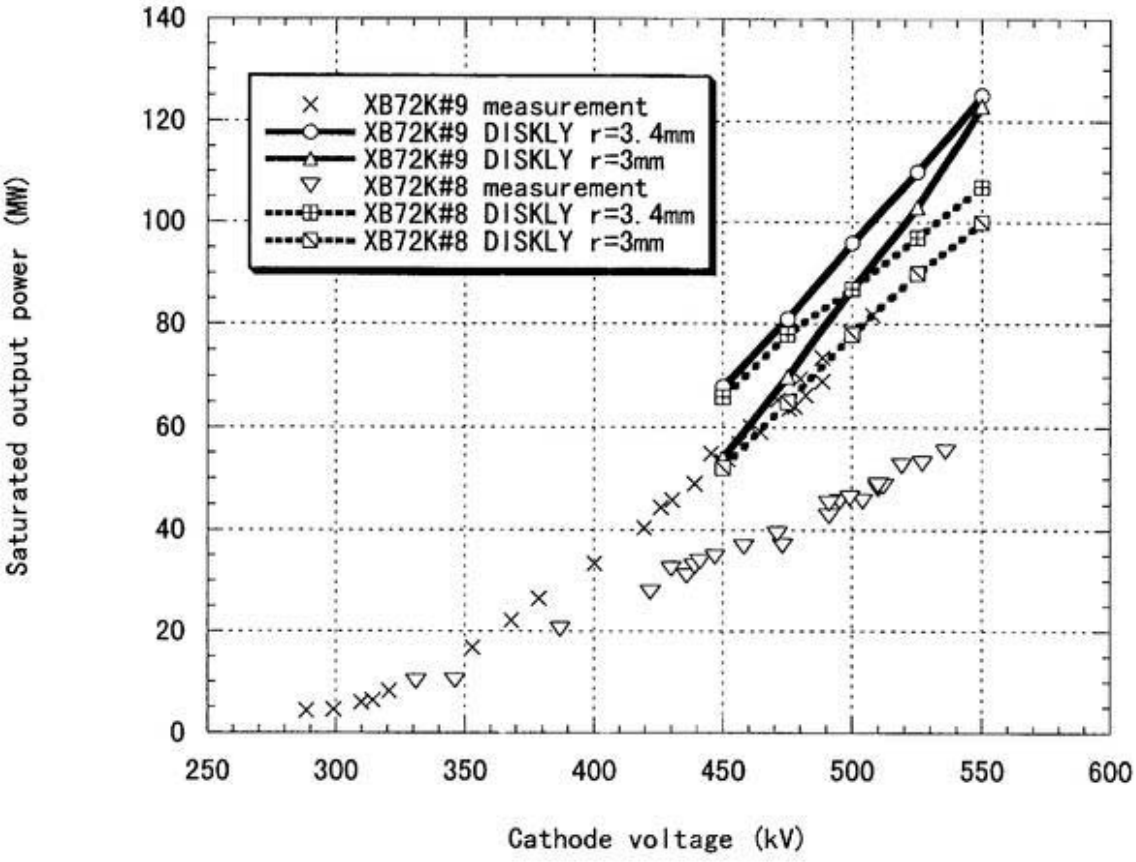

Figure 1.2: Saturated output power based on measurements and DISKLY simulations for the XB72K No.8 and the No. 9 klystrons. We assumed that the beam radius is 3mm or 3.4mm in the DISKLY simulations.

Chapter 2

A Method for Finding Scattering Matrix

As described in the previous chapter, we need an axially symmetric model of the output structure to simulate a klystron with general two-dimensional codes. The model can be obtained with knowledge of the scattering matrix between the cavity mode and the TE10 rectangular waveguide mode.

A definition of the scattering matrix is given in Section 1.

One method to obtain a numerical value of the scattering matrix is given in Section 2.

The reflection coefficient of the cavity cell mode is calculated from the scattering matrix and the reflection coefficient at the rectangular waveguide.

We then construct an axially symmetric model. We set a finite conducting material in the coupler region properly so that this model satisfies the required reflection coefficient. This method is discussed in Section 3.

2.1 Definition of the Scattering Matrix

Figure 2.1 shows the structure of the No. 9 output cavity. For a four-cell output structure, four TM01 modes make the electric-field and the magnetic field in the cavity. Figure 2.2 shows the electric field lines of the four modes in the No. 9 output structure. This figure was plotted by using SUPERFISH. We observe that the electric field has a small longitudinal variation in each cell. By neglecting it ($\partial/\partial z = 0$), we obtain the following equation for the

electric field of TM0 modes in the fourth cell:

$$\frac{1}{r}\frac{\partial}{\partial r}\left(r\frac{\partial E_z}{\partial r}\right)+\left(\frac{\omega}{c}\right)^2 E_z = 0. \tag{2.1}$$

The dependence of the field on time is assumed to be $\exp(-i\omega t)$. The solution of Eq. (2.1) is

$$\begin{aligned} E_z &= a_{1in}H_0^{(1)}(kr)+a_{1out}H_0^{(2)}(kr), \\ k &= \omega/c, \end{aligned} \tag{2.2}$$

where $H^{(1)}, H^{(2)}$ are Hankel functions[1]. We refer to this as the 'TM0*0 mode' in this report because the waves of this mode propagate in the radial direction. Since the asymptotic forms of the Hankel functions as $|kr| \to \infty$ are

$$H_0^{(1,2)}(kr) = \sqrt{2/(\pi kr)}\exp(\pm i(kr-\pi/2)), \tag{2.3}$$

the first and second terms of Eq. (2.2) indicate incoming and outgoing waves seen from the coupler, respectively.

Two rectangular waveguides are attached to the fourth cell through the coupler. The TE10 wave propagates in the rectangular waveguide and power is extracted. The electric field in the rectangular waveguide is

$$\begin{aligned} E_z &= a_{2in}\cos(\pi x/a)\exp(-ik_g y)+a_{2out}\cos(\pi x/a)\exp(ik_g y), \\ k_g &= \sqrt{(\omega/c)^2-(\pi/a)^2}, \end{aligned} \tag{2.4}$$

where a is the width of the waveguide. Coordinates x, y are shown in Figure 2.1. The first and second terms on the right-hand side of Eq. (2.4) correspond to incoming and outgoing waves seen from the coupler, respectively.

The coupler can be assumed to be a mode converter between the TM0*0 mode in the cavity cell and the TE10 mode in the waveguide. Thus, the scattering matrix(S) can be defined as

$$\begin{pmatrix} a_{1out} \\ a_{2out} \end{pmatrix} = S\begin{pmatrix} a_{1in} \\ a_{2in} \end{pmatrix} = \begin{pmatrix} S_{11} & S_{12} \\ S_{21} & S_{22} \end{pmatrix}\begin{pmatrix} a_{1in} \\ a_{2in} \end{pmatrix}. \tag{2.5}$$

What we need to know for the output structure simulation is the reflection coefficient, $s = a_{1out}/a_{1in}$, when there is reflection(r) at the rectangular waveguide. Using Eq. (2.5) and $a_{2in} = ra_{2out}$, we obtain

$$s = S_{11} + rS_{12}S_{21}/(1-rS_{22}). \tag{2.6}$$

The above equation can also be derived in the following way. When the input wave a_{1in} is 1, s is the sum of a wave which reflects at the coupler and of the waves which go through the coupler, reflect in the rectangular waveguide $2n+1(n=0,1,2,\cdots)$ times, and come back through the coupler:

$$s = S_{11} + S_{21}(\sum_{n=0}^{\infty} r^{n+1} S_{22}^{n}) S_{12} = S_{11} + rS_{12}S_{21}/(1 - rS_{22}). \tag{2.7}$$

In order to calculate s, we have to know r, S_{11}, S_{22}, and $S_{12}S_{21}$. In this report, we assume that the reflection coefficient at the rectangular waveguide is zero ($r = 0$). From this assumption, the reflection(s) is S_{11}. If there is some reflection at the DLDS system or at the accelerating structure, r is not 0. In this case, the output structure should be simulated with reflection(s) which is not equal to S_{11}.

2.2 Calculation of the Scattering Matrix

Since the cross section of the waveguide of the TM0*0 wave is not constant, the scattering matrix cannot be calculated directly by the existing codes, such as HFSS. We have developed a method to calculate it, which is shown below.

The parameters ξ_1, ξ_2 are defined so that

$$\xi_1 = a_{1out}/a_{1in}, \xi_2 = a_{2out}/a_{2in}. \tag{2.8}$$

Using these parameters, Eq. (2.5) becomes

$$(S_{11} - \xi_1)(S_{22} - \xi_2) = S_{12}S_{21}. \tag{2.9}$$

If we know three independent (ξ_1, ξ_2) pairs for a given frequency(ω), S_{11}, S_{22}, and $S_{12}S_{21}$ at ω can be calculated using Eq. (2.9).

The scattering matrix is the relation between the incoming and outgoing traveling waves. A traveling wave can be decomposed into two standing waves of different phases, and a standing wave can be decomposed into two traveling waves of different directions, and vice versa. Hence, traveling waves and standing waves are the same in a sense. We can therefore use standing waves to calculate the scattering matrix. To create standing waves, both ends of a TM0*0 waveguide and a rectangular waveguide are closed. A

frequency-domain code is used to calculate the standing waves and the resonant frequency of the system. We need some technique to create standing waves of different phases in each waveguide, as shown below.

MAFIA[17], an eigenmode solver, is used to calculate three (ξ_1, ξ_2) pairs. As shown in Figure 2.3, the waveguide is short-circuited by a plunger at distance $y = d$, and the dielectric material is set at the center of the cavity cell.

By moving the plunger, the parameter ξ_2 can be varied. Since the electric field(E_z) of Eq. (2.4) is 0 on the plane $y = d$, ξ_2 is

$$\xi_2 = -\exp(-2ik_g d). \tag{2.10}$$

By changing the relative dielectric constant(ϵ_r) of the material, the parameter ξ_1 can be varied as

$$\begin{aligned} \xi_1 &= \frac{kJ_0(k'b)H_1^{(1)}(kb) - k'J_1(k'b)H_0^{(1)}(kb)}{k'J_1(k'b)H_0^{(2)}(kb) - kJ_0(k'b)H_1^{(2)}(kb)}, \\ k' &= \sqrt{\epsilon_r}\omega/c, \end{aligned} \tag{2.11}$$

where b is the radius of the dielectric material, J is a Bessel function. Details concerning the derivation of Eq. (2.11) are given in Appendix A.

The following equations can be obtained from the energy-conservation law:

$$\begin{aligned} |S_{11}| &= |S_{22}|, \\ |S_{11}|^2 + |S_{12}S_{21}| &= 1, \\ S_{11}S_{22} - S_{12}S_{21} &= S_{22}/S_{11}^*. \end{aligned} \tag{2.12}$$

The derivations of these equations are shown in Appendix B. These equations are used to check the validity of the calculation.

Figure 2.4 shows one example of a MAFIA frequency-domain calculation. We searched the positions of the plunger(d) for given frequency(ω) and relative dielectric constants $(\epsilon_r = 1, 3, 5)$, as shown in Figure 2.5. Using Eq. (2.9), S_{11}, S_{22} and $S_{12}S_{21}$ were calculated. The reflection coefficient(S_{11}) is shown in Figure 2.6.

2.3 Axially Symmetric Simulation of the Coupler Port

As shown in Section 2, the scattering matrix for the cavity cell TM0*0 mode and the TE10 mode of the rectangular waveguide was calculated. By using Eq. (2.6), the reflection coefficient(s) of the TM0*0 mode was calculated from the scattering matrix as well as the reflection coefficient(r) at the rectangular waveguide. Since we assume that r is zero, s is S_{11} in this report.

Instead of conducting three-dimensional simulations of the coupler port, we made two-dimensional simulations by MAGIC2D with the same reflection coefficient(s) by using an axially symmetric finite conducting material, as shown in Figure 2.7. With this configuration, s is analytically given by

$$\begin{aligned} s &= \frac{k\alpha H_1^{(1)}(kh) - k''\beta H_0^{(1)}(kh)}{k''\beta H_0^{(2)}(kh) - k\alpha H_1^{(2)}(kh)}, \\ \alpha &= H_0^{(1)}(k''g)H_0^{(2)}(k''h) - H_0^{(2)}(k''g)H_0^{(1)}(k''h), \\ \beta &= H_0^{(1)}(k''g)H_1^{(2)}(k''h) - H_0^{(2)}(k''g)H_1^{(1)}(k''h), \\ k'' &= \sqrt{(\omega/c)^2 + i\mu_0\sigma\omega}, \end{aligned} \tag{2.13}$$

where g, h, σ are the outer radius, the inner radius, and the electric conductivity of the material, respectively. The derivation of Eq. (2.13) is shown in Appendix C. The parameters (g, h, σ) are adjusted to reproduce the same value of s which was calculated in Section 2 at the operating frequency. Since this is the $(g, h, \sigma) \mapsto (Re(s), Im(s))$ map, one parameter is free. Consequently, there are an infinite number of choices of (g, h, σ), as shown in Figure 2.8 for a given s.

Figure 2.9 shows the reflection coefficient as a function of frequency when $g = 12.48$mm, $h = 10.57$mm, $\sigma = 2.5$ /Ω m.

2.4 Summary

A two-dimensional model of the output coupler was developed by assuming that the coupler is a mode converter between the cavity mode and the TE10 mode of the rectangular waveguide. The scattering matrix is defined as the mode conversion coefficient of these modes. This matrix is numerically calculated using the MAFIA eigenmode solver. A finite conducting material is

set properly in the coupler region so that the model satisfies the required reflection coefficient. This method is empirically justified in the next Chapter.

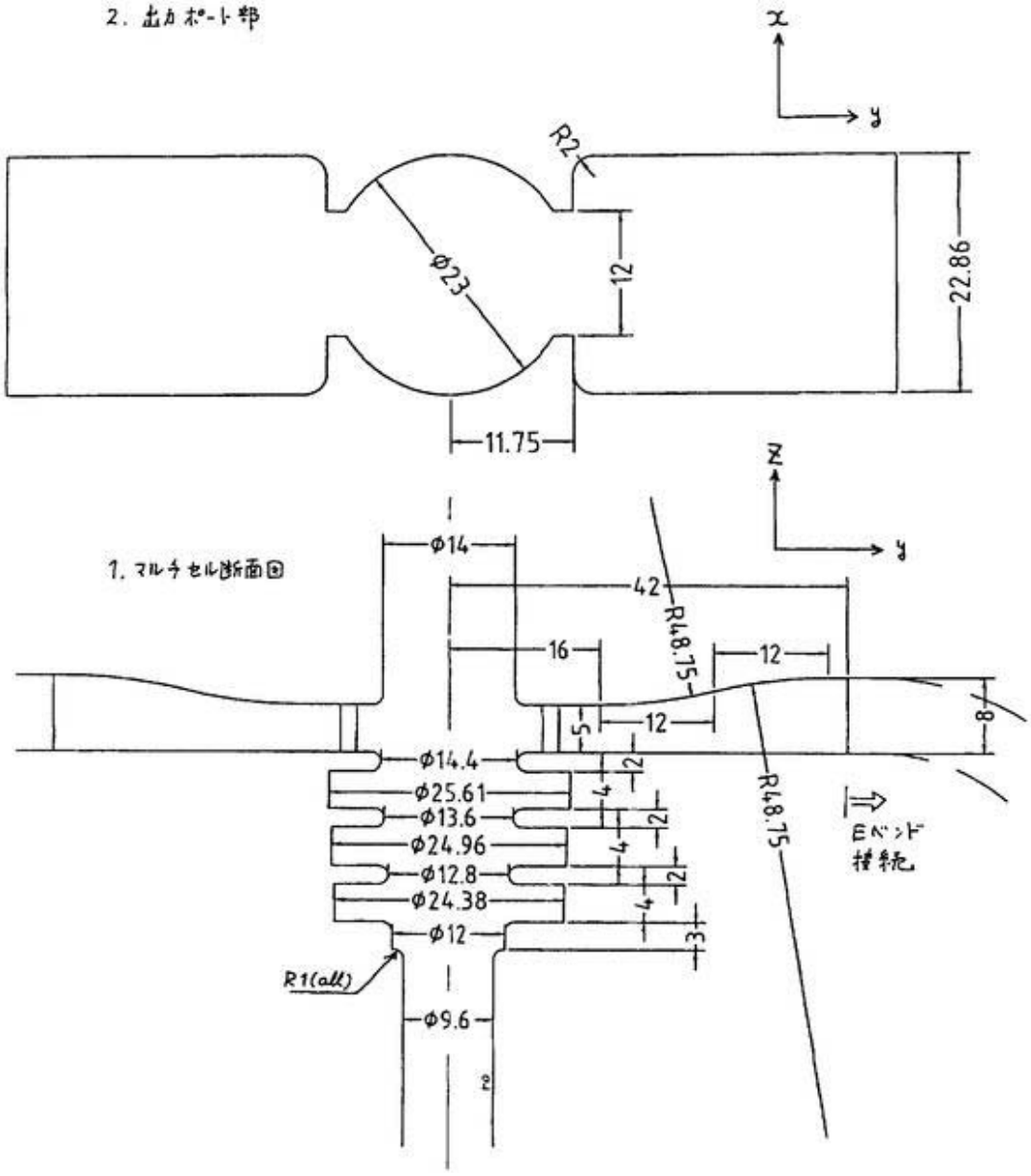

Figure 2.1: XB72K No. 9 output structure

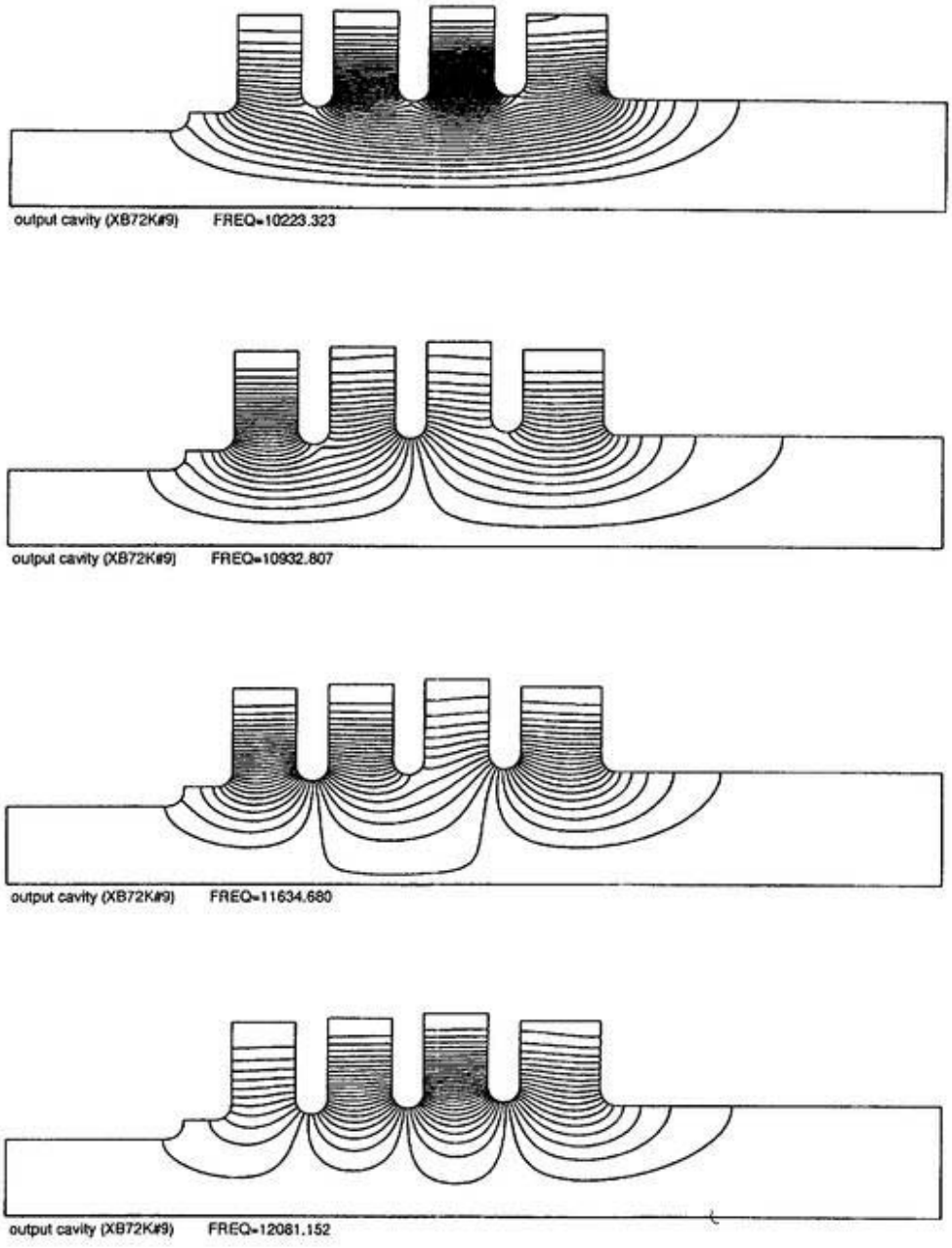

Figure 2.2: Electric field lines of four TM01 modes of the XB72K No. 9 output structure

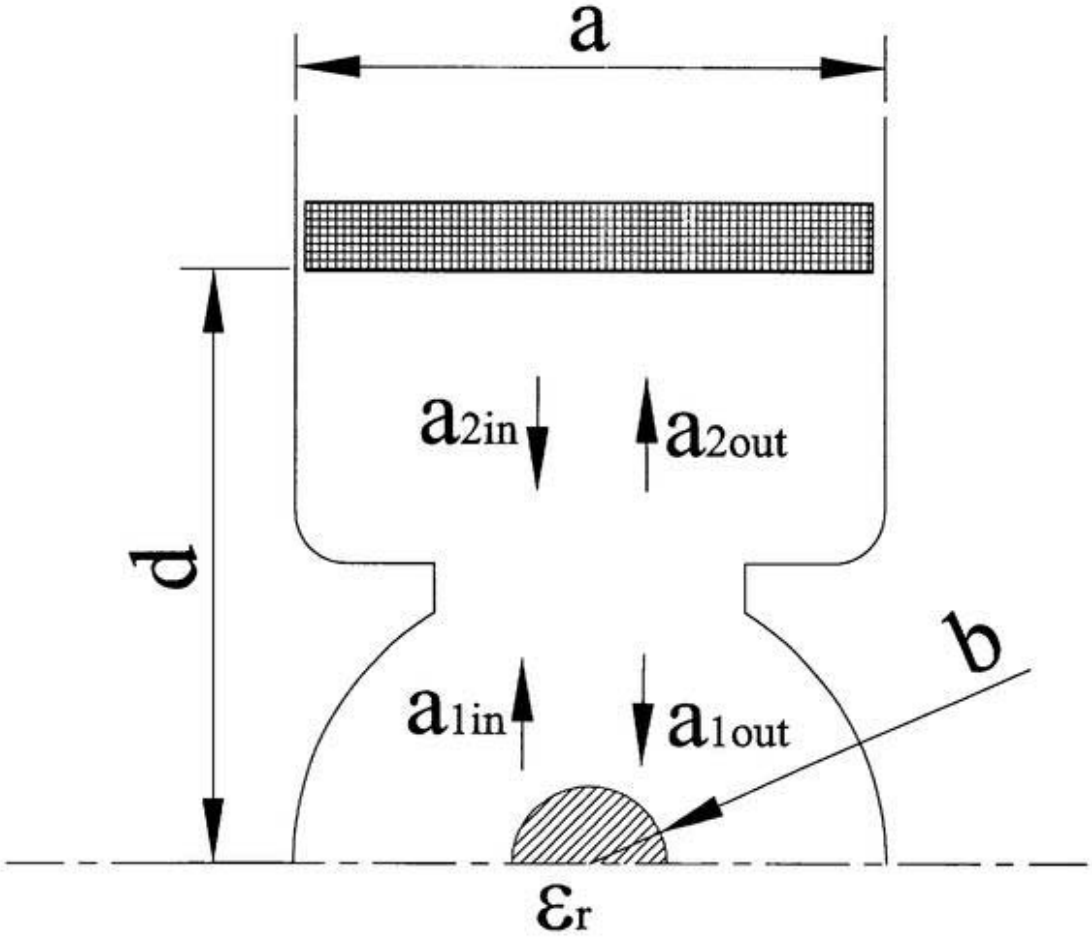

Figure 2.3: Configuration for a MAFIA frequency-domain calculation

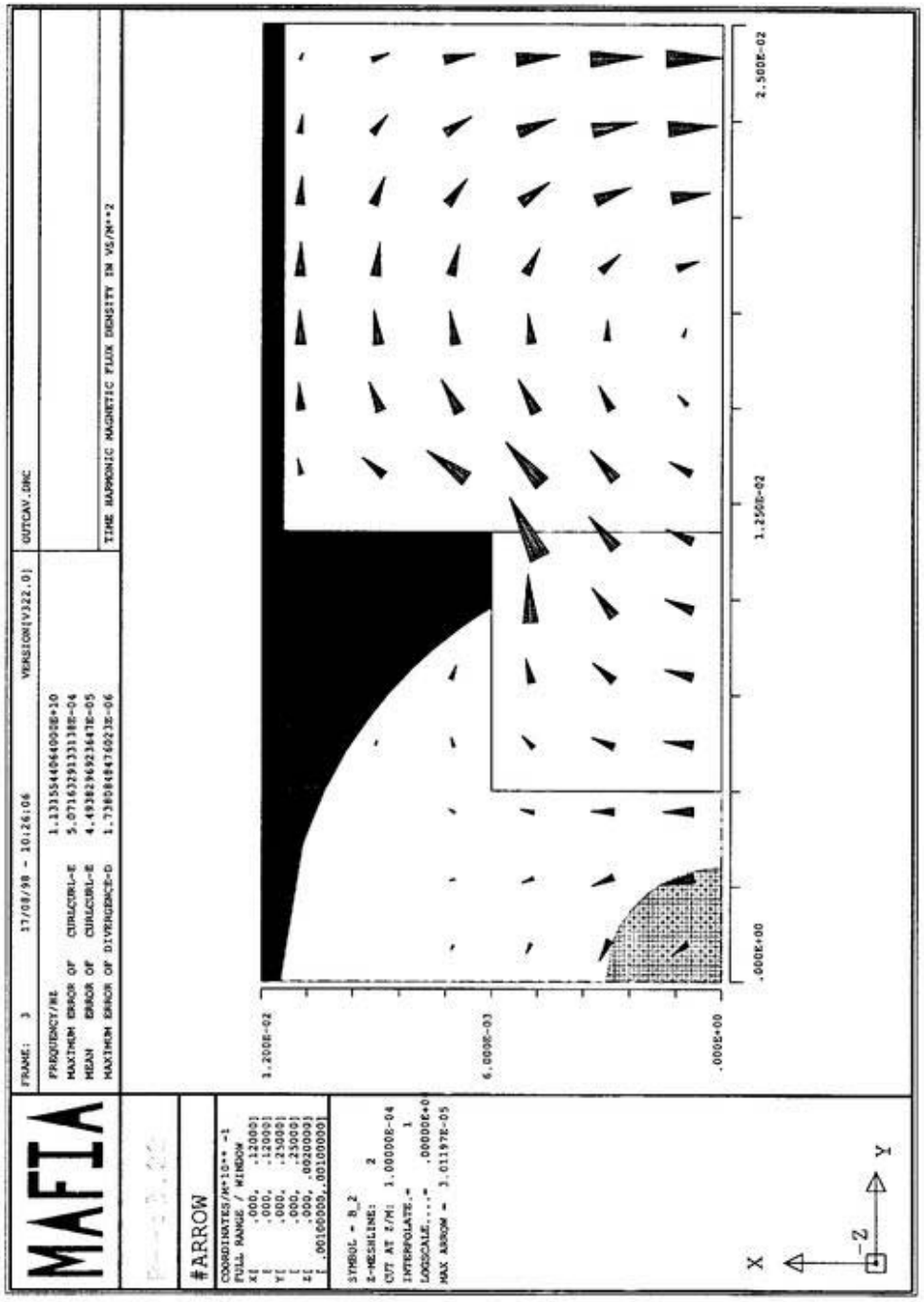

Figure 2.4: Example of a MAFIA frequency-domain calculation

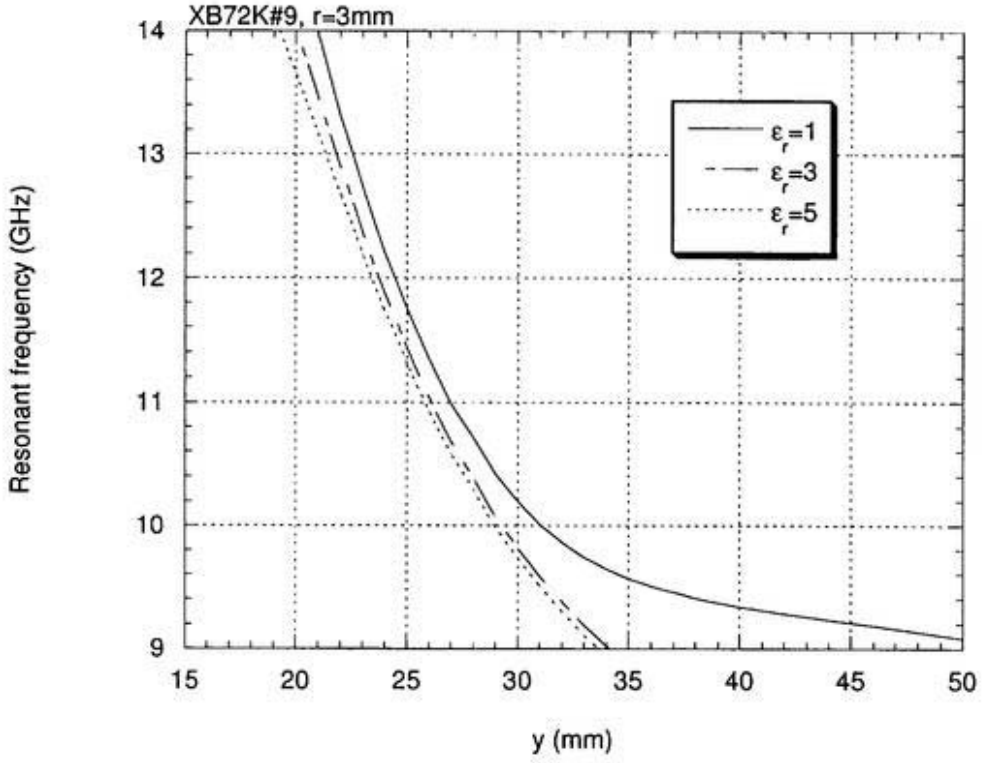

Figure 2.5: Resonant frequency of the mode as a function of the plunger position for three values of the relative dielectric constant ($\epsilon_r = 1, 3, 5$).

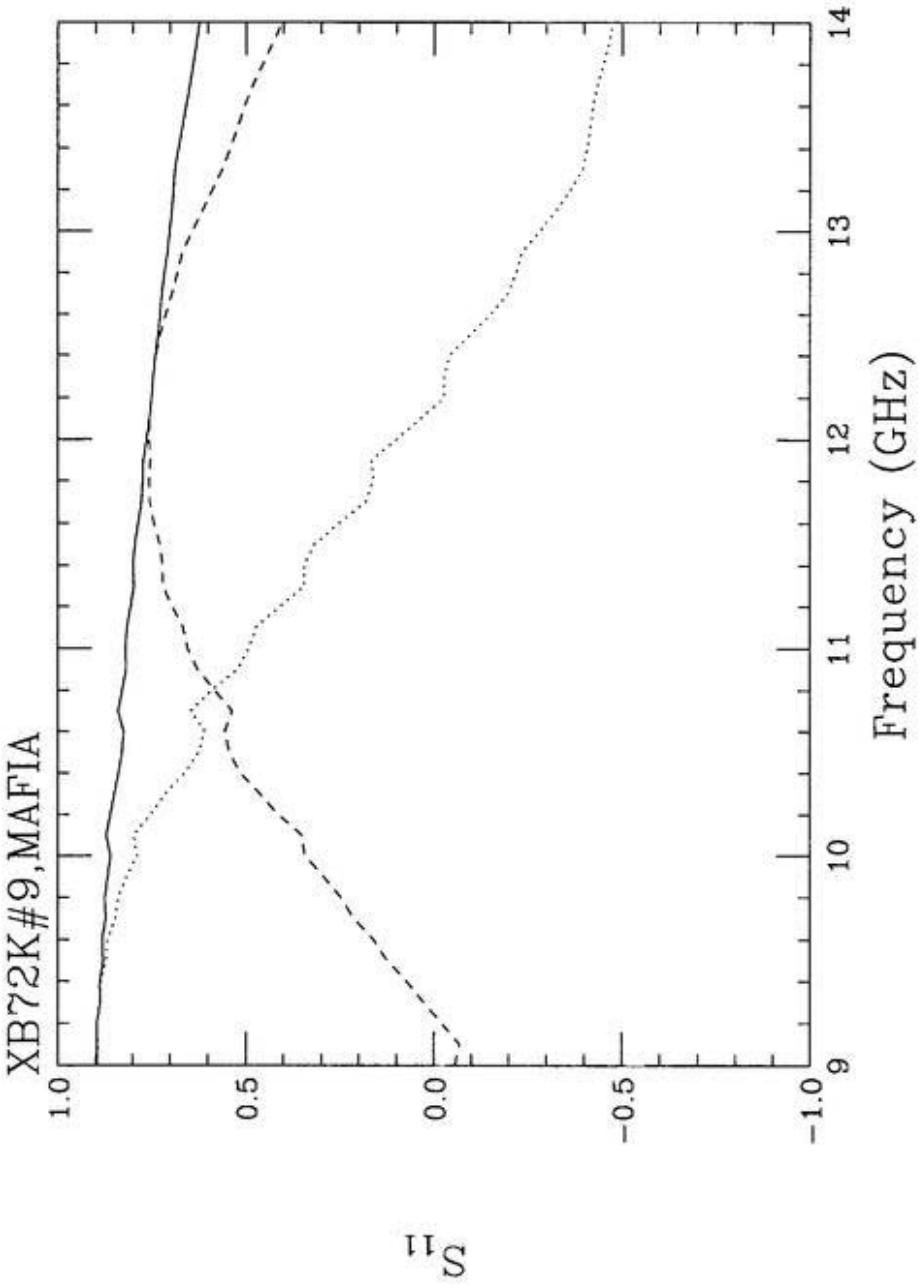

Figure 2.6: Reflection coefficient(S_{11}) as a function of frequency for the XB72K No. 9 output structure. The dotted and broken lines are the real and imaginary parts, respectively.

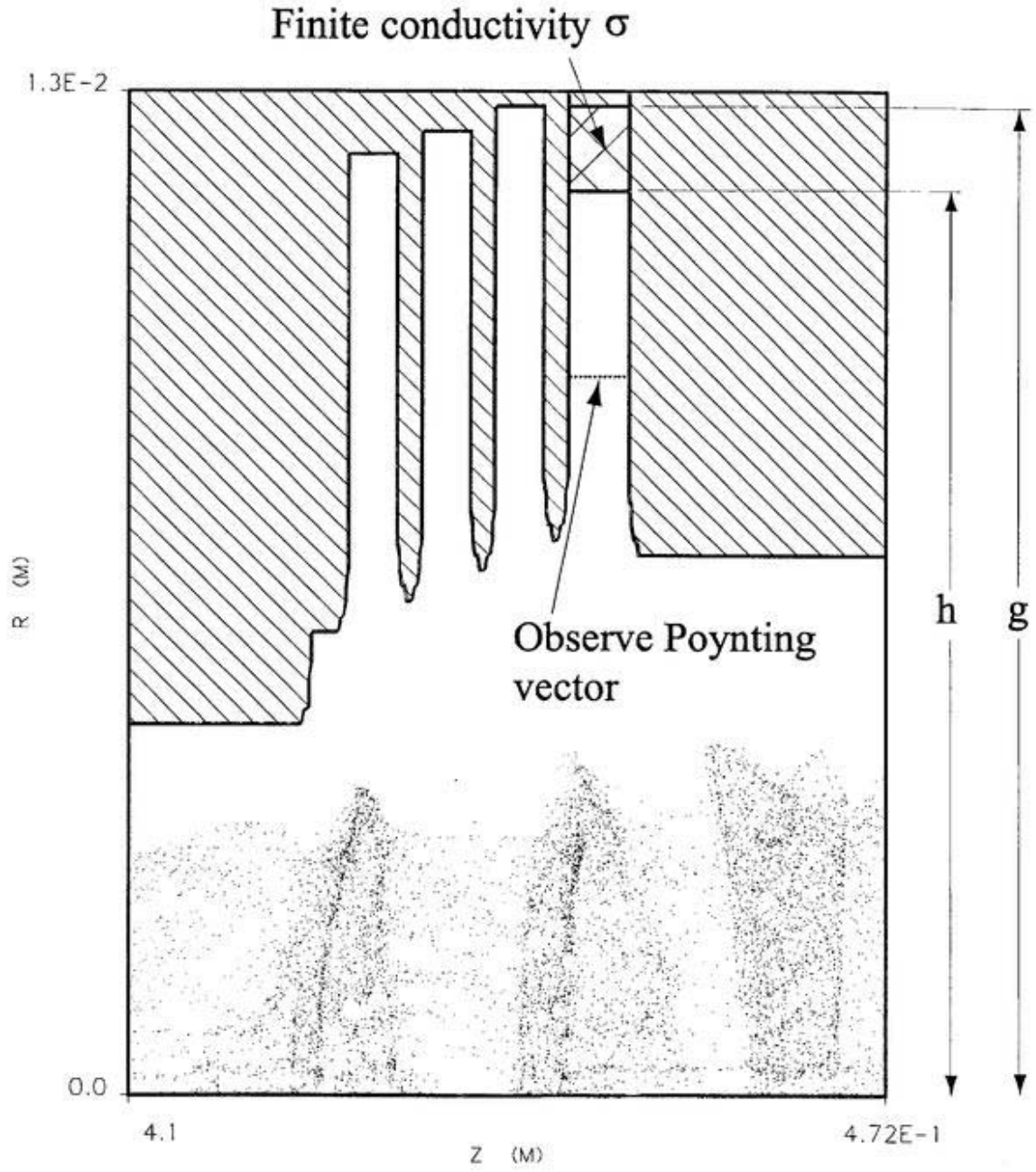

Figure 2.7: Example of MAGIC2D simulation. A finite conducting material is set in the coupler region to match the reflection coefficient(s) to the value calculated by MAFIA. The output power is calculated from the Poynting vector below the material.

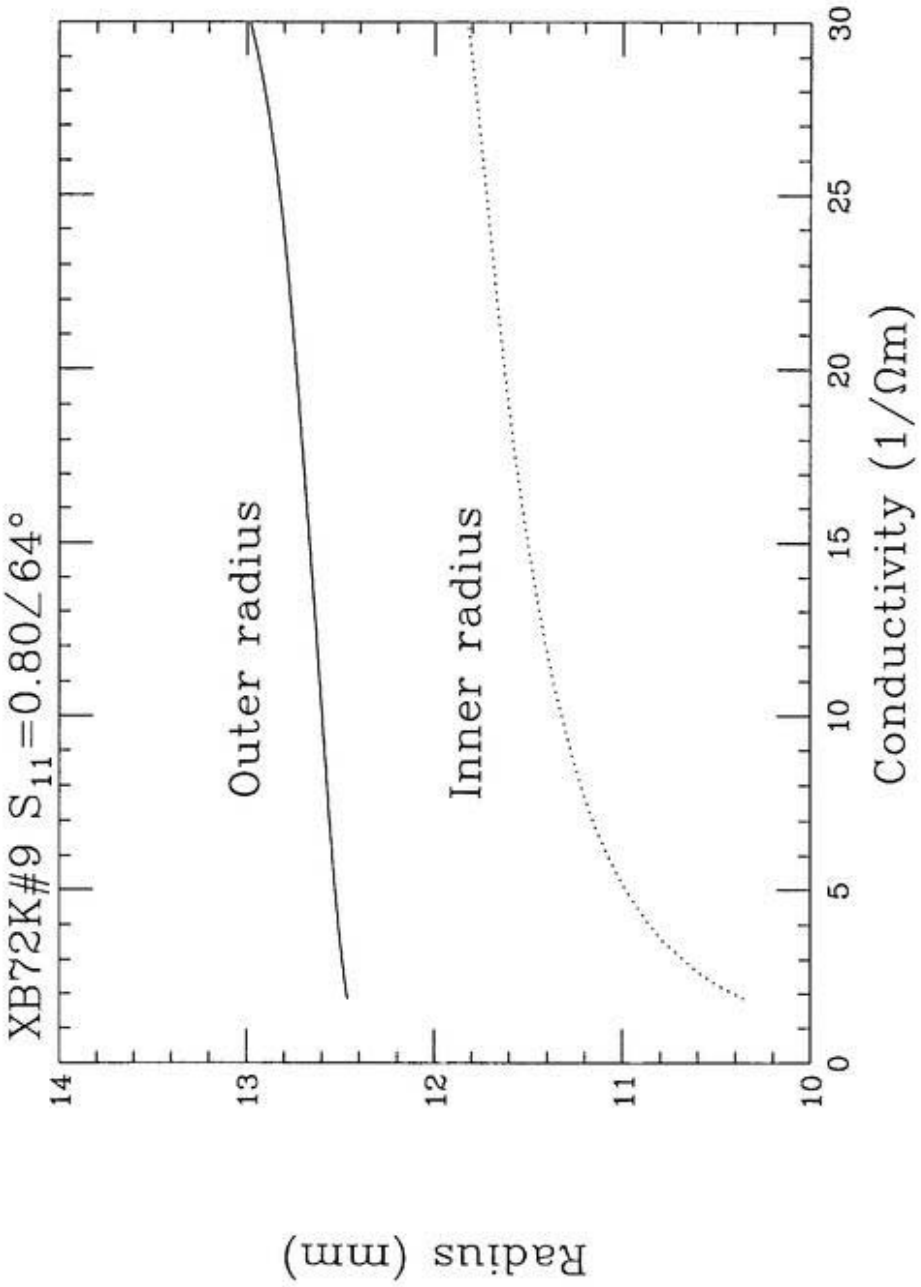

Figure 2.8: Parameters of a finite conducting material for reflection coefficient $s = 0.8$, 64 deg. at 11.424 GHz.

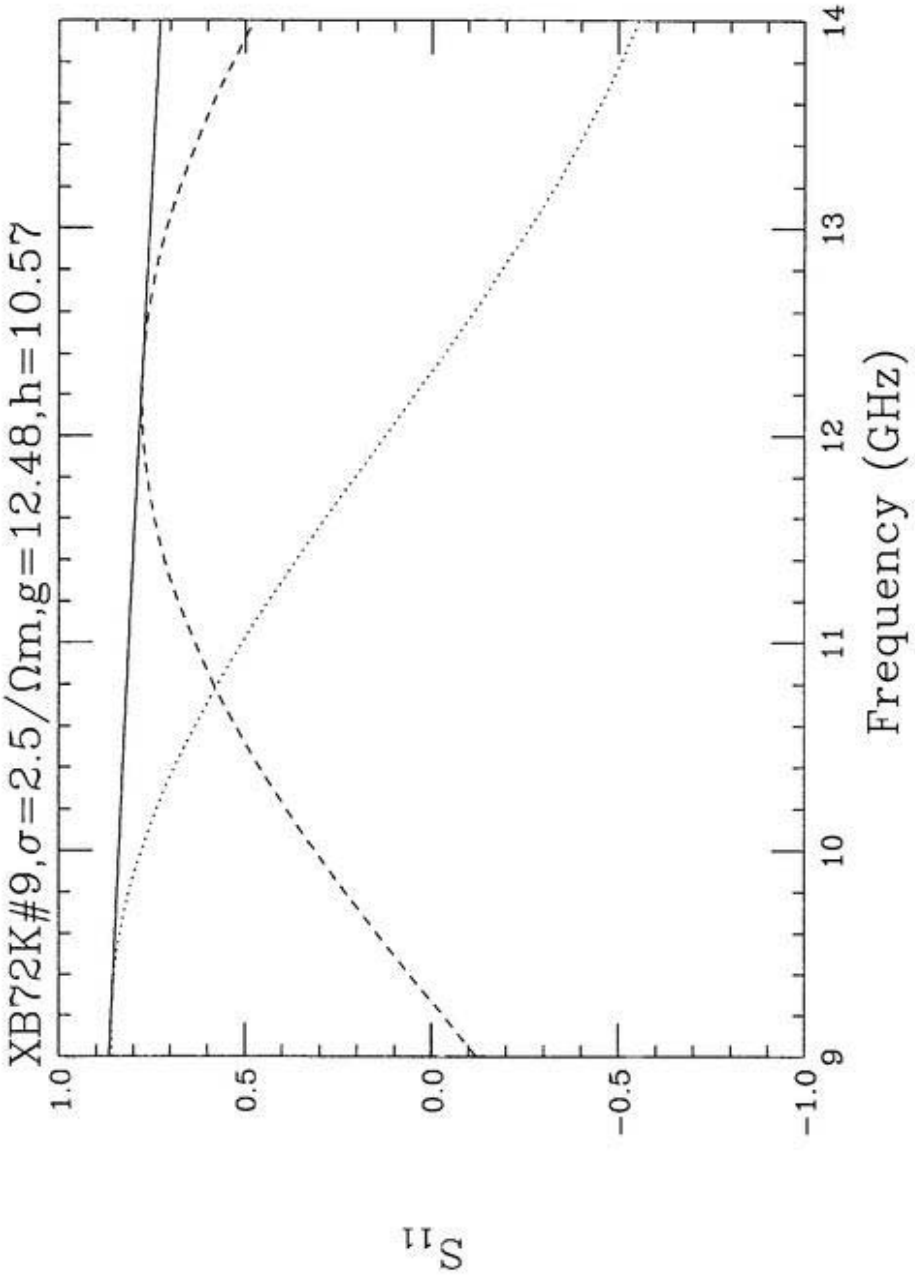

Figure 2.9: Reflection coefficient(s) vs. frequency for the two-dimensional model. The parameters of the finite conducting material are obtained by fitting s to the values 0.8, 64 deg. at the operating frequency(11.424GHz).

Chapter 3

MAGIC2D Simulation

We described a method for creating an axially symmetric model of the klystron output structure in the previous chapter. In this chapter, this method is evaluated by comparing the measured output power and the simulated one with the X-band klystrons, especially with the KEK No. 9 klystron.

We used MAGIC2D for the simulation. Due to the limitation of the grid number in the code, we divided the whole klystron structure into three parts (the electron gun, the bunching section, and the output structure) and simulated them from upstream. The separation is convenient if we change the parameters of the downstream parts, because we do not need to recalculate the upstream part.

In Section 1, we briefly describe the simulation procedure of the XB72K electron gun.

The simulation procedure of the bunching section of the XB72K No. 9 klystron is described in Section 2.

The simulation of the No. 9 klystron output structure is described in Section 3. There are an infinite number of choices of the parameters of the finite conducting material for a given reflection coefficient. The dependence of the output power on these parameters are discussed. The output powers by MAGIC2D are compared with the measured values.

For the input cavity, the relation between the gap voltage and the drive power should be known to calculate the gain. This issue is discussed in Sections 2 and 3.

3.1 Electron Gun

S. Michizono[10] simulated an electron gun. Since electrons are emitted from the surface of the cathode meshes in the MAGIC simulation, the roughness of the electron emission surface of MAGIC is greater than that of EGUN, which causes a large irregularity of the electron flow around the emission region. He made two simulations to reduce the roughness on the cathode surface. A 'large-area' simulation was made at first with a coarse mesh to obtain the voltage distribution on the gap between the wehnelt and the anode. Then, a 'small-area' simulation with a fine mesh was made with the gap voltage distribution by the 'large-area' simulation. In this simulation, the mesh sizes at the cathode were carefully chosen so as to make the cathode surface smooth. The simulation time step was chosen to be 1/360 of one period. Figure 3.1 shows the particle trajectories by the 'small-area' simulation. Electrons and a space-charge wave were 'exported' at the right-hand side of the geometry, and saved to some files. These files were used in bunching-section simulations.

The simulated results were compared with the measurements and EGUN simulations. He found that the perveance of the gun by MAGIC2D agreed with the measured value better than that by EGUN.

3.2 Bunching Section

The bunching section of the XB72K No. 9 klystron was simulated by S. Matsumoto[9]. As shown in Figure 1.1, there is one input cavity, two gain cavities and one penultimate cavity in this klystron. Particles and the field were imported from files which were created by the electron-gun simulation. Transmitted particles and the field were exported and saved to the files for the output-cavity simulation. Since some drive power is applied to the input cavity, the simulation methods for this cavity and for the other cavities are different. These methods are described below.

3.2.1 Input Cavity

In the input cavity, several hundred watts of RF waves modulate the velocity of the electron beam. Unfortunately, there is no direct method to simulate the input cavity in MAGIC2D. Thus, we applied some RF voltage at the gap to emulate it. In order to calculate the gain, we had to find out the

Resonant Frequency	11.424 GHz
Beam voltage	550 kV
Beam current	489 A
Q_0	5961
Q_{ext}	110
$R/Q(r = 0\text{mm})$	157 Ω
$R/Q(r = 3\text{mm})$	120 Ω
$R/Q(r = 5.6\text{mm})$	61 Ω
$\tilde{Q}_b^{-1}(r = 3\text{mm})$	$0.00572 + 0.00041i$

Table 3.1: Parameters of XB72K first cavity

relation between the gap voltage and the drive power. We used the method shown in Appendix D to estimate the gain. The parameters for the first cavity are given in Table 3.1. The beam from the electron gun has hollow-like distribution with about a 3mm radius. According to Eq. (D.23), the relation between the gap voltage (V_g) and the drive power (P_{in}) is

$$V_g(\text{kV}) = 2.4 \times \sqrt{P_{in}(\text{W})/300.} \tag{3.1}$$

3.2.2 Gain Cavities and Penultimate Cavity

The resonant frequencies of the cavities are shifted from the operating frequency, as shown in Table 3.2. In the simulation, these were tuned by small changes in the cavity outer radii. The unloaded quality factor of the cavities was infinity in the simulation. This was not a problem for this case, because the quality factor due to the electron beam $Q_b = 1/Re(1/\tilde{Q}_b)$ was far less than the unloaded quality factor(Q_0). Table 3.2 gives the quality factors of all the cavities calculated by using SUPERFISH. In this table, the material of the cavities is copper. If stainless steel is used, the unloaded quality factor(Q_0) becomes smaller by a factor of 6. In that case, the effect of Q_0 must not be neglected.

The simulation time of this section depends on Q_b. The damping time(τ) based on linear theory is

$$\frac{\tau}{T_0} = \frac{1}{\pi(1/Q_0 + 1/Q_b)} \simeq \frac{Q_b}{\pi}, \tag{3.2}$$

cavity No.	Δf(MHz)	Q_0	Q_b
1 (input)	0	5961	175
2 (gain1)	+12	4393	203
3 (gain2)	+26	6312	182
4 (penultimate)	+376	8639	179

Table 3.2: Quality factors of the cavities of XB72K

where T_0 is the period of one RF cycle. A typical simulation time was around 200 RF cycles, which is close to Q_b.

3.2.3 MAGIC2D Simulation of Bunching Section

We divided the bunching section into two parts because of a limitation of the number of grids of MAGIC2D. Figure 3.2 shows the beam trajectory in the first part of the No. 9 bunching section. Figure 3.3 shows the beam trajectory in the second part of the No. 9 bunching section. Figure 3.4 shows the normalized RF current in the No. 9 klystron. The maximum value of I_1/I_0 was around 1.2, which was much smaller than 1.55 of the SLAC XL-4.

3.3 Output Structure

The two-dimensional model which we are using was described in the previous chapter. The reflection coefficient(s) at the cell is assumed to be S_{11}, because the reflection coefficient(r) in Eq. (2.6) is ideally zero. The parameter S_{11} is $0.80\angle 64^o$ at 11.424GHz for the XB72K No. 9 structure. There are an infinite number of choices for the outer radius(g), the inner radius(h), and the electric conductivity(σ) of the finite conducting material for a given $s = S_{11}$, as shown in Figure 2.8.

In a sense, h and σ are considered to be essential parameters and g to be a provisional parameter, based on an analogy of resonant cavities. This is not true for this case because the electric conductivity(σ) is small. In our case, the skin depth(δ) is

$$\delta = \sqrt{\frac{2}{\sigma\omega\mu_0}} = 1.5\text{mm} \tag{3.3}$$

S_{11}	σ (1/Ω m)	g (mm)	h (mm)	P_{out} (MW)	E_{max} (MV/m)	$(E/B)_{r=8.2\text{mm}}$ (MV/Tesla m)	s
$0.8\angle 64^o$	2.5	12.48	10.57	83.8	97.5	$308.7\angle 96.2^o$	$0.87\angle 57.7^o$
$0.8\angle 64^o$	13.3	12.64	11.45	89.5	98.8	$311.4\angle 97.0^o$	$0.86\angle 58.3^o$
$0.8\angle 64^o$	24.1	12.81	11.71	91.5	99.1	$320.1\angle 98.3^o$	$0.83\angle 60.4^o$
$0.8\angle 64^o$	30.3	13.00	11.83	93.1	94.5	$323.4\angle 100.5^o$	$0.79\angle 61.2^o$

Table 3.3: MAGIC2D simulation results for No. 9 klystron. Beam voltage is 550kV.

when $\sigma = 10/\Omega$ m, which is much larger than the values for the cavities. Since the skin depth is the penetration depth of the electromagnetic field into the material, the field at $r = g$ is not negligible.

On the other hand, the skin depth should be larger than the mesh size so as to make a reasonable simulation. In our case, the mesh size is around 0.2mm, which satisfies the above requirement.

We made simulations with some parameter sets. We derived the output power using the Poynting vector below the finite conducting material. Some formulae are collected in Appendix E. The result is given in Table 3.3. The output power was varied by about 10%, whereas the maximum electric field was varied by about 5%. We observed the electric field and the magnetic flux density at r =8.2mm. The ratios of the electric field and magnetic flux density (E_z/B_ϕ) are also given in the table. The analytical value of E_z/B_ϕ at r =8.2mm is

$$\frac{E_z}{B_\phi} = \frac{i}{c}\frac{H_0^{(1)}(kr) + sH_0^{(2)}(kr)}{H_1^{(1)}(kr) + sH_2^{(2)}(kr)} = 336\angle 100^\circ\text{MV/m Tesla.} \qquad (3.4)$$

The reflection coefficient(s) in the simulation was estimated from E_z/B_ϕ and Eq. (3.4). It can be seen from the eighth column of Table 3.3 that the values of s are dependent upon the choice of σ. For the No. 9 output structure, a large σ seems to be preferable, since the reflection coefficient(s) is close to the desired value ($s = 0.8\angle 64^o$).

We think that the discrepancy in the reflection coefficients is due to two reasons. The first reason is the numerical error. Since the mesh size is 0.2mm in this case, we have only 5 or 6 mesh lines in the r direction. This situation can be improved by reducing the mesh size, but the time step should be reduced in that case in order to satisfy the Courant stability criterion:

$v\Delta t \leq 1/\sqrt{1/(\Delta r)^2 + 1/(\Delta z)^2}$. The derivation of this criterion is shown in Appendix F. Thus, if one needs to reduce the mesh size, one has to reduce the time step and perform a full klystron simulation again. It is difficult to do so because of the limitation on computer resources. The second reason is that the field in the fourth cell is not pure TM0*0. In any case, the output power is almost the same if $\sigma \geq 10/\Omega$m. We chose ($\sigma = 24.1/\Omega$m, $g = 12.81$mm, $h = 11.71$mm).

Figure 3.5 shows the beam trajectory in the No. 9 output structure.

Figure 3.6 shows the saturated output power as a function of the cathode voltage. There were two measurements. The difference in the two measured values was a few percent. The saturated power by a MAGIC simulation varies with the choice of the finite conducting material. If we choose a material with $\sigma = 24.1/\Omega$m, the output power would coincide with the measurement within 10%.

Figure 3.7 shows the output power vs. drive power for the No. 9 klystron. In this measurement, the focusing field was changed from the design value so as to optimize the output power. If we use the relation of Eq. (3.1), the curve by MAGIC simulation does not agree with the measurement. Since the shapes of the curves are similar, they agree if another voltage-power coefficient is chosen. Curves with a coefficient of 3.43kV/300W are also shown in Figure 3.7. It can be seen that the measured values are better fitted with this coefficient than with the calculated value.

We thought that this discrepancy is due to the following reasons:

- The resonant frequencies of the cavities in MAGIC2D simulation are different from the design values.
- The static magnetic field by the solenoid coils in the simulation is different from the actual field.

We changed the outer radii of the idler cavities or the static magnetic field slightly, and conducted simulations. The results are shown in Figure 3.8. If the outer radii of the idler cavities are increased by 0.01mm, the resonant frequencies are decreased by about 10 MHz. In this case, the curve shifted to the left. This is reasonable because the original resonant frequencies of the gain cavities are shifted from the operation frequency by +12 MHz and +26 MHz. If the outer radii of the idler cavities are increased by 0.05mm, the resonant frequencies are decreased by about 50 MHz. In this case, the curve is shifted to the right; this is also reasonable. From these calculations, we

thought that the resonant frequencies of the cavities were set with an error of 10 MHz order or smaller. The dotted curve in the figure shows the case when the static magnetic field by the solenoid coils are reduced by 2%. The curve is not very much different from the original. From the above data, we could not find any reason for the discrepancy.

We recently found that the measured microperveance of the electron gun is 1.4 (design value is 1.2), because the XB72K electron guns were manufactured at the factory with the geometry of the hot design. We think that the discrepancy of the gain is due to the perveance difference. We should check it sometime in future.

Figure 3.9 shows the saturated output power of the XB72K No. 8, 9 and the SLAC XL-4 klystrons. For these three klystrons, the saturated output powers by MAGIC2D simulations agreed with the measured values within 10%.

S. Matsumoto made a three-dimensional simulation by MAGIC3D with a virtual electron beam, and found that the output power is almost the same as the value calculated by our method. This result supports our method.

3.4 Summary

The model described in the previous chapter was evaluated empirically by comparing the output power with the measured value. The choice of a finite conducting material is important for obtaining a reasonable output power. The saturated output powers by MAGIC2D agreed with the measured values within 10% for the XB72K No.8,9 and the SLAC XL-4 klystrons.

The relation between the drive power and the gap voltage of the input cavity was calculated analytically. Although the gain curves of the simulation and the measurement were similar in shape, the voltage-power coefficient of the input cavity was different from the calculated value. This issue should be investigated sometime.

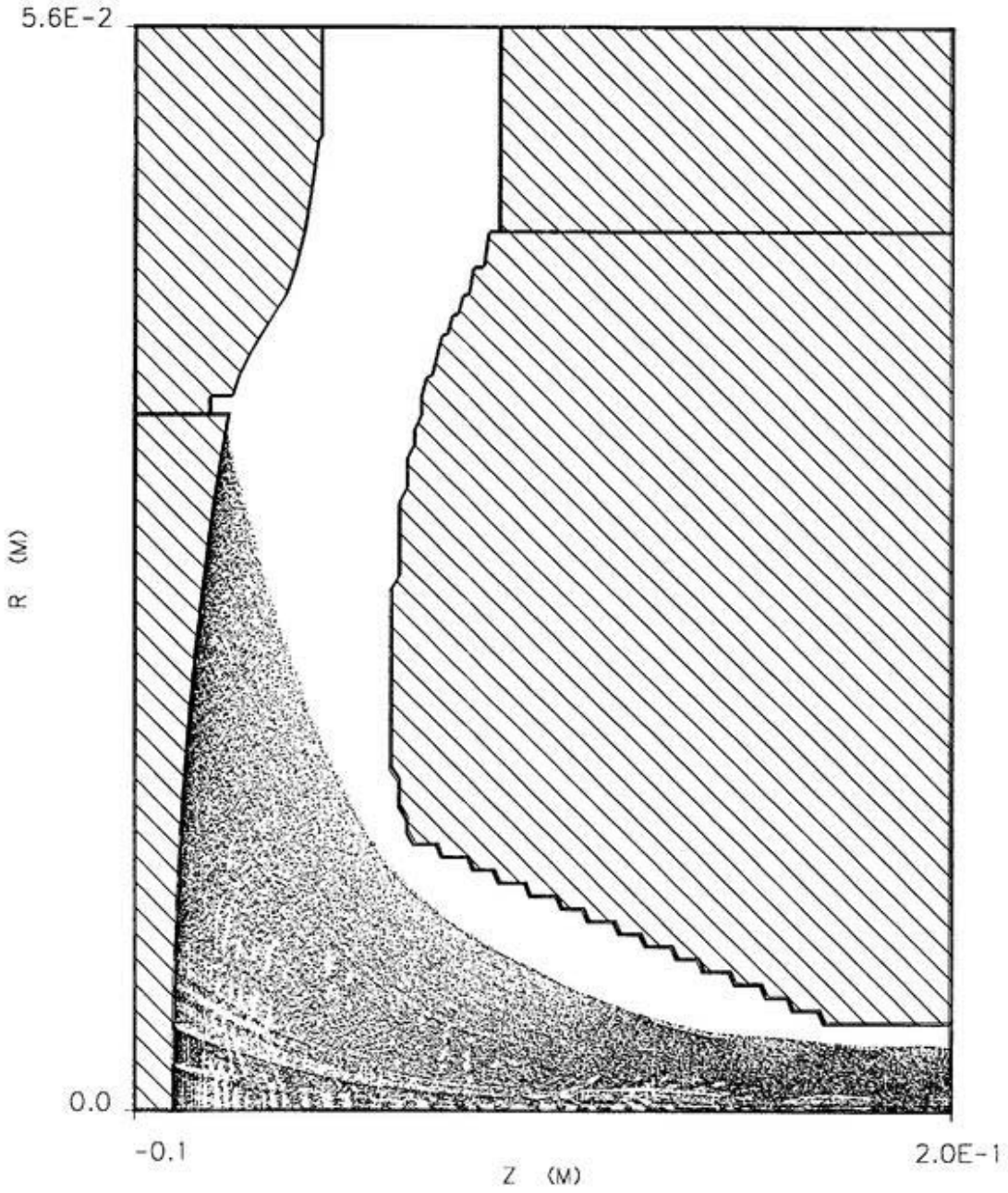

Figure 3.1: Particle trajectories of the XB72K No.9 electron gun by a MAGIC2D 'small-area' simulation. The applied voltage and beam current are 550kV and 490A, respectively.

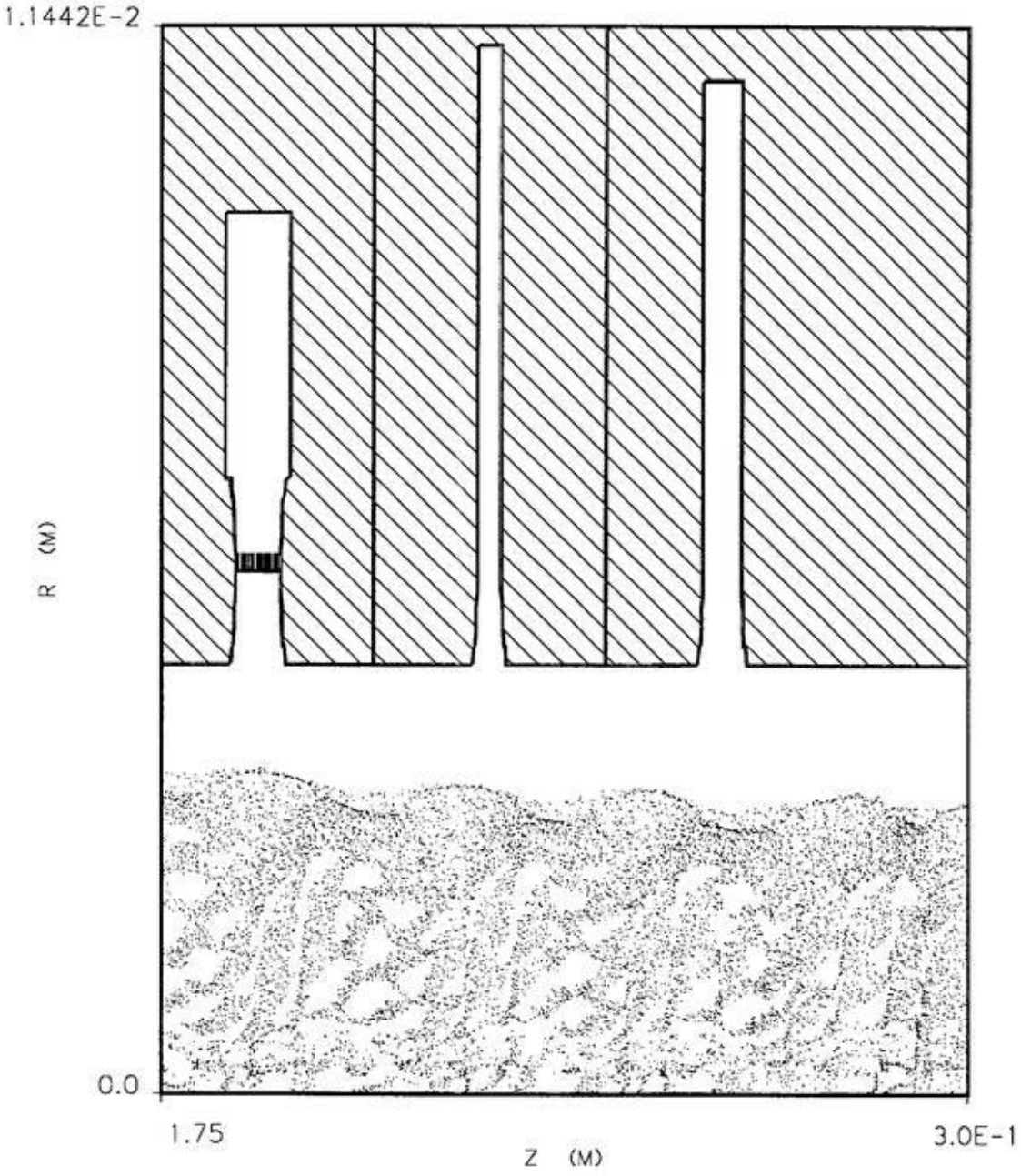

Figure 3.2: Beam trajectory in the XB72K No. 9 input cavity and two gain cavities.

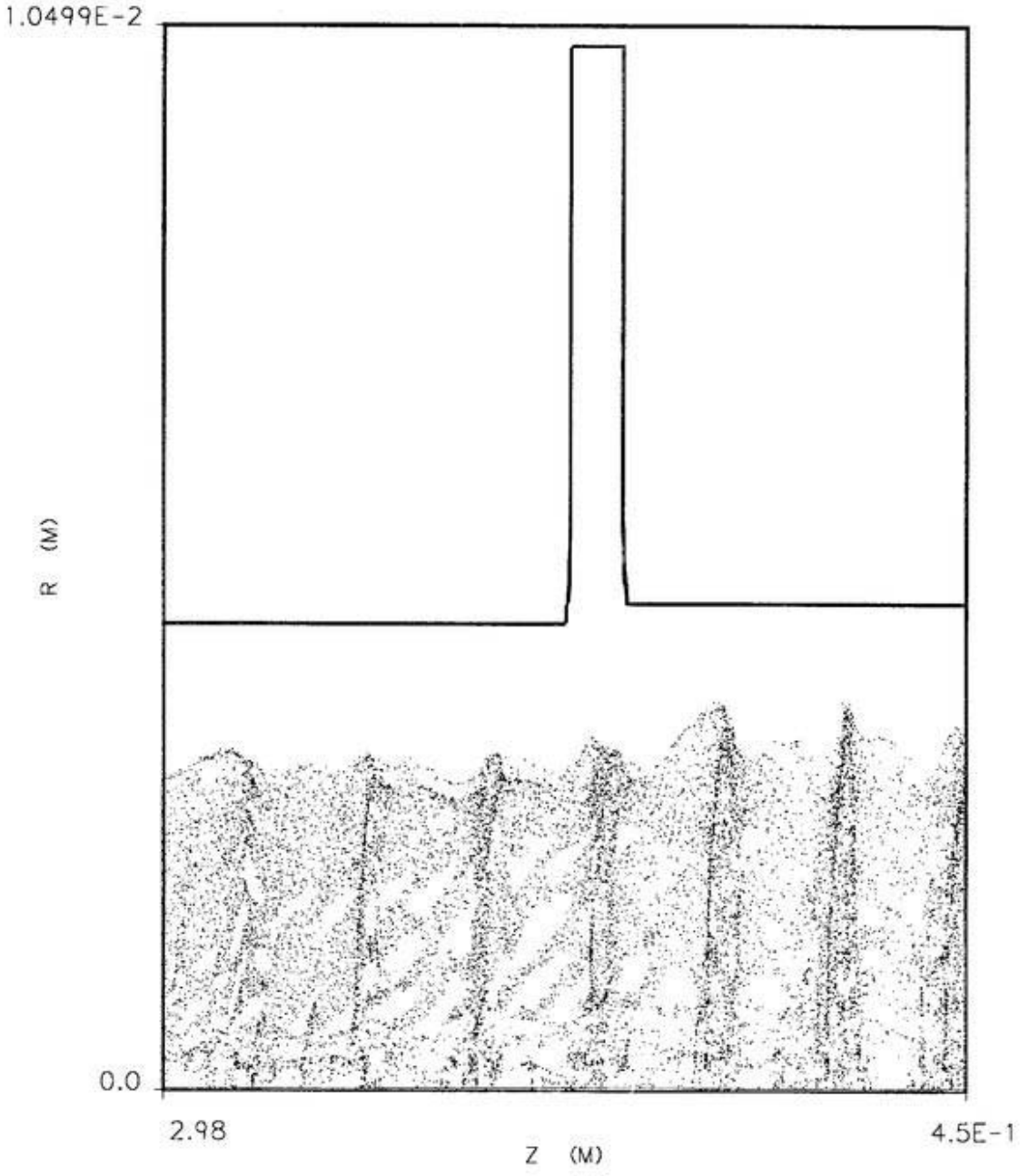

Figure 3.3: Beam trajectory in the second part of the XB72K No. 9 bunching section.

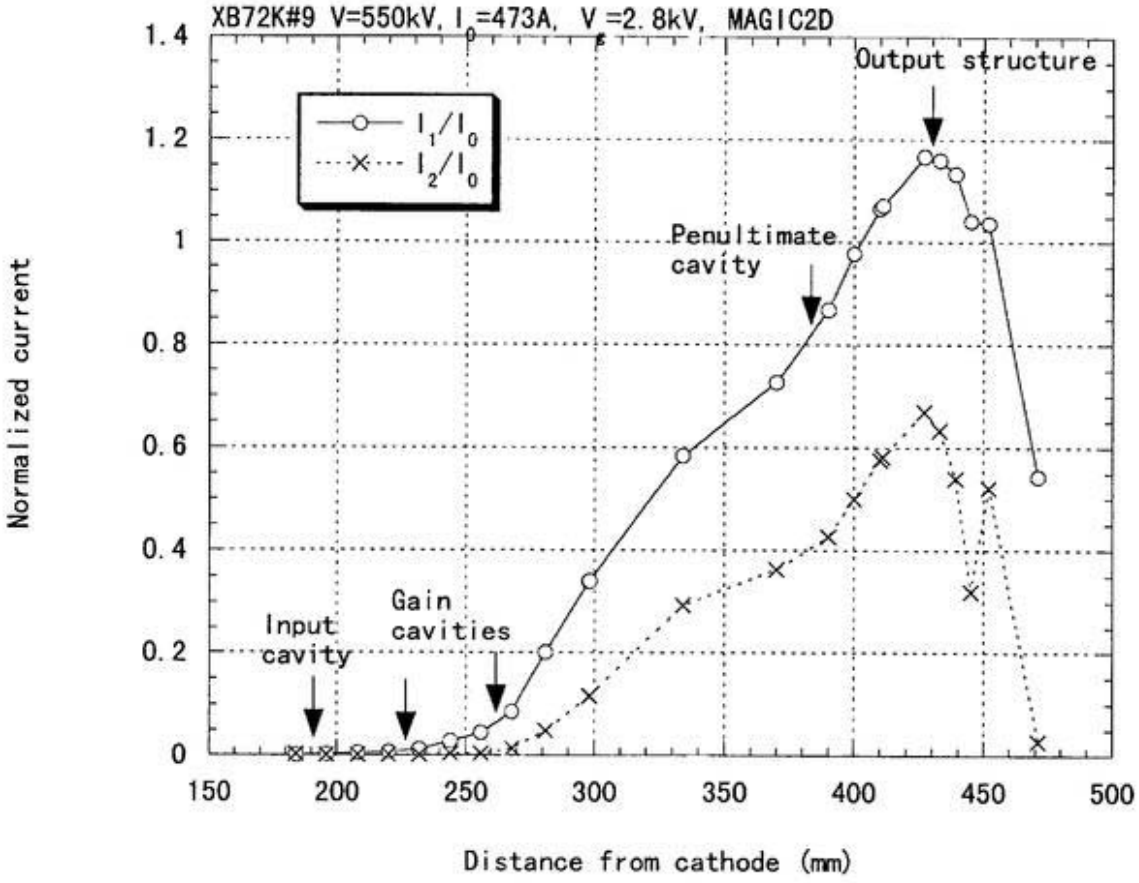

Figure 3.4: Normalized RF current in the XB72K No. 9 klystron by a MAGIC2D simulation.

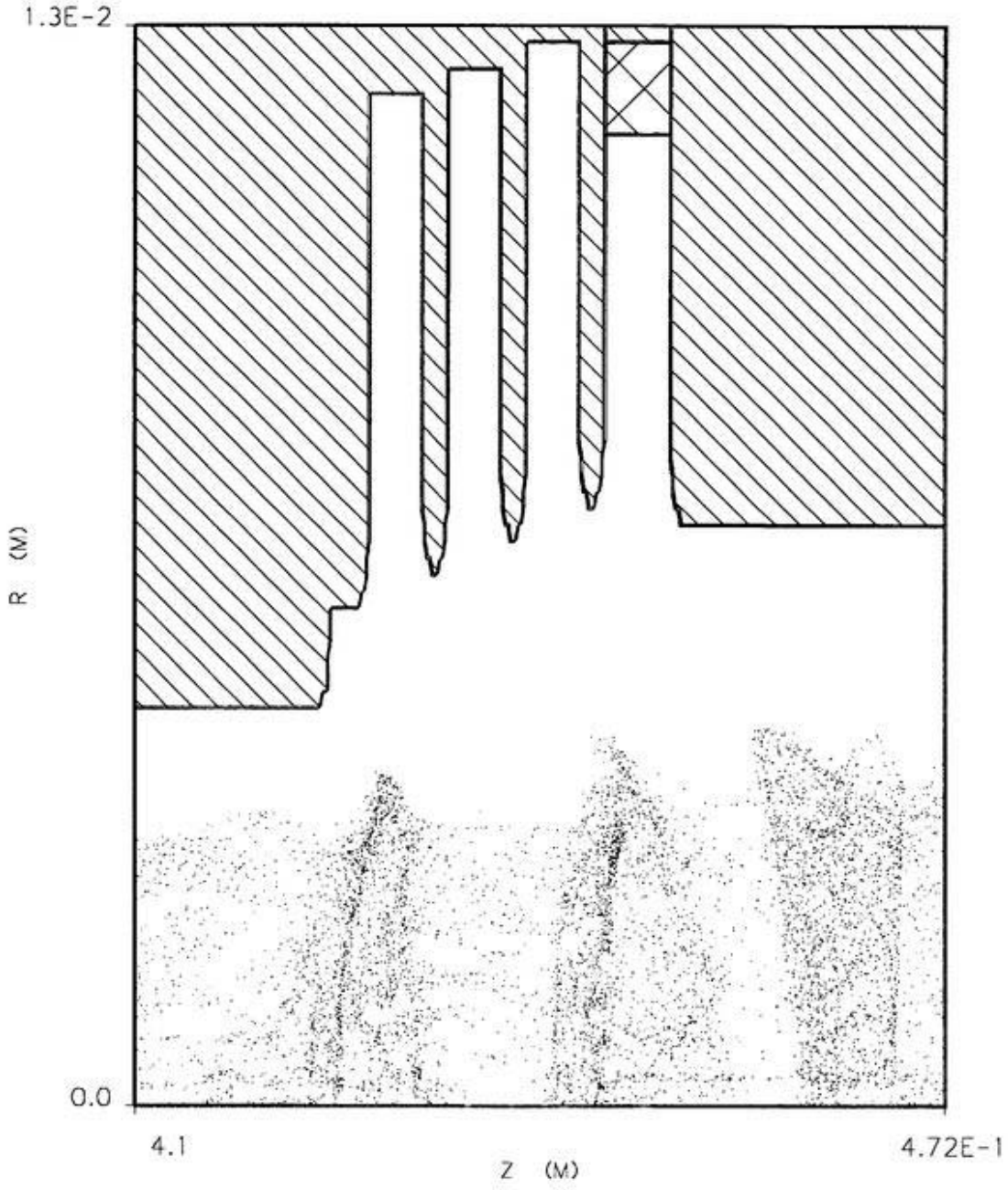

Figure 3.5: Beam trajectory in the XB72K No. 9 output structure.

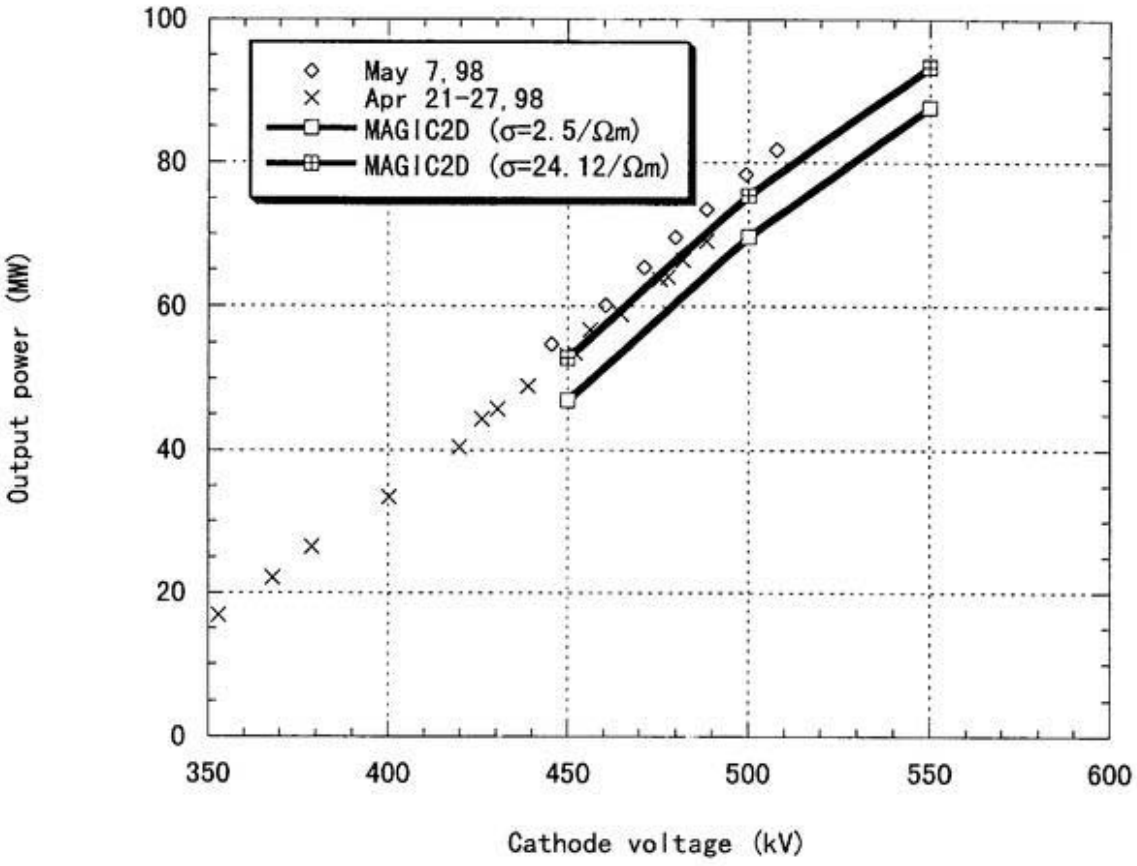

Figure 3.6: Saturated power of the XB72K No. 9 klystron. The design focusing field is used.

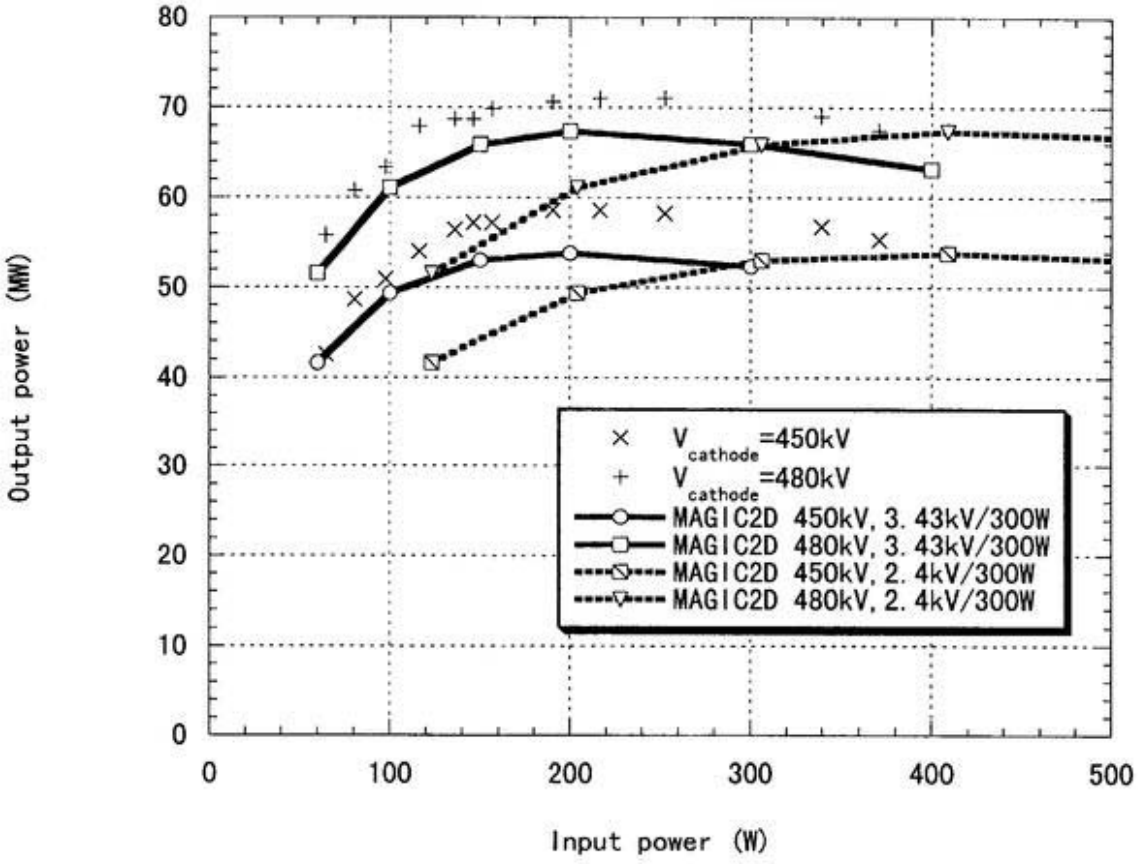

Figure 3.7: Output power vs. drive power for the XB72K No. 9 klystron.

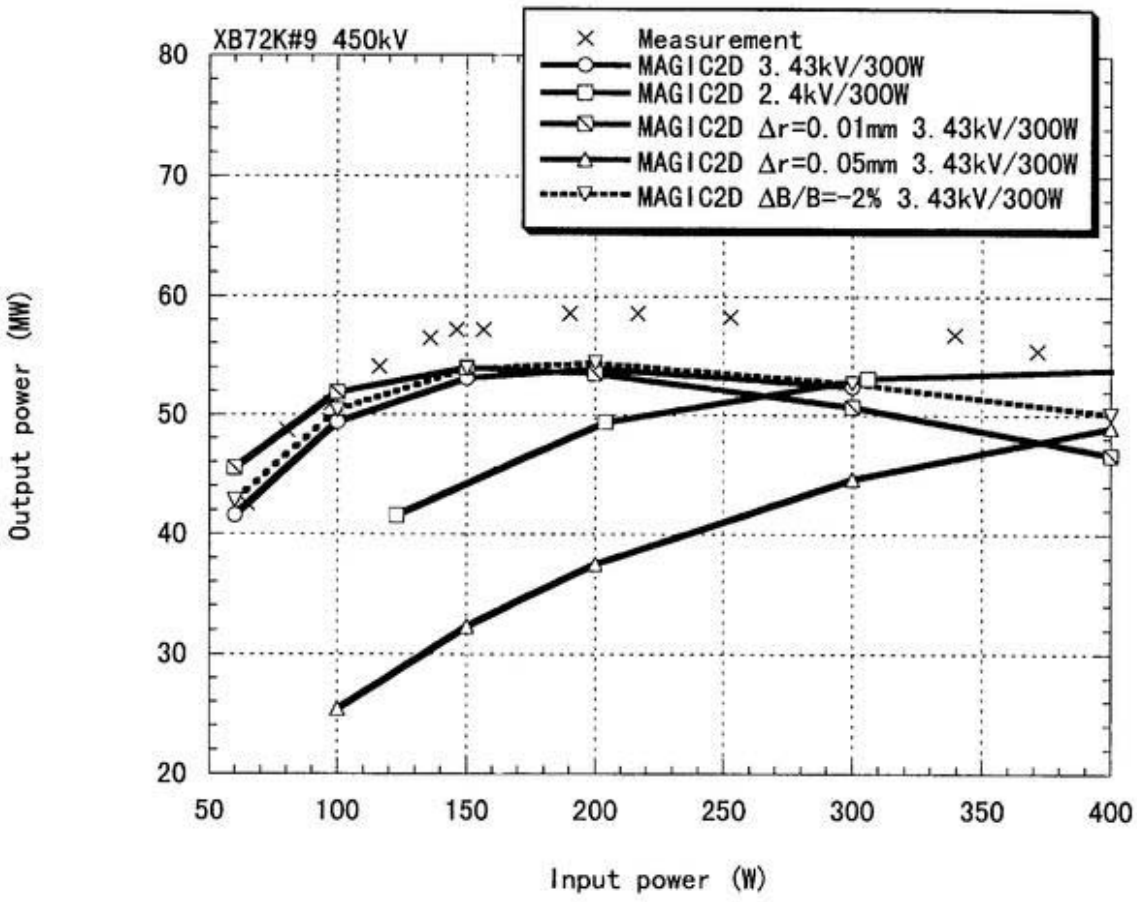

Figure 3.8: Output power vs. drive power for the XB72K No. 9 klystron with small changes in the cavity resonant frequencies or the static magnetic field.

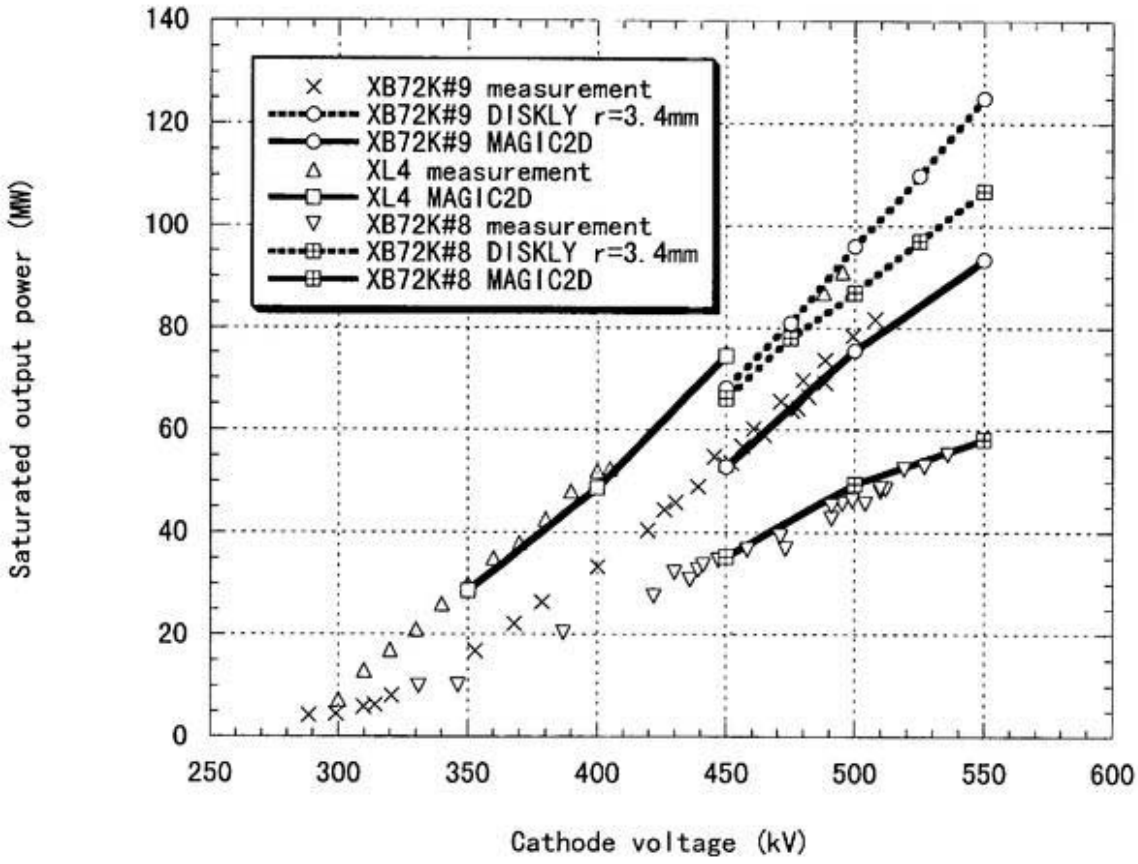

Figure 3.9: Saturated output power of the XB72K No.8, 9 and the SLAC XL-4 klystrons.

Chapter 4

Design of No. 10 Klystron

Our simulation method is described in the previous chapter. We next discuss the design a new klystron with our method. We examined the MAGIC2D simulation output of the No. 9 klystron and found that the bunching section and the output structure could be improved.

At the entrance of the output structure in the No. 9 klystron, the first harmonic of the normalized RF current is around 1.2, which is lower than $1.5 \sim 1.6$ of the SLAC XL-4 klystron. We therefore redesigned the bunching section so as to be $I_1/I_0 > 1.5$, as described in Section 1.

The maximum electric field in the output structure of the No. 9 klystron was 98MV/m at 550kV by MAGIC2D. If this structure is used for the No. 10 klystron with a larger RF current, the maximum electric field may exceed 100MV/m, which has a risk of an electric discharge. We thus designed a new output structure with a lower maximum electric field. The design process is described in Section 2.

4.1 Design of Bunching Section

We considered two parameters, the first harmonic of the normalized RF current (I_1/I_0), and the bandwidth, to improve the performance of the bunching section.

If the first harmonic component of the normalized RF current is higher, more electrons can be in phase with the electric field in the output structure, and the efficiency becomes higher. An ideal situation is a train of perfectly bunched electrons at the output cavity ($I_1/I_0 = 2, \Delta p/p = 0$). In this case,

we can make the efficiency 100% by using a good output cavity. This situation is impossible because: 1) the voltages in the cavities are sinusoidal (not saw-like shape) with time, and 2) the longitudinal space-charge force makes the bunch length longer. To make a saw-like voltage shape, second-harmonic cavities are used in some klystrons. We did not take this way because the cut-off frequency of the beam duct ($r = 4.6$mm) for the TM01 mode is 24.9 GHz, which is near to the frequency of the second harmonic. Instead of using the above method, we made long drift space between the gain cavities and the bunching cavities. After traversing the gain cavities, the electrons at the edge in phasespace go rather slowly to the focus because the modulation voltage is sinusoidal. Before they reach the nearest points to the focus, the other electrons reach their nearest points. At the nearest points, they exchange longitudinal momentum due to the longitudinal space-charge repulsion, and the longitudinal momentum spread becomes small. At the same longitudinal position, the electrons at the edge in the phasespace are still on the way to the focus. By placing the bunching cavities there, the center electrons are forced to stay around the focus, whereas the edge electrons are accelerated to reach the focus, and a high RF current can be obtained at the output cavity. By the above method, the effect of any nonlinearity of the modulation voltage can be reduced. The length of the drift space should be around a quarter of the space charge wavelength [7],

$$\frac{\lambda_p}{4} = \frac{\sqrt{1+g} - \sqrt{g}}{2} \sqrt{\frac{17kA}{I_0}} (\beta_0 \gamma_0)^5 \frac{2\pi c}{\omega} = 15\text{cm}, \tag{4.1}$$

where $g = 2\ln(\text{beam tube radius} \,/\, \text{beam radius})$. Even though we took the above way, we could not obtain $I_1/I_0 = 2$, because of the longitudinal space-charge repulsion. Practically, in case of the SLAC XL-4 klystron, the maximum normalized RF current is around 1.55 by the MAGIC2D simulation. We tried to reach this value. At the same time, we should reduce the momentum spread to obtain an efficient interaction between the beam and the electric field in the output cavity.

The bandwidth of our klystron should be wide enough to quickly respond when we invert the RF phase for the pulse compression. Assume that we shift the frequency by Δf and wait for time T. Then, the equation for the phase inversion is $2\pi(f + \Delta f)T = \pi + 2\pi f T$. From the above equation, the response time(T) is estimated to be $1/2\Delta f$. Since the response time is also limited by the damping times of the cavities ($\tau \simeq Q_b T_0/\pi$), T should be

case	gain	total length	bunch quality
$f_2 \sim +50$MHz,$f_3 \sim -50$MHz	larger	shorter	good
$f_2 \sim -50$MHz,$f_3 \sim +50$MHz	smaller	longer	better

Table 4.1: Comparison of the two cases for stagger detuning

around these values to obtain the optimized performance. In our case, since the damping time of the cavities is around 10 nsec, Δf is 50 MHz.

Based on the above considerations, we modified the bunching sections from the No. 9 as follows:

- One bunching cavity was added to increase the RF current.
- Distances between cavities were changed to increase the RF current.
- Frequencies of the gain cavities were changed to make the bandwidth of the klystron ± 50 MHz by stagger detuning.

Since the typical full simulation time of the bunching section is about one or two days, it is difficult to design it by MAGIC2D alone. The one-dimensional simulation code DISKLY was therefore used for a rough design. It takes a few minutes to run one DISKLY job on a PC.

The parameters were roughly determined by DISKLY. The criteria were 1) $I_1/I_0 > 1.5$ at 11.424GHz, 2) I_1 at 11.424GHz $\pm$ 50MHz is greater than 90% of I_1 at 11.424GHz, 3) the electric field strength should not exceed 40MV/m. The value of 40MV/m comes from the gap voltage of the No. 9 penultimate cavity by the DISKLY simulation. The following variables were changed: 1) the distances between cavities and 2) the resonant frequencies of the cavities. Since we did not encounter any beam instabilities at the idler cavities during the No. 1 - 9 klystron experiments, we decided to reuse their shapes, except for the outer radii for frequency tuning.

The resonant frequencies of two gain cavities should be 1) $f_2 \sim +50$MHz, $f_3 \sim -50$MHz, or 2) $f_2 \sim -50$MHz, $f_3 \sim +50$MHz to make the klystron wide-band. We tested both cases by DISKLY. Comparisons of the two cases are tabulated in Table 4.1. If the beam traverses the cavity with the resonant frequency being lower than the operating frequency (capacitively detuned), the beam will at first be debunched, and then be bunched again. Therefore, for case 2), the RF current at the third cavity is low, and the induced voltage

cavity number	f_{TE111} (GHz)	f_{TM110} (GHz)
4 (bunching1)	14.435	16.548
5 (bunching2)	14.729	16.847

Table 4.2: Resonant frequencies of the transverse modes of the bunching cavities

of the third cavity is also low. This makes the gain of case 2) small. To make the induced voltage higher, one should either increase R/Q of the cavity or add cavities. The R/Q value can be increased by using the reentrant structure. Since we decided to reuse the design of the XB72K cavities, we could not change R/Q. Since the total length of the bunching section is limited by the existing setup of the XB72K test stand, we could not add any additioned gain cavities. We thus decided to choose case 1).

We made simulations by MAGIC2D with the parameters determined by DISKLY. The original parameters by DISKLY were Δz = 190,40,40,120,40mm, Δf_r = 0,+50,−40,+400,+500MHz. The power from the output structure (XO#54) was 116MW.

We varied the resonant frequencies of the bunching cavities and compared them with the original design. Figure 4.1 shows the result. In this case the original design was the best.

We varied the distance between the second gain cavity and the first bunching cavity, and compared them with the original. Figure 4.2 shows the result. We chose 16cm, which is close to a quarter of the space-charge wavelength, $\lambda_p/4$ = 15 cm.

For actual klystrons, we sometimes encounter oscillations and beam instabilities. Sometimes the coupling of transverse modes between cavities is believed to be the origin of the instabilities. To avoid the risk of instabilities by the transverse modes, we tried to separate the resonant frequencies of the transverse modes of the bunching cavities as much as possible. We changed the edge radius of the first bunching cavity from 1mm to 2mm. The resonant frequencies of the TE111 and the TM110 modes were calculated by using the MAXWELL code, as shown in Table 4.2.

The parameters of the No. 10 klystron bunching section are tabulated in Table 4.3. Figure 4.3 shows a schematic view of the No. 10 klystron bunching section.

The DISKLY output is shown in Figure 4.4 The dependence of $(I_1/I_0)_{max}$

cavity number	z (mm)	Δf (MHz)	Q_0	$R/Q(\Omega)$ ($r = 0$mm)
1 (input)	190	-20	5880	160
2 (gain1)	230	+45	4400	75
3 (gain2)	270	-45	6300	121
4 (bunching1)	430	+300	8800	210
5 (bunching2)	470	+500	8660	211

Table 4.3: Parameters of No. 10 klystron bunching section

on the operating frequency is shown in Figure 4.5.

Figure 4.6 and Figure 4.7 show the beam profile in the first three cavities and two bunching cavities, respectively.

Figure 4.8 shows the normalized RF current by a MAGIC2D simulation.

Since one cavity was added and the distances between the cavities was made to be longer so as to increase the RF current, the length of the iron yoke for focusing the magnetic field should be increased by 4cm. We calculated the static magnetic field in the new focusing magnet system using POISSON. The currents of the four solenoid coils and the one bucking coil were changed so that the focusing magnetic fields of the no. 1-9 klystrons and the no. 10 klystron are the same around the gun region. The focusing magnetic field is shown in Figure 4.9. The magnetic flux density at the cathode is 41 Gauss.

4.2 Design of Output Structure

The following requirements should be satisfied for the output structure:

- The output power is 120MW or larger at 550 kV.
- The amplitude of the electric field should be low so as to avoid any RF discharge.

The threshold electric field for a RF discharge depends on many parameters, such as the frequency, a geometrical structure of the gap, cleanness of the surface, and vacuum pressure. W. D. Kilpatrick[6] studied the frequency dependence of the threshold electric field for continuous waves and obtained

the following equation in 1957:

$$f = 1.6 \times 10^{-3} E_{th,cw}^2 \exp(-8.5/E_{th,cw}), \tag{4.2}$$

where the frequency is in GHz and the threshold field is in MV/m. The above equation can be modified to

$$\begin{aligned} E_{th,cw}(\mathrm{MV/m}) &= \sqrt{f(\mathrm{GHz})/1.6 \times 10^{-3}} \exp(4.25/E_{th,cw}) \\ &\geq E_{th,cw,2} = 25\sqrt{f(\mathrm{GHz})}. \end{aligned} \tag{4.3}$$

Some accelerator physicists use $E_{th,cw,2}$ to design RF structures. In our case, $E_{th,cw} = 89$ MV/m. Since the several techniques has been improved since 1957, it is possible to exceed the Kilpatrick limit by a factor of 2 or more. Also, the threshold electric field is increased by pulsed operation. P. B. Wilson [19] showed a breakdown formula for short RF pulses based on the power flow at breakdown in a S-band resonant ring at SLAC,

$$E_{th} = E_{th,cw,2}\left[1 + \frac{4.5}{t^{1/4}(\mu\mathrm{s})}\right]. \tag{4.4}$$

In our case, if the pulse duration is 1.5 μ s, $E_{th} = 430$ MV/m. In the design of the X-band relativistic klystron output structure, G. A. Westenskow and T. L. Houck [18] used 80 MV/m at 50 nsec as the design limit. They explained that the reason of the low value is a poor vacuum, and claimed that they can reach 150 MV/m in the future.

As described above, the threshold electric field varies from 80 MV/m to 430 MV/m. Since their values do not contain any effect of the geometrical structure, we do not know whether they can be used or not in our case. Hence, we decided to use the maximum electric field in the SLAC XL-4 output structure calculated by MAGIC2D as the design limit. The simulated performance of the XB72K No.9 and the SLAC XL-4 output structures are given in Table 4.4. We decided to design the output structure with the maximum electric field of less than 100 MV/m.

To design the traveling-wave-type output structure, the following parameters should be fixed: 1) number of cells, 2) cell widths and the phase difference between cells, 3) reflection coefficient at the coupler, and 4) radii of the irises and the cells.

If the number of cells is larger, the interaction length becomes larger and the amplitude of the electric field can be lower. However, since the

output structure	mode	beam voltage (kV)	output power (MW)	maximum electric field (MV/m)	typical cell width (mm)
XB72K No. 9	$\pi/2$	550	84	98	4 or 5
SLAC XL-4	$\pi/2$	450	72	104	3

Table 4.4: Performances of the XB72K No.9 and SLAC XL-4 output structures calculated by MAGIC2D.

structure is more complicated, there should be more unwanted deflecting modes inside the output structure. The No. 9 output structure has 4 cells and the maximum electric field was 98 MV/m at 84 MW by MAGIC2D simulation. If we reduce the number of cell to 3, the maximum electric field may exceed 100 MV/m. If we add one cell to the No. 9 output structure, we would have more unwanted modes. Hence, we chose 4-cell structure.

For the cell width, we considered the following. For simplicity, we assumed that the electron bunch sees a constant longitudinal electric field of $-E$ while it is in the output structure. If the transverse motion is neglected, the equations for the electron motion are:

$$\begin{aligned} \gamma(z) &= \gamma_0 - \frac{eE}{mc^2}z, \\ \beta(z) &= \sqrt{1-1/\gamma^2}, \\ t(z) &= \int_0^z \frac{dz}{c\beta} = \frac{mc}{eE}(\sqrt{\gamma_0^2-1} - \sqrt{\gamma^2-1}), \end{aligned} \tag{4.5}$$

where γ_0 is the relativistic factor at the entrance of the cavity, z is the longitudinal distance from the entrance of the cavity, γ is the relativistic factor at z, and t is the time since the electron entered the cavity. In our case $\gamma_0 = 550/511 + 1 = 2.076$. We assume that the synchronized electron loses 80% of its energy in the cavity. At the exit of the cavity ($z = z_{exit}$), $\gamma_{exit} = 1 + 0.2(\gamma_0 - 1) = 1.215$. We consider a four-cell structure with a phase difference between cells of ϕ. The value of ϕ is $\pi/2$ for the output structures of the XB72K No. 9 and SLAC XL-4. The interaction time is $t = 4T_0\phi/2\pi$, where T_0 is one period. If ϕ is larger, the interaction time become longer. This means that the widths of the cavity cells can be made longer. We decided to choose $\phi = 2\pi/3 > \pi/2$. Then, the interaction time is

place	t (ps)	γ	Δz (mm)
entrance of the cavity	0	2.08	0
exit of the cell 1	29.2	1.83	7.51
exit of the cell 2	58.4	1.60	7.10
exit of the cell 3	87.5	1.40	6.50
exit of the cell 4	116.7	1.22	5.57

Table 4.5: Length of the cells calculated using Eq. (4.5).

$t = 4T_0/3 = 116.7$ps. By substituting this into Eq. (4.5), we obtain

$$E = \frac{3mc}{4eT_0}(\sqrt{\gamma_0^2 - 1} - \sqrt{\gamma_{exit}^2 - 1}) = 16.49\text{MV/m}. \tag{4.6}$$

The total length of the cavity is

$$z_{exit} = \frac{mc^2}{eE}(\gamma_0 - \gamma_{exit}) = 26.68\text{mm}. \tag{4.7}$$

Using Eq. (4.5), z at the exit of the cells can be calculated as shown in Table 4.5. If we assume that the width of the iris is 2mm, the width of the cell 4 should be shorter than 3.6mm. This is not desirable because the electromagnetic power from the 1-4 cells is concentrated in this region. We chose 4,4,4,5 mm and 2mm for the widths of the cells and the iris, which are the same as the values of the No. 9 structure. The total length of this structure is 1+4+2+4+2+4+2+5+1=25mm, which is almost the same as the value of Eq. (4.7). There may be two other possibilities:

- Use a backward-wave. The energy flows to cell 1. An output coupler can be installed on cell 1.
- Install a coupler to every cell. Then, the power is not concentrated on one cell. The powers from the couplers are combined somewhere.

We did not examine them this time.

The amplitude of the reflection coefficient of the TM0*0 mode, defined in Chapter 2, was 0.8 for the XB72K No. 8, 9 and the SLAC XL-4 klystrons. If this value is high, the coupling between the inside and the outside of the structure is reduced. Hence, the output power is reduced or the amplitude

of the electric field in the structure is increased. If this value is low, the coupling between the inside and the outside of the structure is increased, and the output power is easily affected by the reflection from the downstream of the rectangular waveguide. We chose 0.8 for the No. 10 klystron.

To determine the radii of the irises and the cells, we assumed the following:

- There is no energy flow to the previous cell.
- An electron bunch loses the same power, $P/4$, at each cell.
- The cell length is $z = 6$mm for all cells.
- The stored energies in the cells U are the same.
- The dispersion curve of the TM01 modes is sinusoidal.

From the second assumption, the energy flow through irises 1,2,3 are $P/4$, $2P/4$, $3P/4$. The average energy flows in cells 1,2,3,4 are $(0 + P/4)/2 = P/8, (P/4+2P/4)/2 = 3P/8, (2P/4+3P/4)/2 = 5P/8, (3P/4+0)/2 = 3P/8$. The group velocities($v_g$) for cells 1,2,3,4 are $zP/8U, 3zP/8U, 5zP/8U, 3zP/8U$. In the last cell, the quality factor(Q) can be approximated as

$$Q \simeq -\frac{\omega a}{c \ln |s|} \simeq 10, \tag{4.8}$$

where a is the outer radius of the 4. The derivation of the above equation is shown in Appendix G. Since $Q = \omega U/P$, the group velocities for cells 1,2,3,4 are $\omega z/8Q$, $3\omega z/8Q$, $5\omega z/8Q$, $3\omega z/8Q$. From the third assumption, frequency(f) is

$$f(\phi) = f_0 + \frac{1 - \cos(\phi)}{2}(f_\pi - f_0), \tag{4.9}$$

where f_0 is the frequency of the 0 mode, and f_π is the frequency of the π mode. The group velocity(v_g) is

$$v_g = \frac{d\omega}{dk} = 2\pi z \frac{df}{d\phi} = \pi z \sin\phi (f_\pi - f_0). \tag{4.10}$$

Hence, f_0 and f_π are

$$\begin{aligned} f_0 &= f - \frac{v_g}{2\pi z} \tan\frac{\phi}{2}, \\ f_\pi &= f + \frac{v_g}{2\pi z} \cot\frac{\phi}{2}. \end{aligned} \tag{4.11}$$

Frequencies f_0, f_π were calculated using SUPERFISH for each cell. The outer radii and the iris aperture were varied so as to fit the 0-mode and the π-mode frequencies to the above value.

Figure 4.10 shows the trajectory of the electron beam in this output structure, XO#0, by a MAGIC2D simulation. It can be seen that the radius of the first iris is smaller than the beam-duct radius. This causes electron interruption, and too much interaction occurs between the electromagnetic field in cell 1 and the electron bunch.

We thought that XO#0 was failure because the pure traveling wave was assumed. We decided to allow backward wave, and set the radii of the irises larger. We assumed that the group velocity(v_g) is kept constant for all cells,

$$v_g = \frac{zP}{U} = \frac{\omega z}{Q} = 4.3 \times 10^7 \mathrm{m/s}. \tag{4.12}$$

By using Eq. (4.11) and SUPERFISH, structure was fixed. Figure 4.11 shows the trajectory of the electron beam for this structure (XO#45). The output power from XO#45 was 119MW, which is almost sufficient for our requirement. Electric fields are observed at the points shown in Figure 4.11. The phases of the longitudinal electric fields in the cell 1 and 4 were almost the same, which means that this structure operated with $\phi = 2\pi/3$, as expected. The electric field at iris 3 (point 7) was high, as shown in Figure 4.12.

We made small changes to the XO#45 structure. Figure 4.13 shows the output power as a function of the radius of the irises. The radius of the irises of XO#45 is 7.6mm, which is the optimal value. Figure 4.14 shows the output power as a function of the argument of the reflection coefficient s. The argument of the reflection coefficient of XO#45 was 73 degrees, which was the optimal value. We also changed the radii of the aperture of the irises individually and ran MAGIC2D simulations, finding that the output powers by modified structures are the same level as or smaller than the output power by XO#45.

The shortcoming of XO#45 is the electric field at iris 3 is high. We changed the corner radii of the iris 3 and of the exit of the cell 4 from 1mm to 1.6mm (XO#87) in order to avoid the concentration of the electric field, and ran the MAGIC2D simulation. Figure 4.15 shows the electron-beam trajectory in the XO#87 output structure. The output power was 122MW. Figure 4.16 shows the electric field distribution in the XO#87 output structure. Electric field strength at iris 3 in XO#87 was reduced from XO#45. The highest value is 88MV/m at iris 3, which is sufficient for our purpose.

The resonant frequency of TE111-like mode of XO#87 was 11.284GHz, which is close to the operating frequency (11.424GHz). We decided to shift the frequency of the TE111-like mode to at least 200MHz below 11.424GHz. The resonant frequency of TE111-like mode largely depends on the radius of the aperture of irises 2 and 3. We changed the aperture radii of irises 1,2,3 from 7.6mm to 7.4mm,7.6mm,7.8mm, respectively (XO#105). The resonant frequency of TE111-like mode is 11.201GHz for XO#105. Figure 4.17 shows the electron-beam trajectory in the XO#105 output structure. The output power was 128MW with the particle distribution from the new bunching section. Figure 4.18 shows the electric field distribution in the XO#105 output structure. The highest electric field amplitude was 82MV/m at iris 3.

This output structure (XO#105) was built by TOSHIBA. They measured the scattering matrix between the two output ports by a network analyzer before brazing. They calculated the field distribution by HFSS and observed that a considerable amount of electric field of the TE111-like mode exists at the operating frequency. We decided to shift the frequency of the TE111-like mode to 500MHz below 11.424GHz. We changed the aperture radii of irises 1,2,3 to 7.6mm, 8.6mm, 7.8mm, respectively (XO#105m29). The resonant frequency of TE111-like mode was 11.201GHz for XO#105m29.

TE111-like mode may be excited by two mechanisms:

- The transverse displacement of the electron beam.
- Unbalance of the reflection waves from two output rectangular waveguides.

The kick angles were estimated for the XO#105 and XO#105m29 structures (see Appendix H).

Figure 4.19 shows the electron-beam trajectory in the XO#105m29 output structure. The output power was 120MW. Figure 4.20 shows the electric-field distribution in the XO#105m29 output structure. The highest electric-field intensity is 85MV/m at iris 3. Figure 4.21 shows the output power of the No. 10 klystron as a function of the drive power of the input cavity. The relation between the gap voltage and the drive power was discussed in the previous chapter. If we assume 3.4kV/300W, this klystron saturates when the drive power is 400W. Figure 4.22 shows the saturated output power of the No. 10 klystron as a function of the cathode voltage.

4.3 Summary

We designed the KEK XB72K No. 10 klystron. A bunching section with $I_1/I_0 > 1.5$ at the entrance of the output structure was designed by using DISKLY and MAGIC2D. An output structure with 120MW at 550kV was designed by a simple empirical method.

This klystron was manufactured at TOSHIBA Corporation. We will test it from January, 1999.

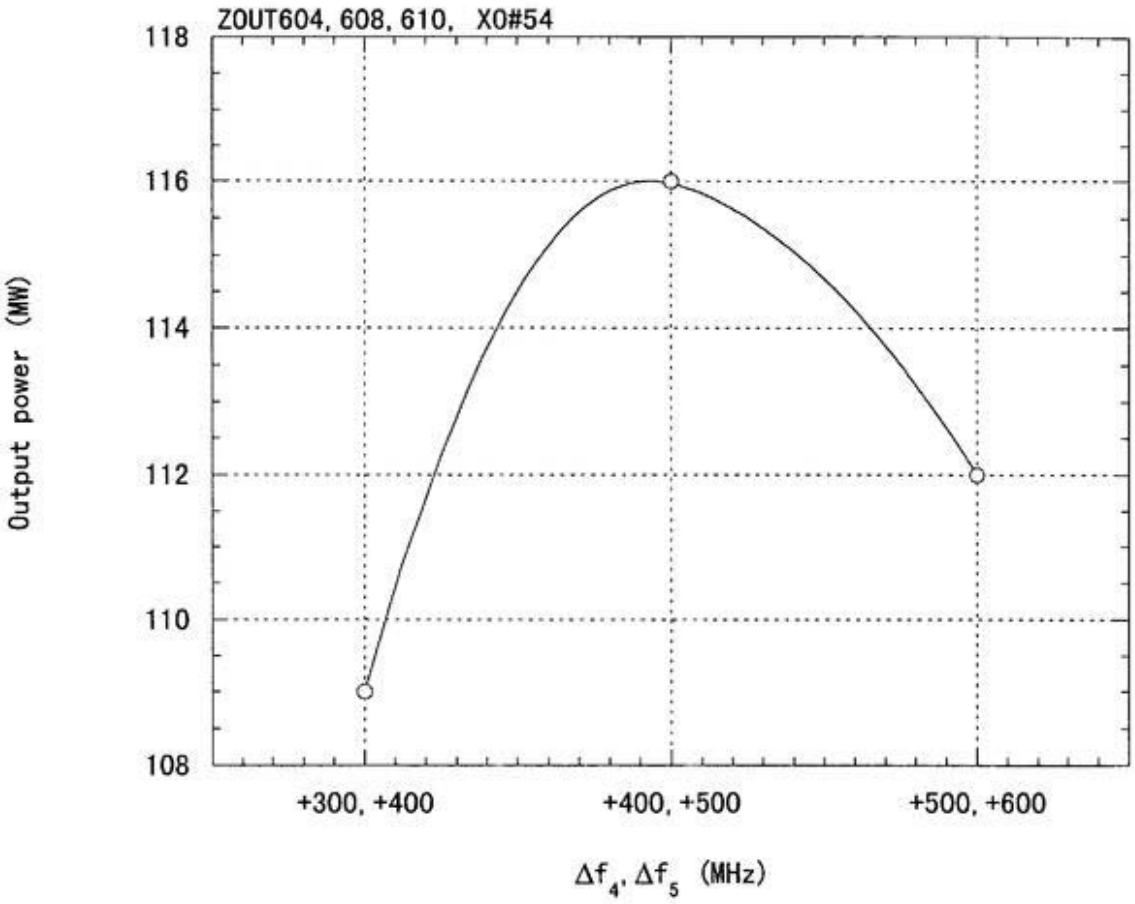

Figure 4.1: Output power vs. resonant frequencies of bunching cavities by a MAGIC2D simulation.

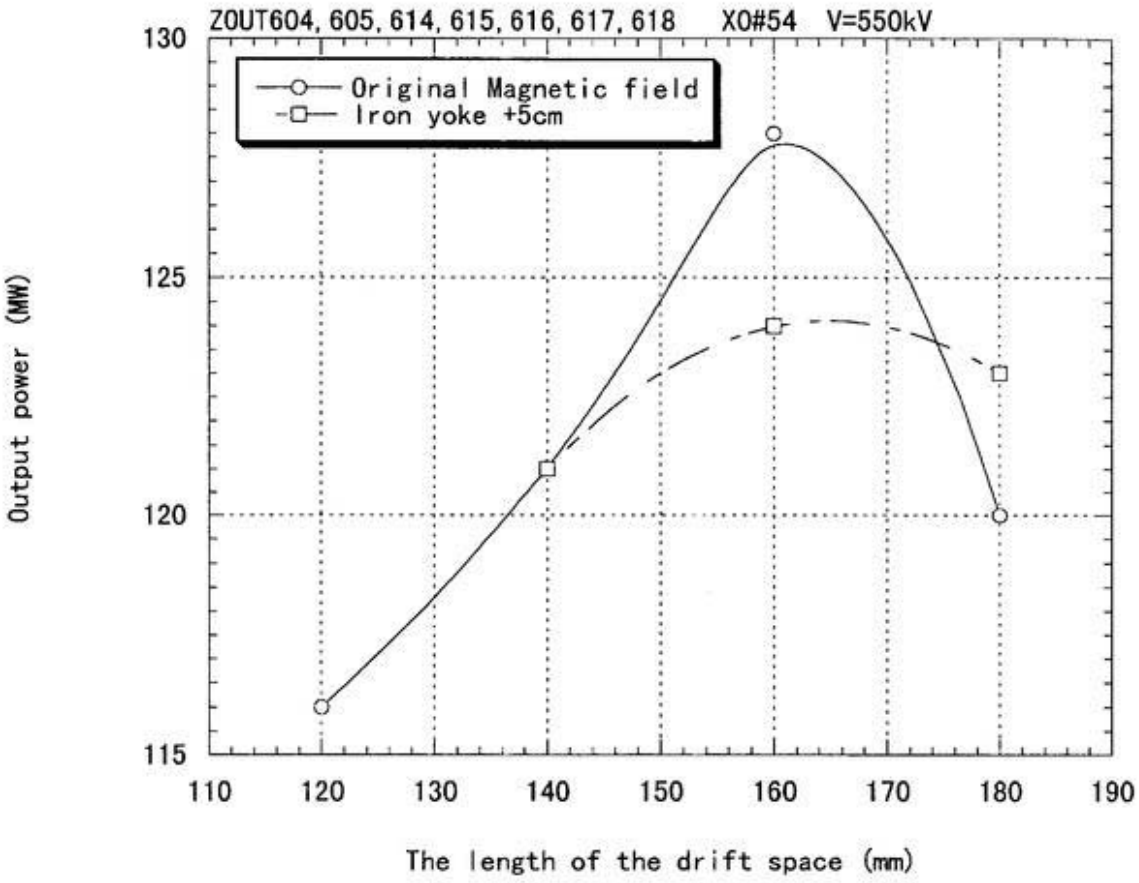

Figure 4.2: Output power vs. distance between the second gain cavity and the first bunching cavity by a MAGIC2D simulation

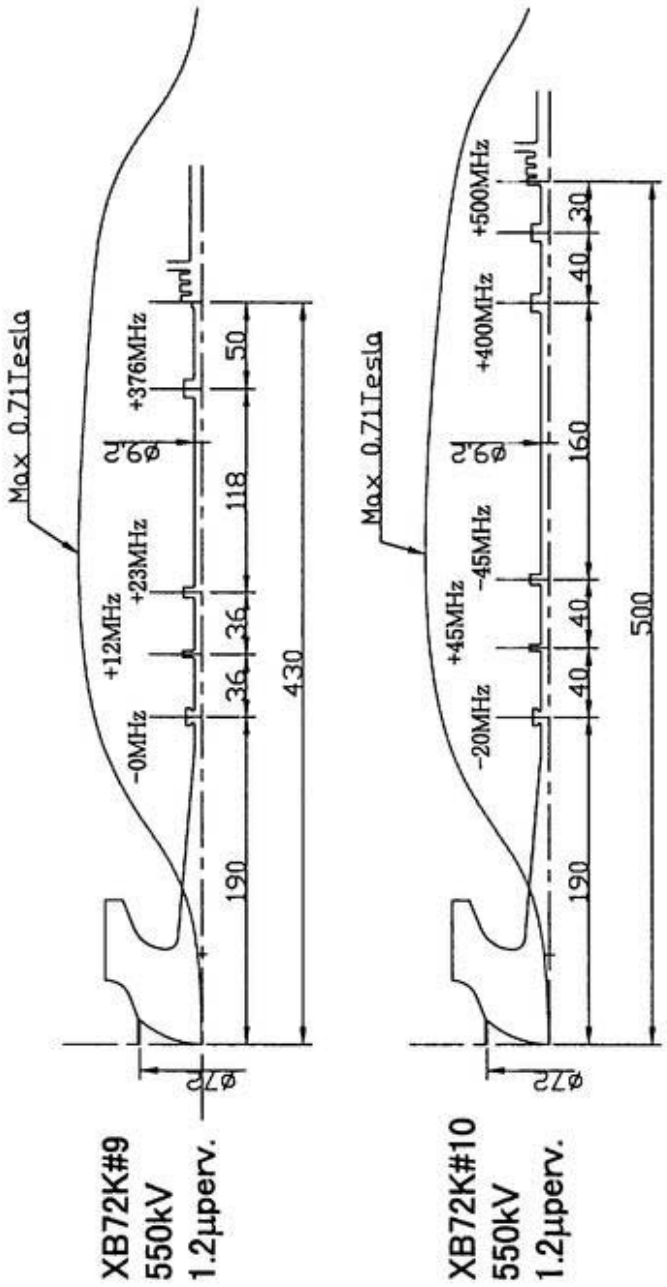

Figure 4.3: Schematic of the No. 9 and No. 10 klystron bunching section.

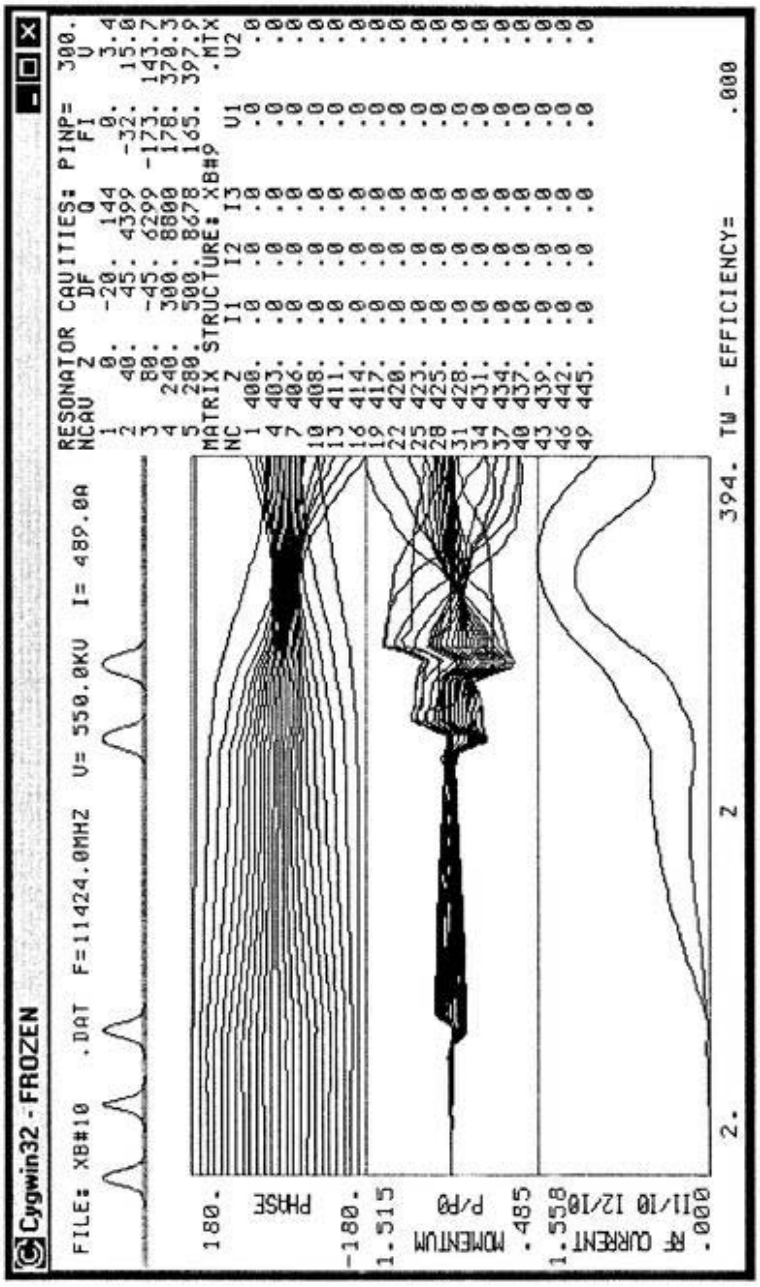

Figure 4.4: DISKLY simulation of the XB72K No. 10 klystron.

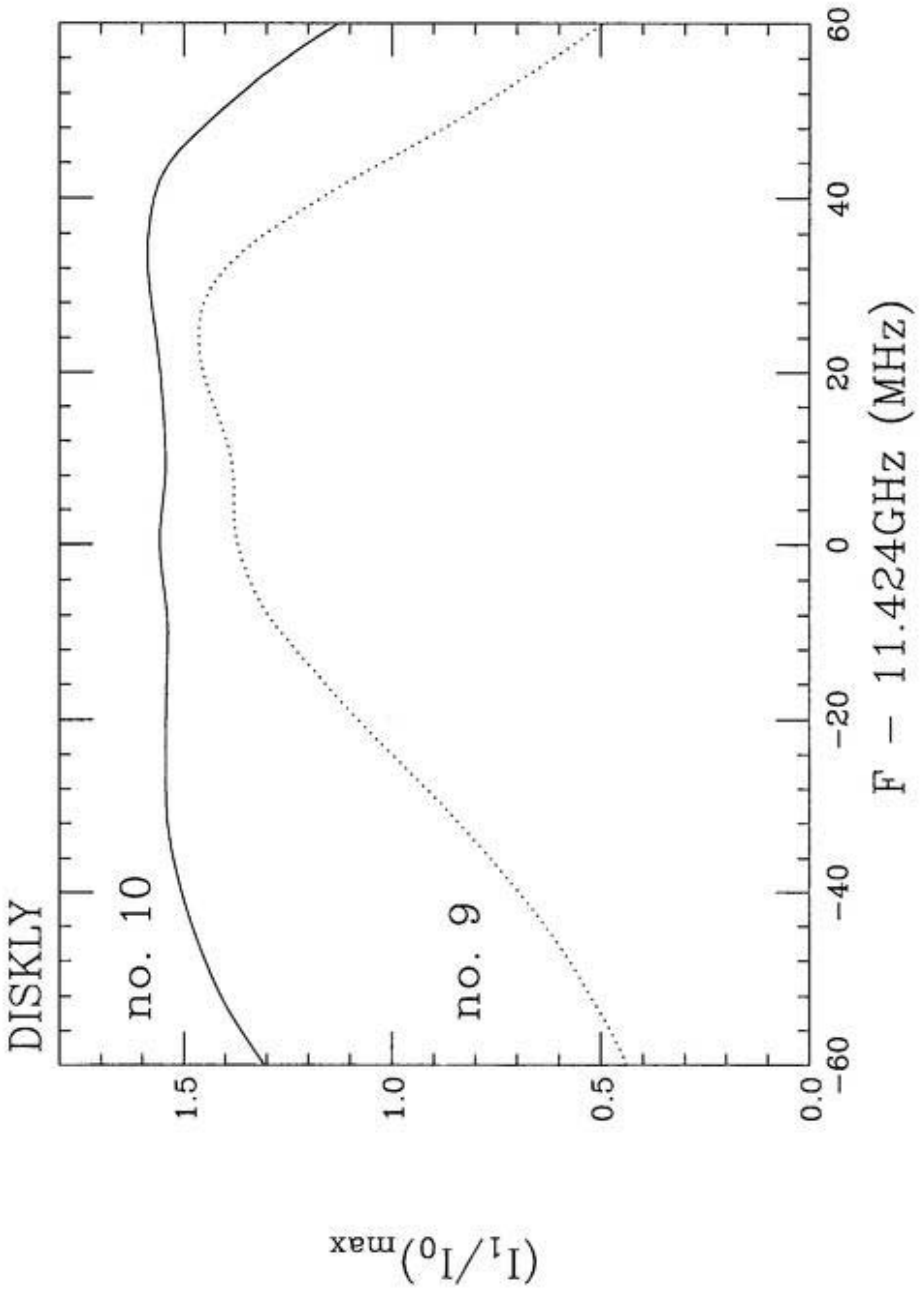

Figure 4.5: Dependence of the maximum normalized current $(I_1/I_0)_{max}$ on the operating frequency. This was calculated by the DISKLY code.

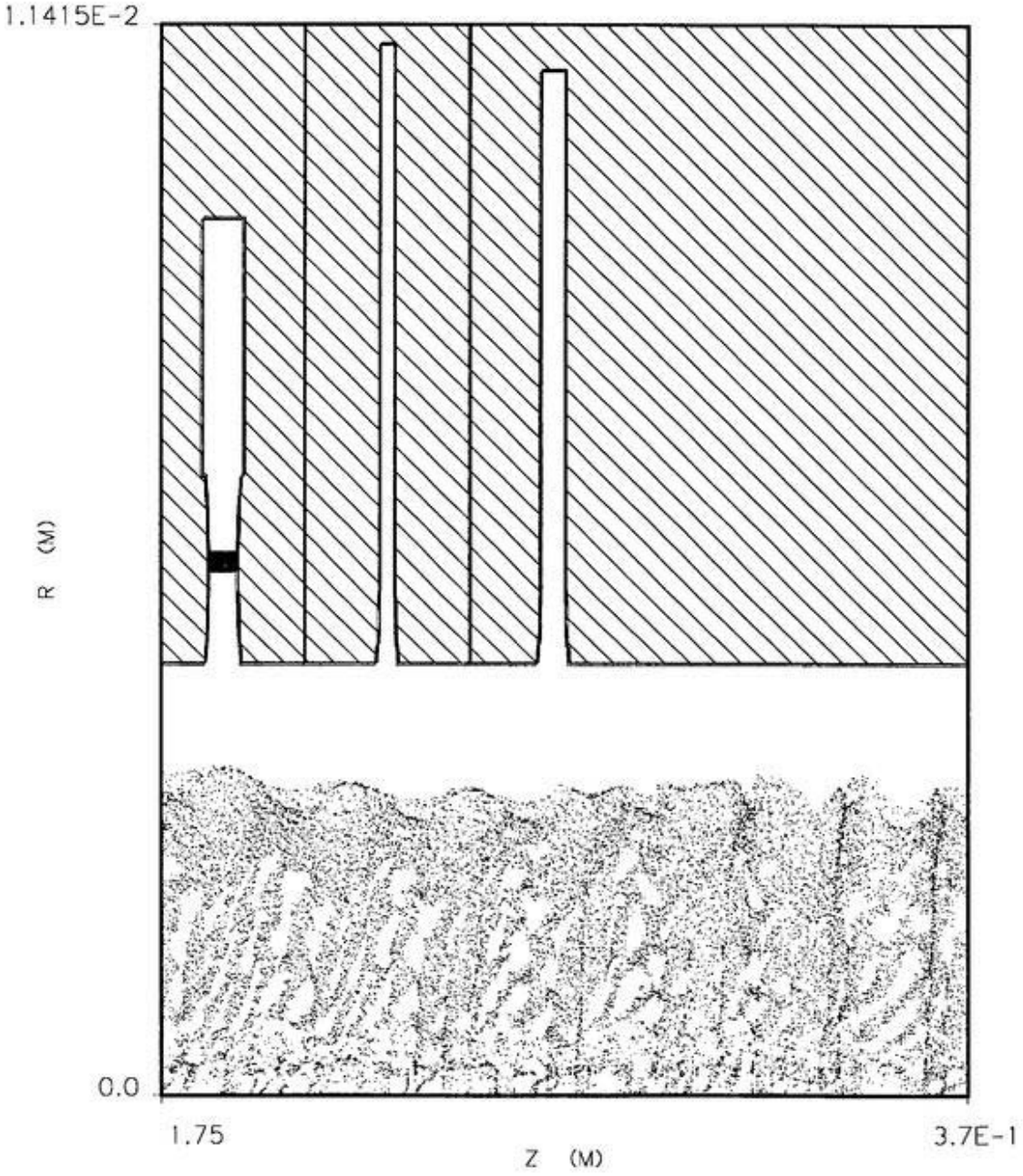

Figure 4.6: Beam profile in the first three cavities of the XB72K No. 10 klystron.

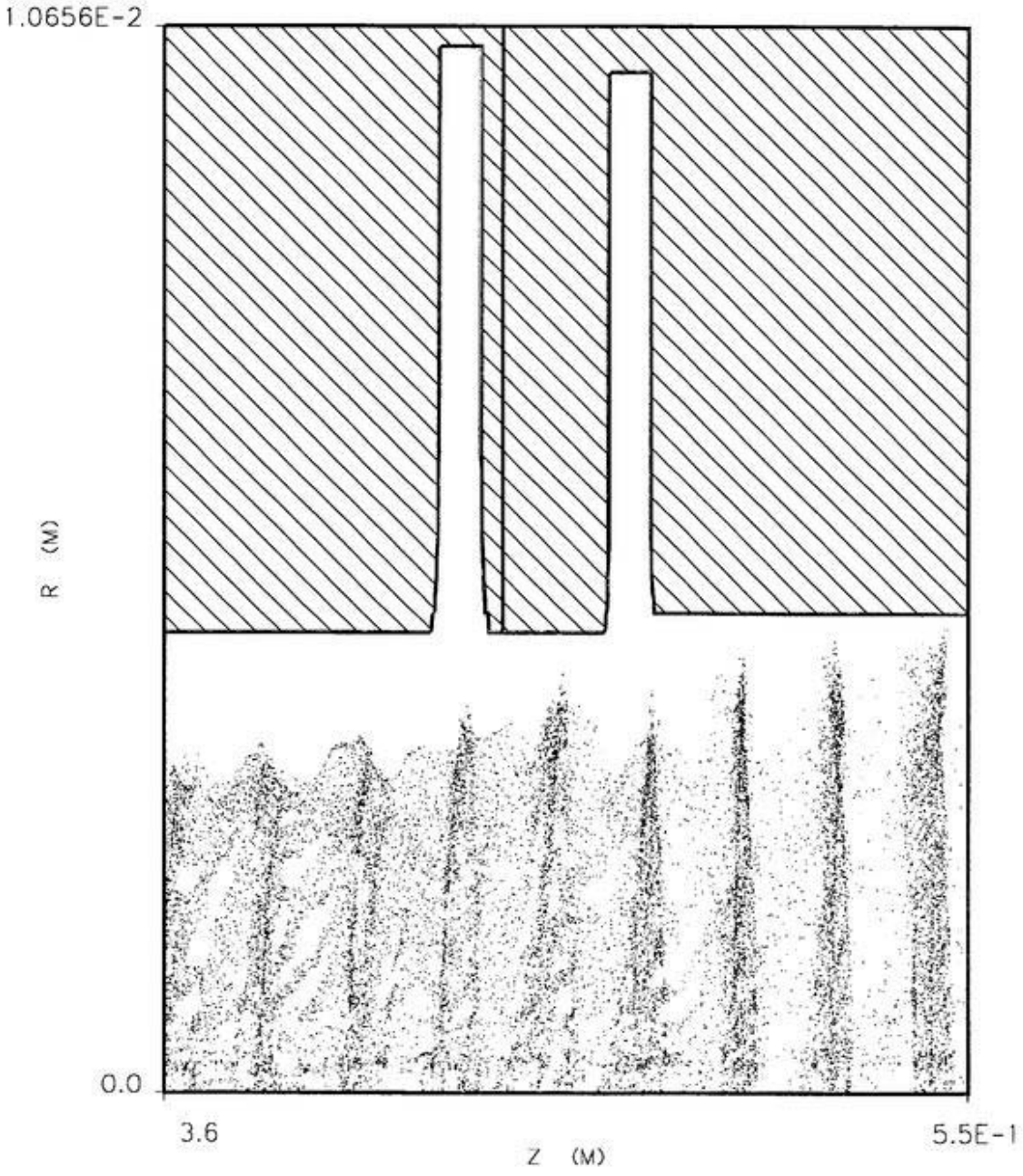

Figure 4.7: Beam profile in bunching cavities of the XB72K No. 10 klystron.

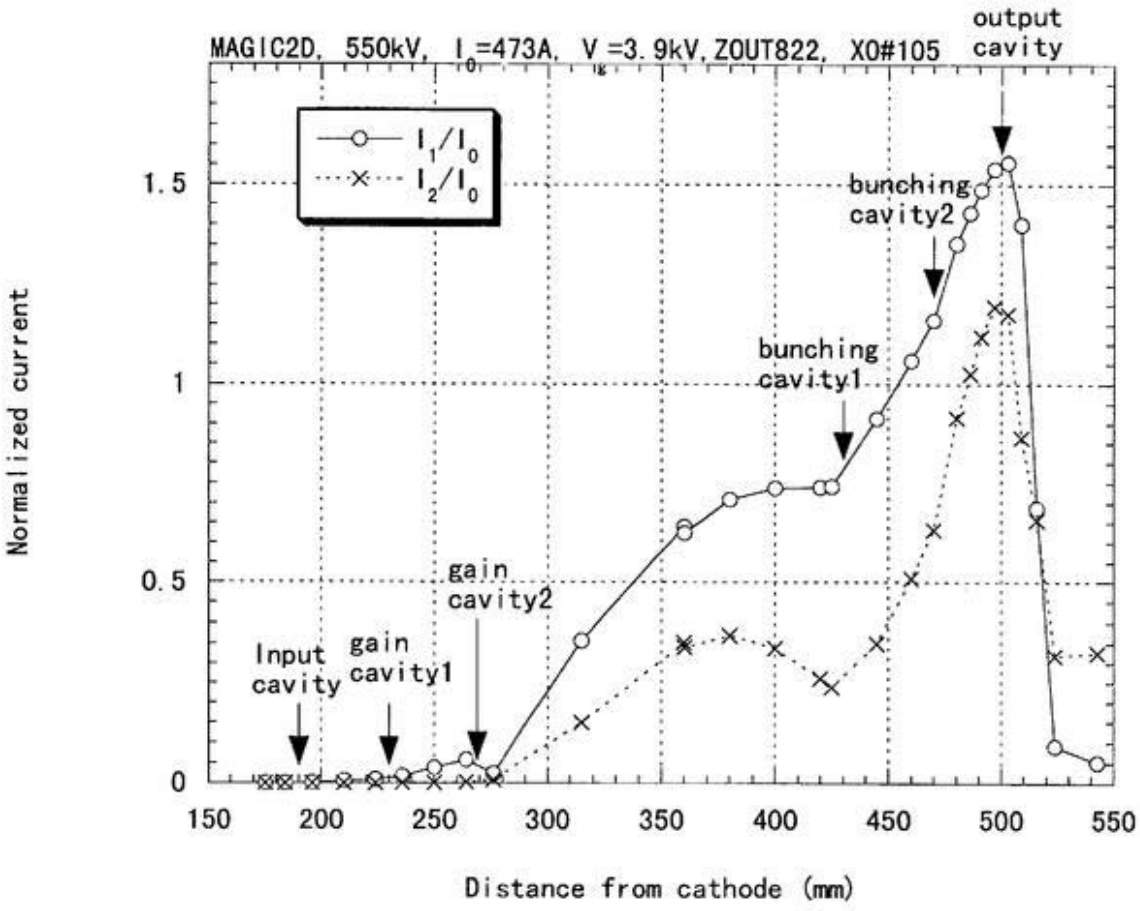

Figure 4.8: Normalized RF current of the XB72K No. 10 klystron

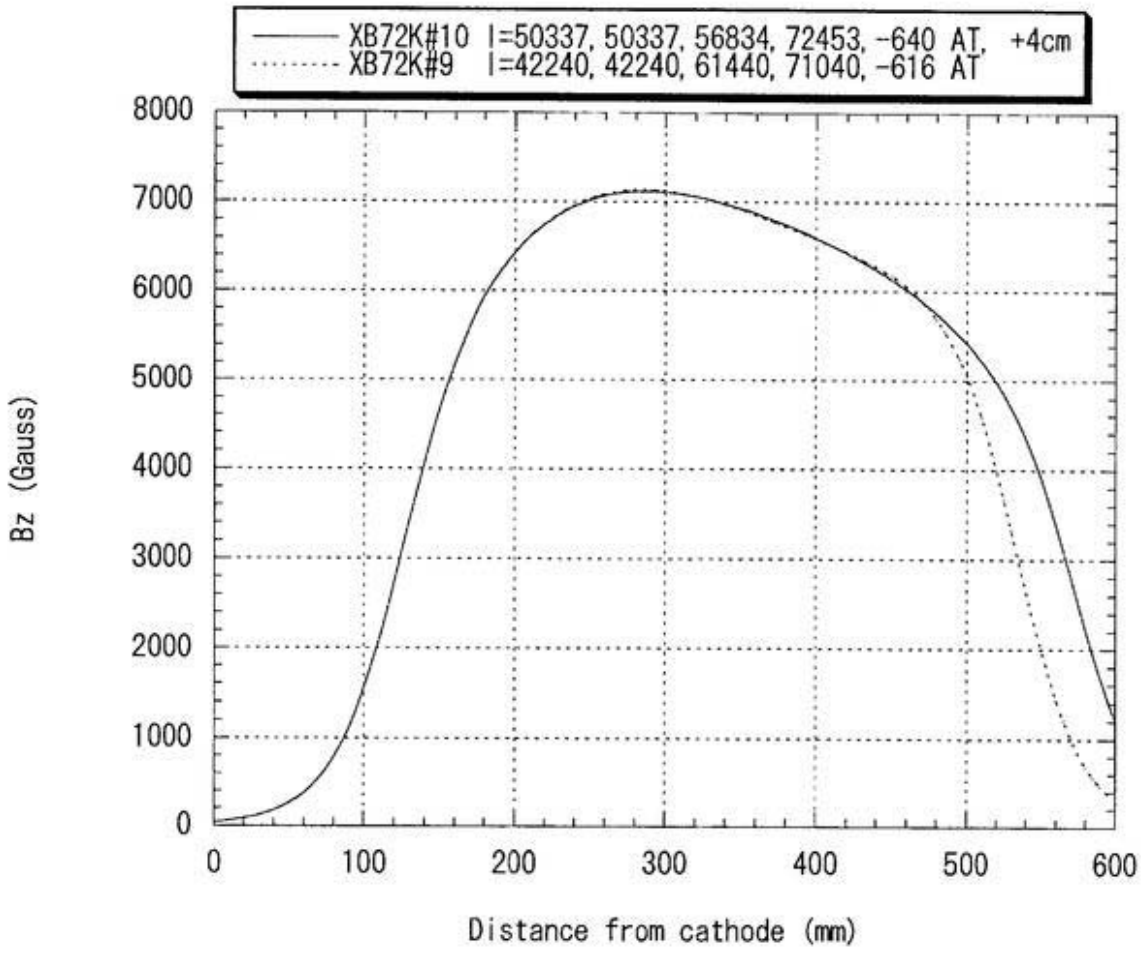

Figure 4.9: Focusing magnetic field of the XB72K No. 10 klystron.

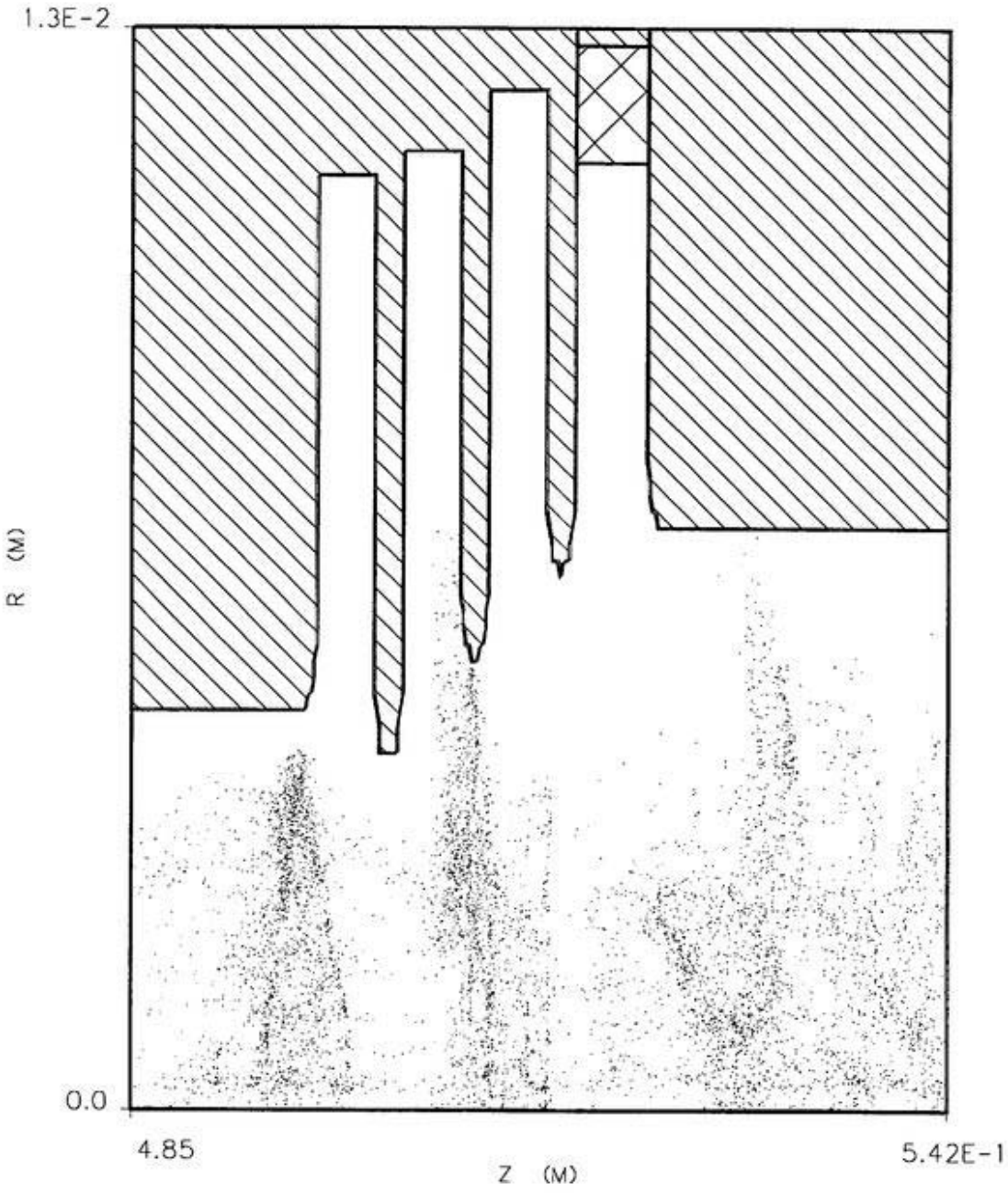

Figure 4.10: Particle trajectory in the XO#0 output structure.

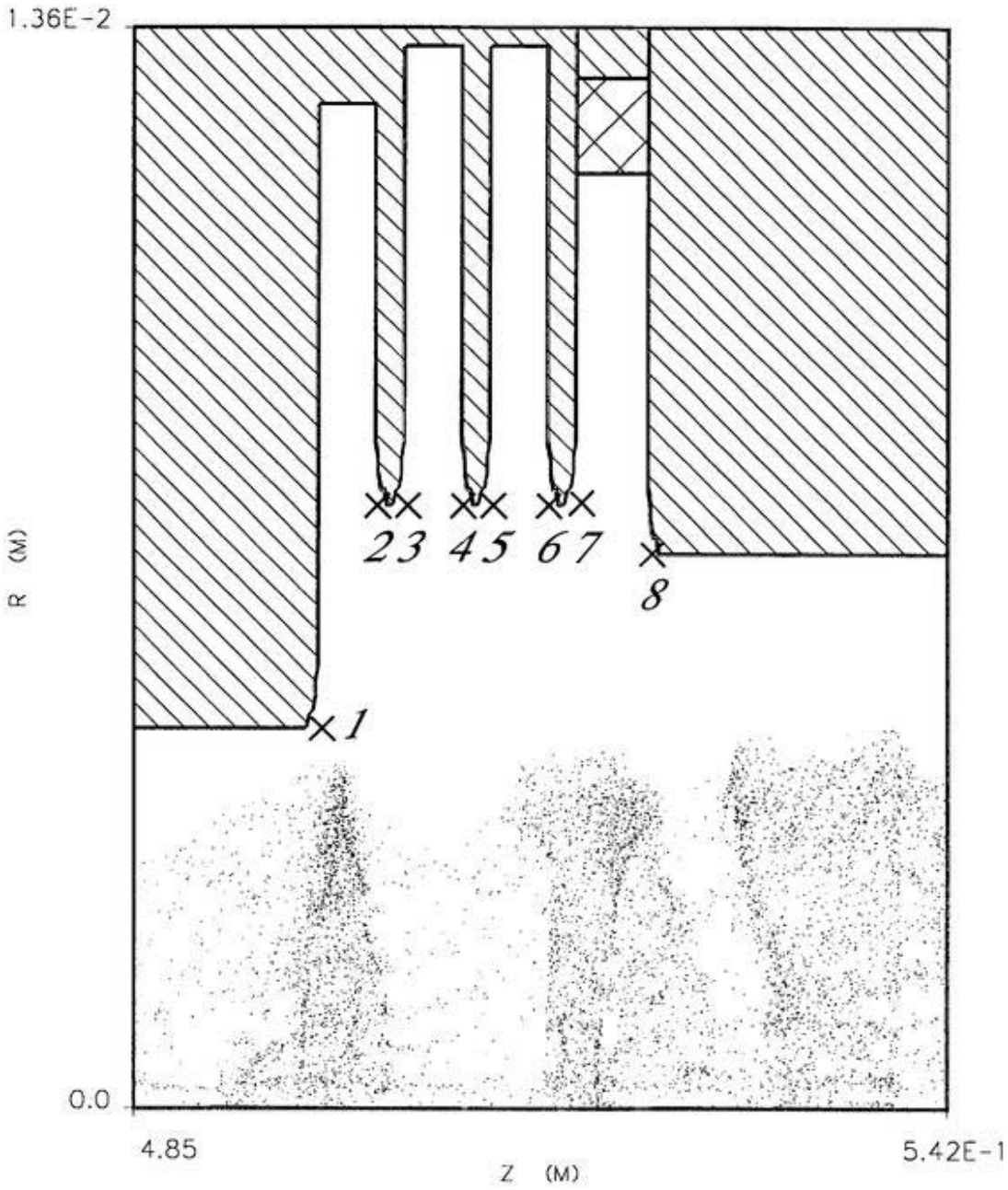

Figure 4.11: Electron beam trajectory in the XO#45 output structure. Electric fields were observed at eight points shown in the figure.

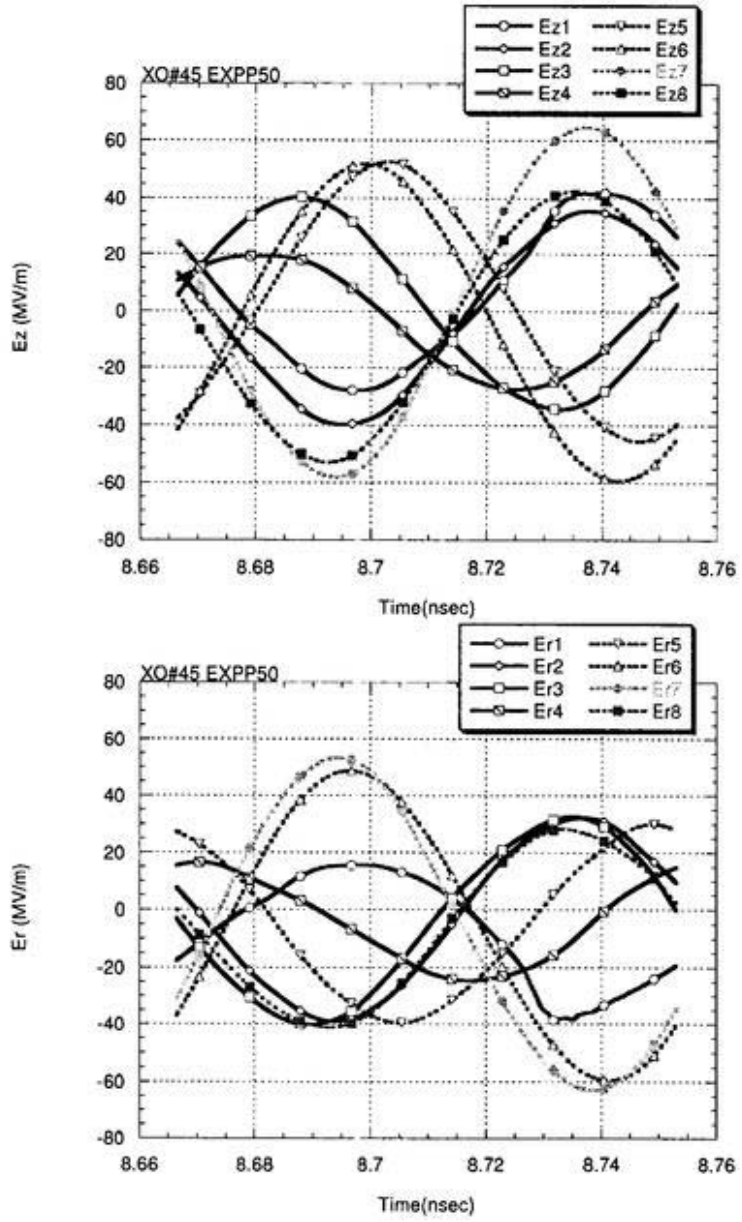

Figure 4.12: Electric field in the XO#45 cavity. The positions of the points are shown in Figure 4.11

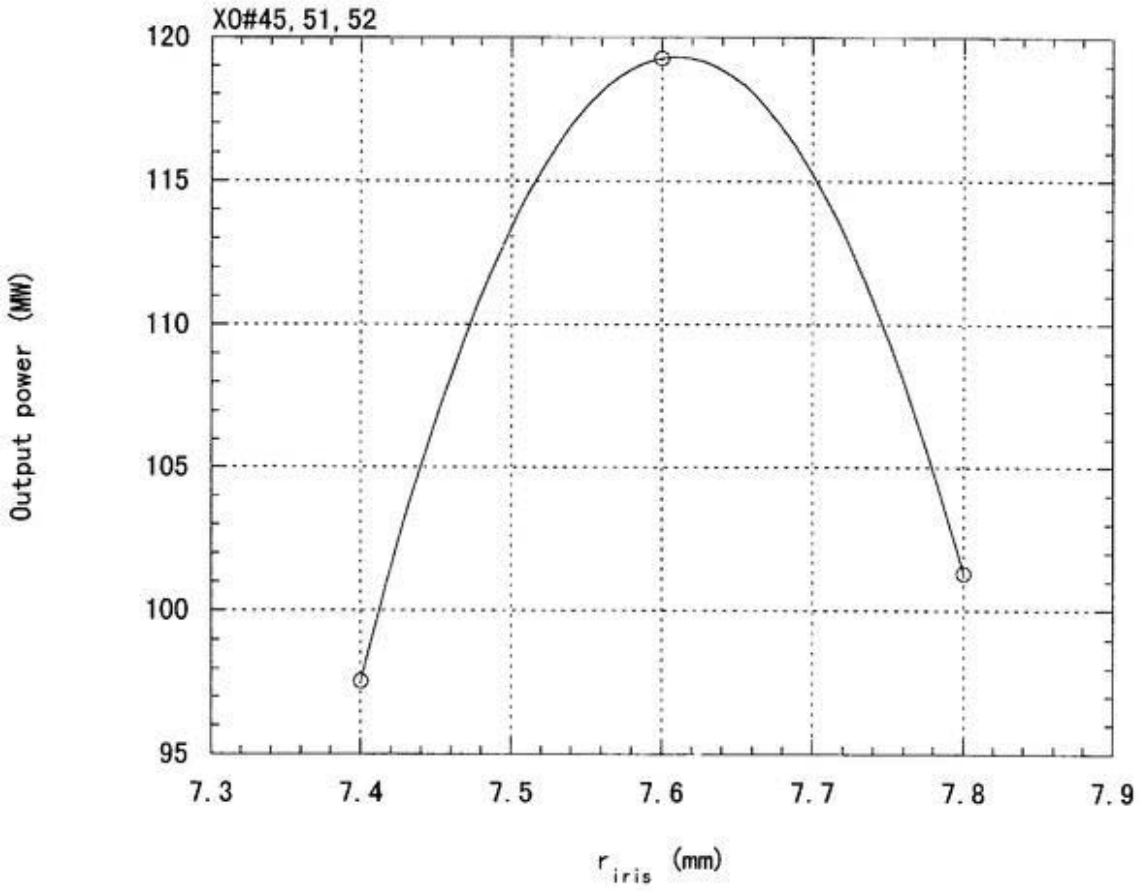

Figure 4.13: Output power vs. radius of the irises for the XO#45 output structure.

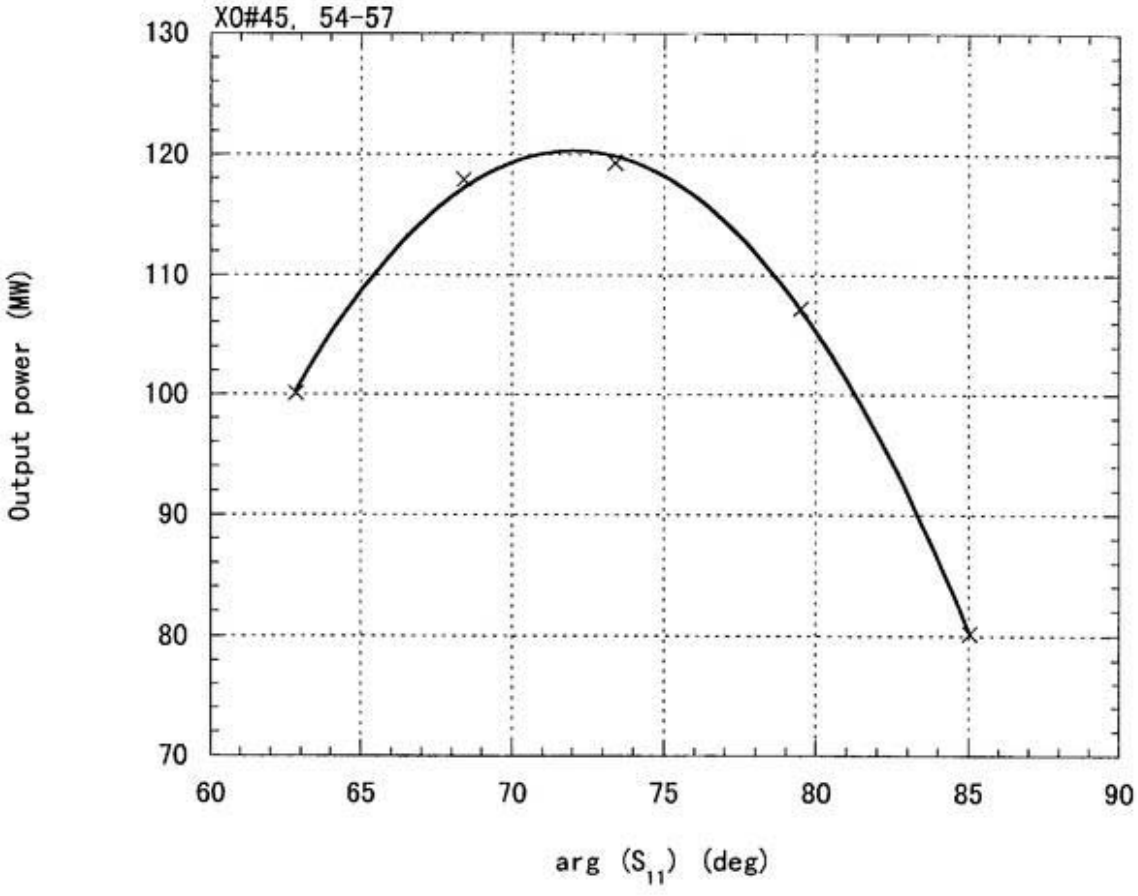

Figure 4.14: Output power vs. argument of the reflection coefficient

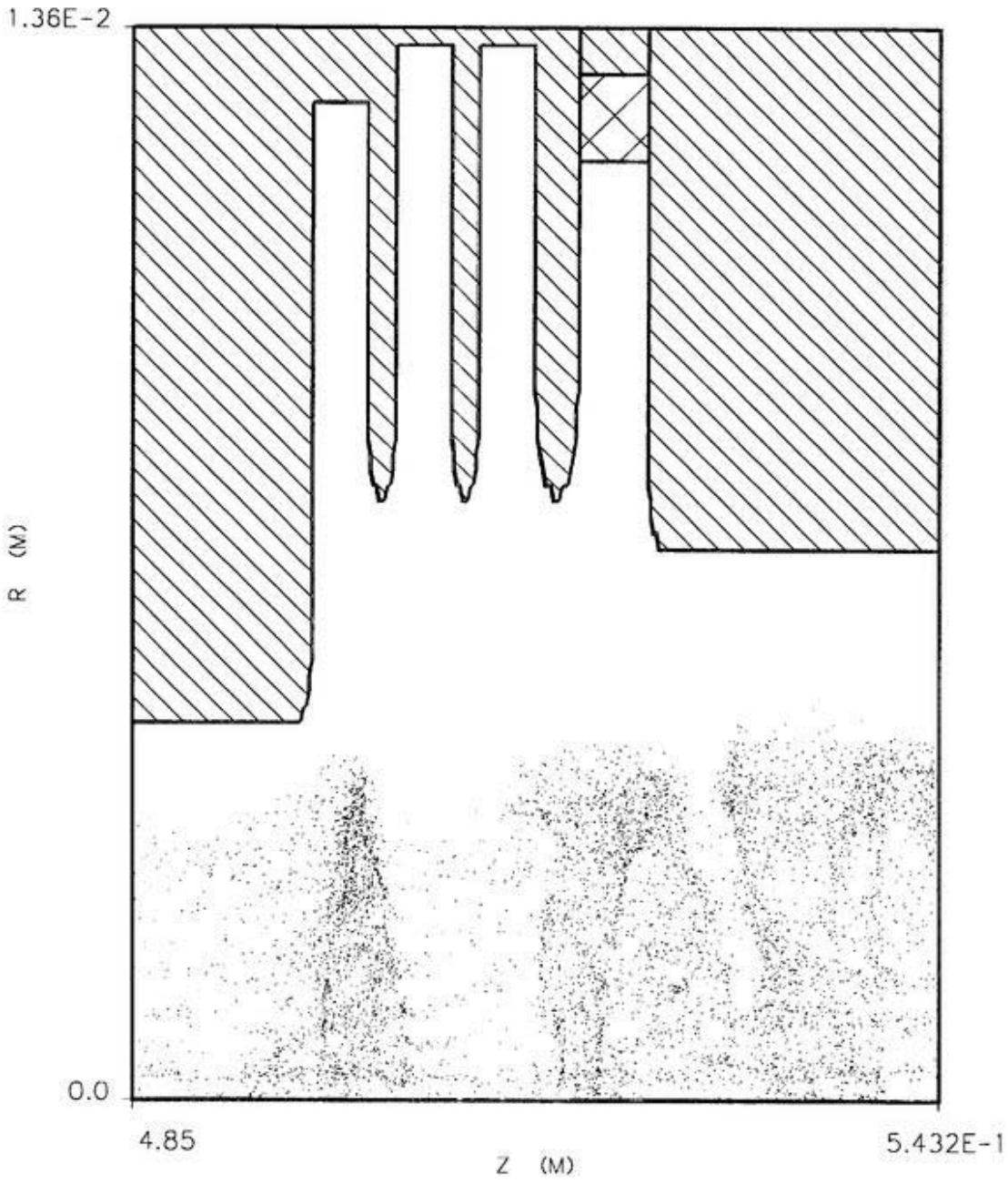

Figure 4.15: Electron-beam trajectory in the XO#87 output structure.

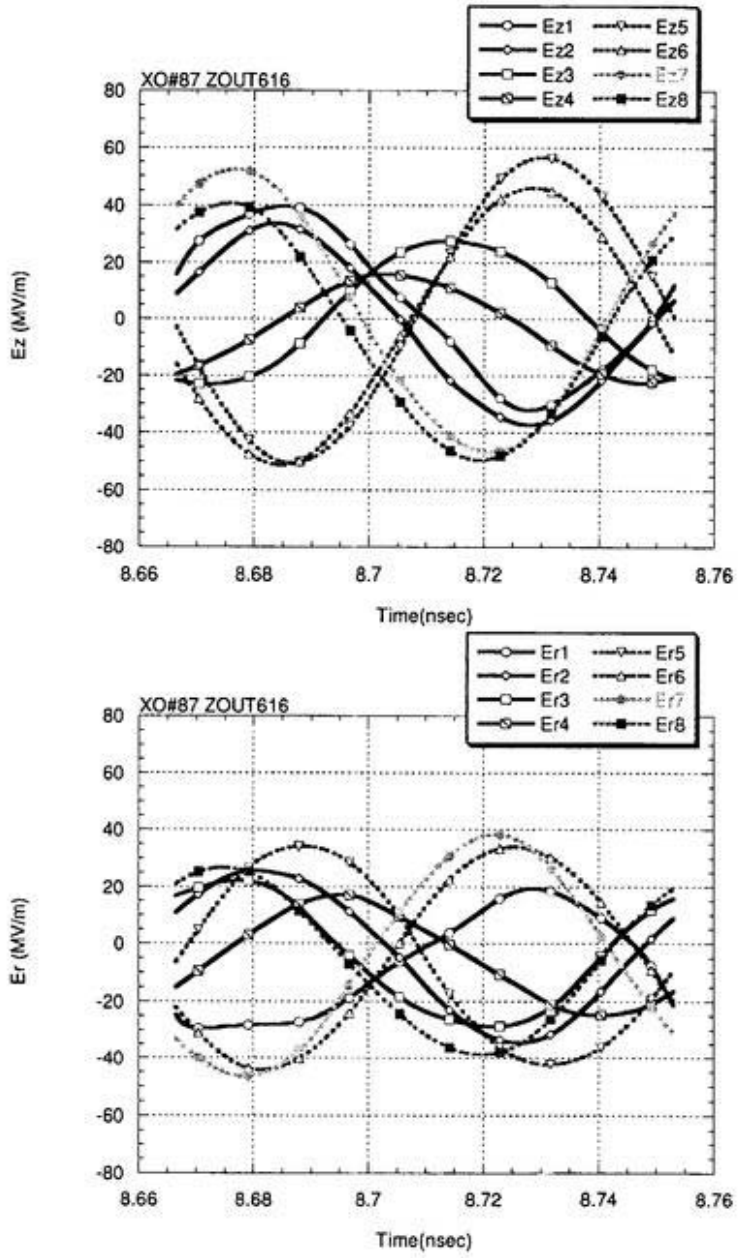

Figure 4.16: Electric-field distribution in the XO#87 output structure.

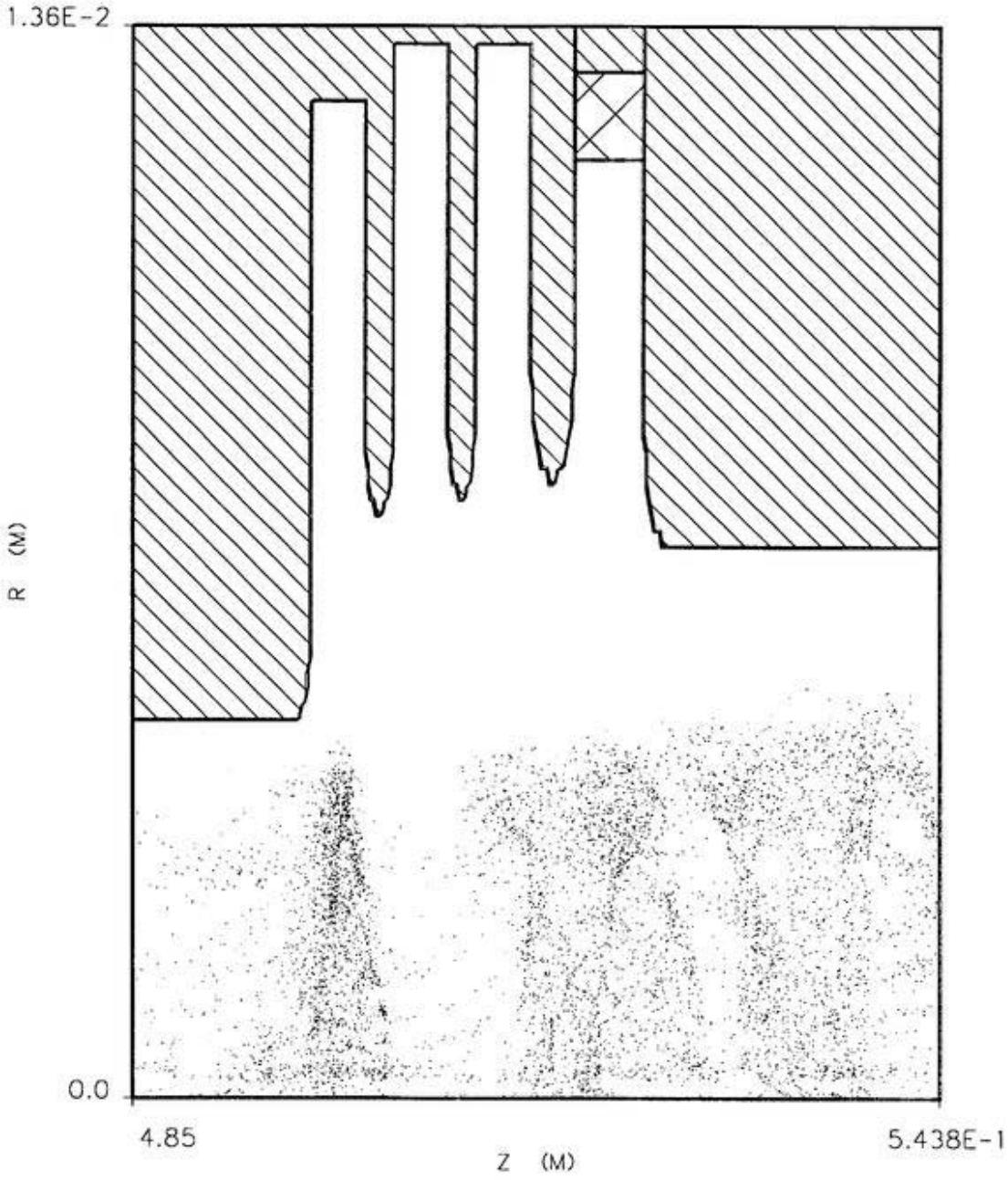

Figure 4.17: Electron-beam trajectory in the XO#105 output structure.

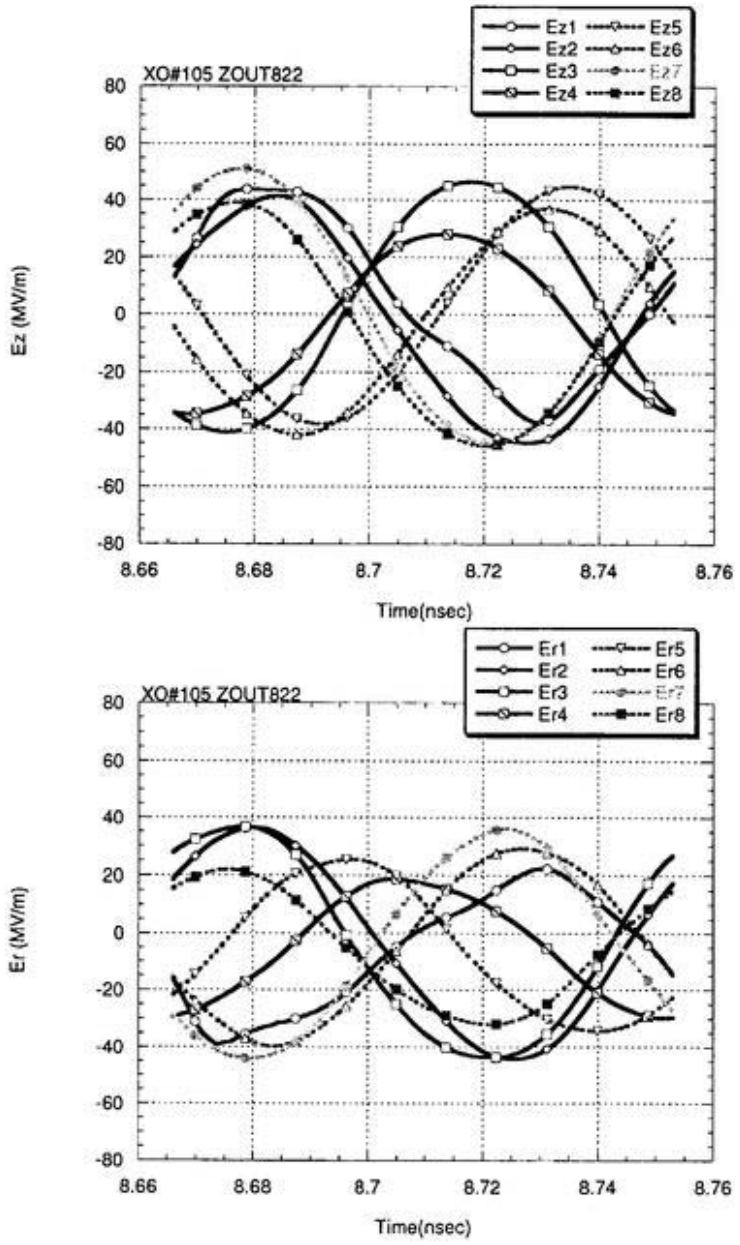

Figure 4.18: Electric-field distribution in the XO#105 output structure.

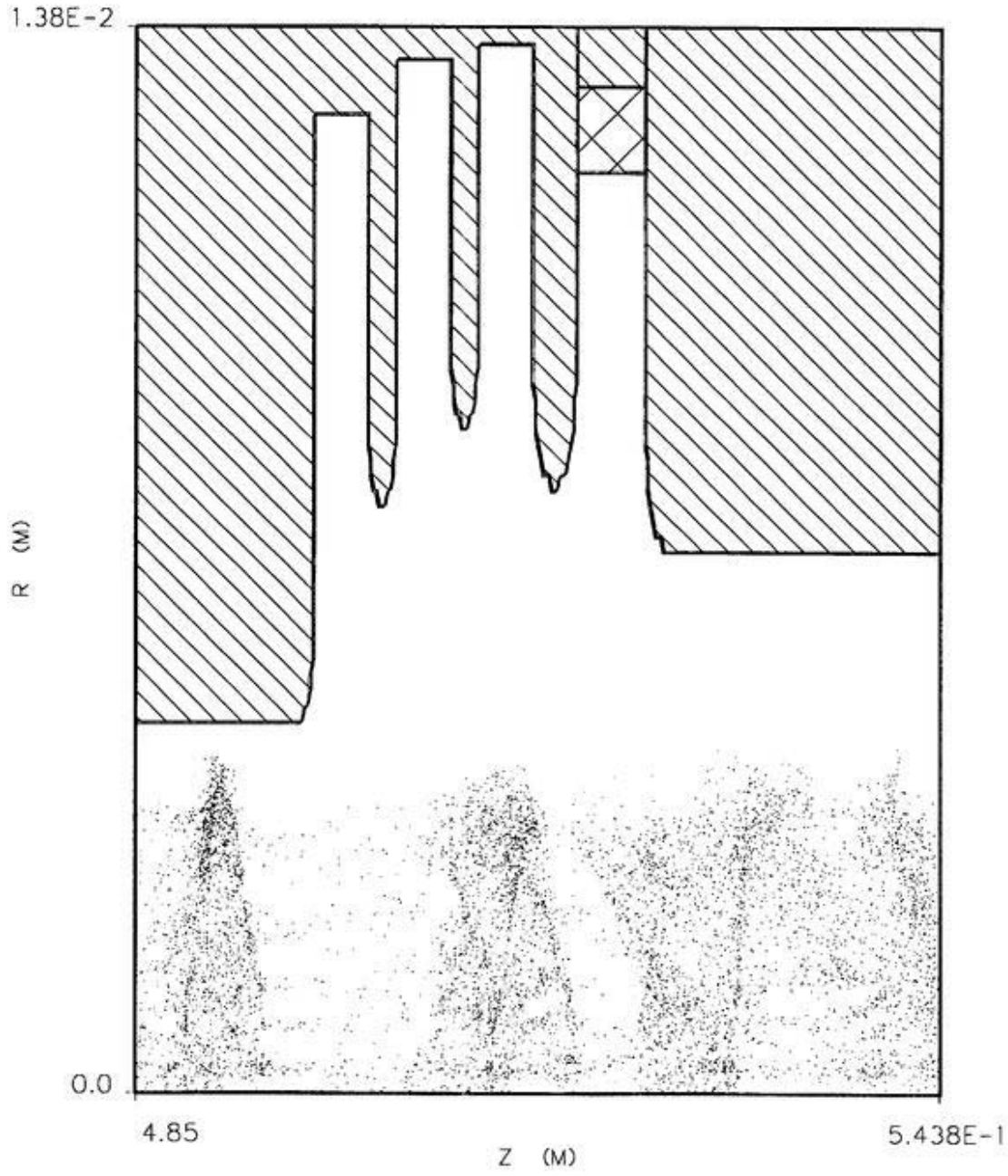

Figure 4.19: Electron-beam trajectory in the XO#105m29 output structure.

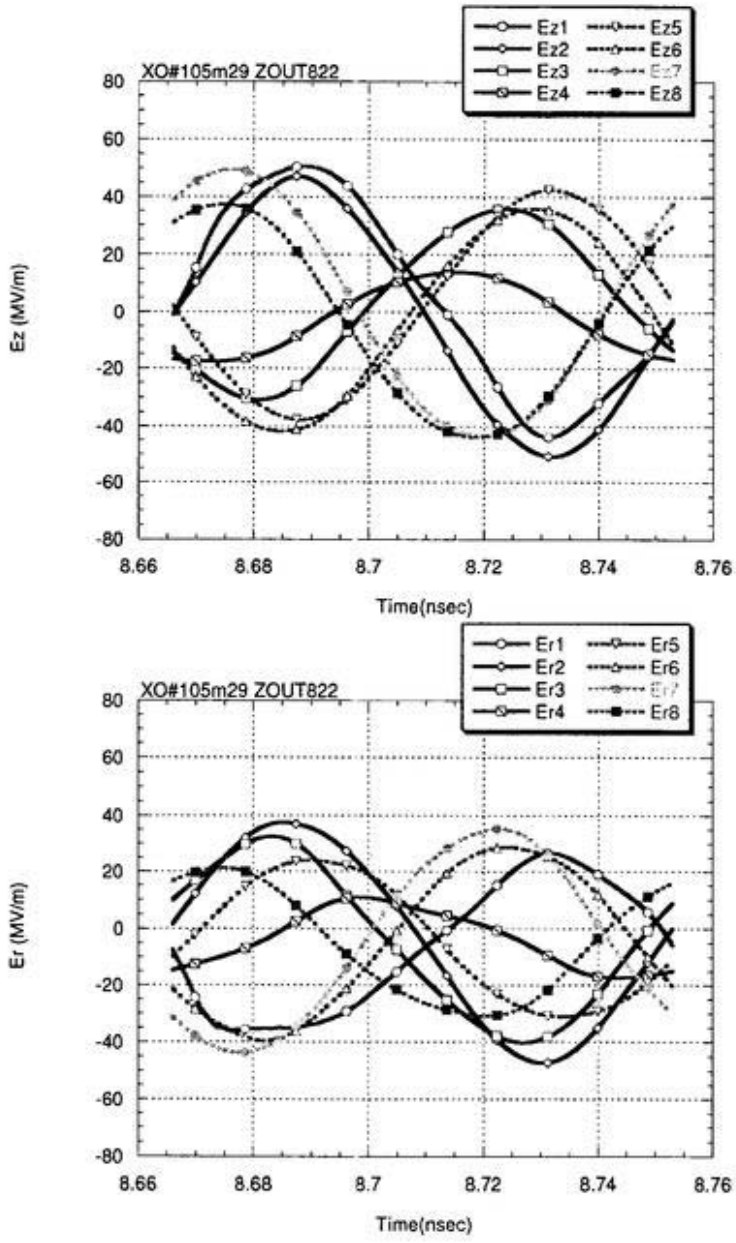

Figure 4.20: Electric-field distribution in the XO#105m29 output structure.

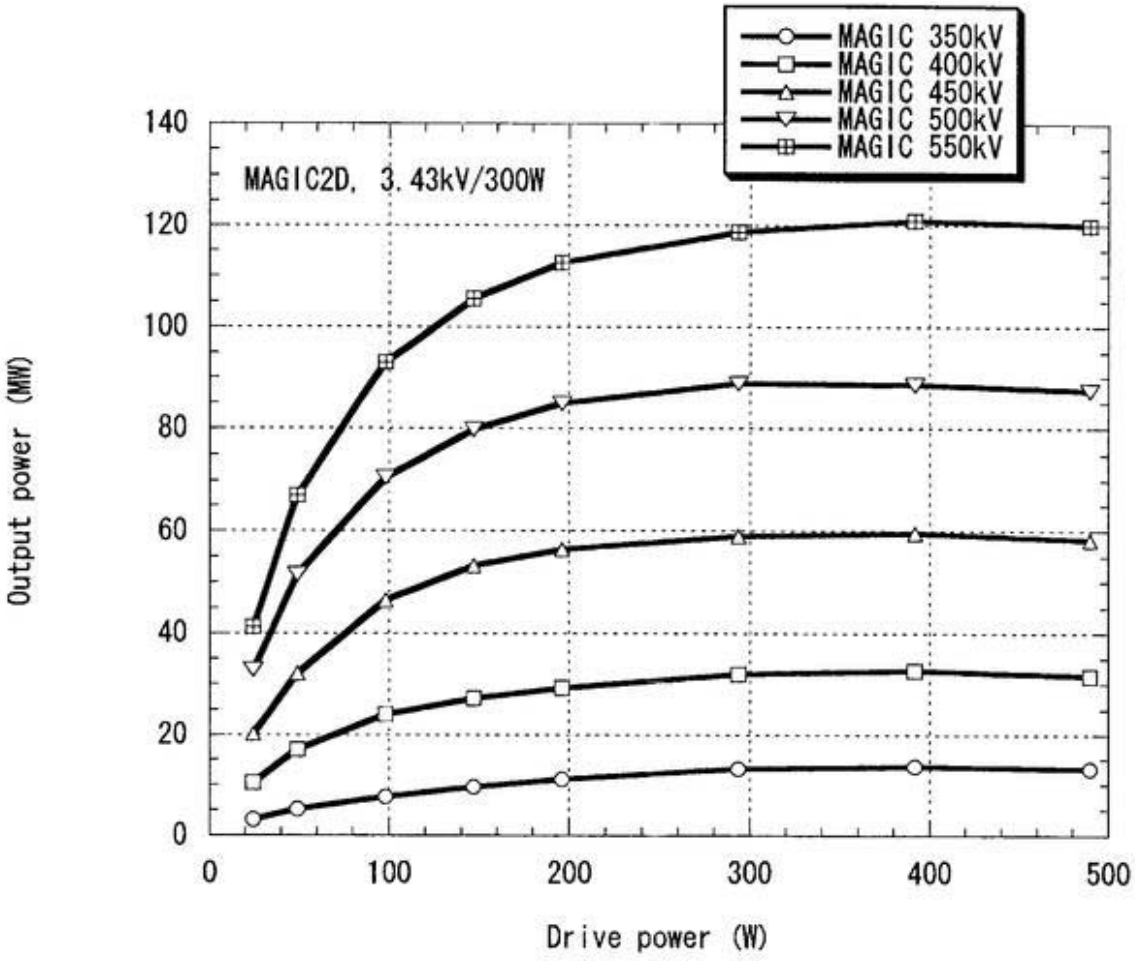

Figure 4.21: Output power vs. drive power of the input cavity.

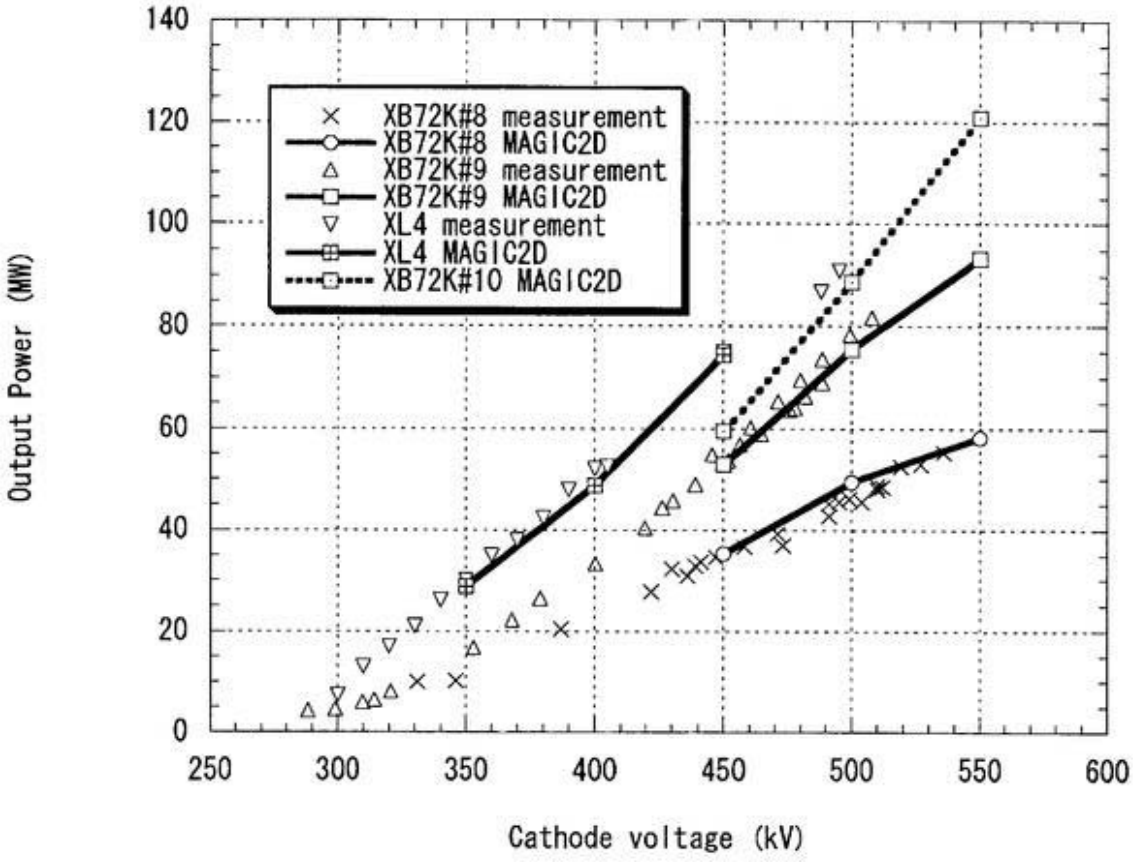

Figure 4.22: Saturated output power vs. cathode voltage.

Chapter 5

Conclusions and Summary

For the stable operation of klystrons, the amplitude of the electric field in the output cavity should be small. In the X-band (11.424GHz) klystron for next linear colliders (JLC/NLC), the use of a multi-cell output structure is one the way to reduce the maximum electric field.

The 'Port approximation method' is a powerful klystron simulation technique used to skip the transient state. This method has been used in most klystron simulation codes. Unfortunately, applying this technique to a multi-cell cavity is not easy, because there are many modes around the operating frequency in the cavity.

S. Kazakov found a method to simulate a multi-cell cavity. A one-dimensional klystron simulation code, DISKLY, treats the multi-cell output structure by his method. This code had been used to design the XB72K No. 7-9 klystrons. It has been found that the measured output powers are far smaller compared to the simulated values. We think that the discrepancy is because the DISKLY code is one-dimensional.

MAGIC2D is a two-dimensional multi-purpose time-domain particle-in-cell simulation code developed by MRC. Since it solves Maxwell's equations directly, it can treat the multi-cell output structure. On the other hand, it takes much time (typically one or two days) to do a full simulation of a klystron. This code was introduced at KEK in 1997.

Since the output coupler does not have axial symmetry, the output cavity cannot be simulated by MAGIC2D directly. Though the output cavity can be simulated by three-dimensional codes, such as MAGIC3D, without any assumptions, these codes need so much computer resources that it is presently very difficult to design a new klystron with them. It may take about one

month or so to make a full klystron simulation with a coarse (0.5mm) mesh.

In order to conduct two-dimensional simulations of the multi-cell output structures, we have developed a two-dimensional model of the output coupler. A scattering matrix was defined as the relation between the traveling waves of the cavity cell mode (we call this the TM0*0 mode) and the traveling waves of the TE10 mode of a rectangular waveguide. Since a traveling wave can be decomposed into two standing waves with different phases, the scattering matrix can be calculated by using standing waves. A frequency-domain code was used to create the standing waves, and the phases of the standing waves were shifted by changing the boundary condition of the waveguides. We searched three independent pairs of the phases of the standing waves of the TM0*0 mode and the TE10 mode for a given frequency. From three pairs of phases, we calculated the scattering matrix for given frequency. The reflection coefficient of the TM0*0 waves was calculated from the scattering matrix and the reflection coefficient of the TE10 waves. In the MAGIC2D simulation, a finite conducting material was set at the coupler region, the parameters of which were adjusted so as to satisfy the reflection coefficient of the TM0*0 mode.

Our new method was empirically justified based on comparison of the saturated output power between the measurement and the simulation. The saturated output power agrees within 10% between them, which is much better than the one-dimensional simulation code DISKLY.

Using the above techniques, we designed the XB72K No. 10 klystron. We changed the bunching section and the output structure from the No. 9 klystron.

For the bunching section, one bunching cavity was added to increase the RF current at the output structure. Furthermore, the resonant frequencies of the gain cavities were changed so as to obtain a wide-band response (stagger tuning).

For the output structure, we tried to reduce the electric field by using the $2\pi/3$ mode. At first, the parameters of the structure were chosen by using simple equations. Then, we used the 'cut and try' method to improve the performance of the output structure. By the MAGIC2D simulation, the saturated output power of the No. 10 klystron was found to be 120MW at 550kV. This klystron will be tested in January, 1999.

Acknowledgments

I would like to acknowledge the assistance, support, and efforts of Dr. Shinichiro Michizono and Dr. Shuji Matsumoto.

I wish to thank Mr. Shuichi Tokumoto, for measurements of the XB72K klystrons.

I wish to thank Professor Nobukazu Toge and Professor Toshiyasu Higo, for their helpful suggestions and comments at a meeting.

I wish to thank Mr. Tomonori Sakamoto and Mr. Masato Kanno of TOSHIBA Corporation, for manufacturing the XB72K No. 10 klystrons, and for useful discussions and suggestions.

I wish to thank the klystron group of SLAC, especially Dr. Arnold E. Vlieks, for showing me the data and a drawing of the XL-4 klystron.

I would like to thank Ms. Noriko Onishi and Dr. Katsuhiro Shinto for the correction of my bad English.

I would also like to thank Mr. Takeshi Takayama, Mr. Toshitada Hori, Mr. Masaoki Hirose, and colleagues of Sumitomo Heavy Industries, Ltd. They sent me to this graduate university.

Appendix A

Derivation of ξ_1

The configuration is shown in Figure 2.3. In a dielectric material, the electric field is

$$\begin{aligned} E_{z1} &= J_0(k'r), \\ k' &= \sqrt{\epsilon_r}\omega/c. \end{aligned} \tag{A.1}$$

In the region between the material and the coupler, the electric field is

$$\begin{aligned} E_{z2} &= \alpha\left(H_0^{(1)}(kr) + \xi_1 H_0^{(2)}(kr)\right), \\ k &= \omega/c. \end{aligned} \tag{A.2}$$

At the boundary ($r = b$), the longitudinal component of electric field and the azimuthal component of the magnetic field should be continuous:

$$\begin{aligned} E_{z1}(r=b) &= E_{z2}(r=b), \\ \frac{\partial E_{z1}}{\partial r}(r=b) &= \frac{\partial E_{z2}}{\partial r}(r=b). \end{aligned} \tag{A.3}$$

By solving the above equation with ξ_1, we obtain

$$\xi_1 = \frac{kJ_0(k'b)H_1^{(1)}(kb) - k'J_1(k'b)H_0^{(1)}(kb)}{k'J_1(k'b)H_0^{(2)}(kb) - kJ_0(k'b)H_1^{(2)}(kb)}. \tag{A.4}$$

Appendix B

Energy Conservation and Scattering Matrix

From the energy-conservation law, one can obtain

$$\exists A \in \mathcal{R}, \forall a_{1in}, a_{2in} \in \mathcal{C},$$
$$|a_{1in}|^2 + A|a_{2in}|^2 = |S_{11}a_{1in} + S_{12}a_{2in}|^2 + A|S_{21}a_{1in} + S_{22}a_{2in}|^2. \quad \text{(B.1)}$$

By eliminating a_{1in}, a_{2in}, one obtains,

$$\begin{aligned} 1 &= |S_{11}|^2 + A|S_{21}|^2, \\ A &= |S_{12}|^2 + A|S_{22}|^2, \\ 0 &= S_{11}S_{12}^* + AS_{21}S_{22}^*. \end{aligned} \quad \text{(B.2)}$$

If we define α_{ij}, ϕ_{ij} as

$$S_{ij} = \alpha_{ij}\exp(\phi_{ij}), \alpha_{ij} > 0, \quad \text{(B.3)}$$

Eq. (B.2) becomes,

$$\begin{aligned} \alpha_{11} &= \alpha_{22}, \\ \alpha_{11}^2 + \alpha_{12}\alpha_{21} &= 1, \\ \phi_{11} + \phi_{22} &= \phi_{12} + \phi_{21} + (2n+1)\pi. \end{aligned} \quad \text{(B.4)}$$

These equations can be written in another form:

$$\begin{aligned} |S_{11}| &= |S_{22}|, \\ |S_{11}|^2 + |S_{12}S_{21}| &= 1, \\ S_{11}S_{22} - S_{12}S_{21} &= S_{11}/S_{22}^*. \end{aligned} \quad \text{(B.5)}$$

Appendix C

Derivation of Equation (2.13)

In the vacuum region ($r < h$), electric field is

$$\begin{aligned} E_{z1} &= H_0^{(1)}(kr) + sH_0^{(2)}(kr), \\ k &= \omega/c. \end{aligned} \tag{C.1}$$

In the material ($h < r < g$), electric field is

$$\begin{aligned} E_{z2} &= \xi H_0^{(1)}(k''r) + \eta H_0^{(2)}(k''r), \\ k'' &= \sqrt{(\omega/c)^2 + i\mu_0\sigma\omega}. \end{aligned} \tag{C.2}$$

Boundary conditions are:

$$\begin{aligned} E_{z1}(r=h) &= E_{z2}(r=h), \\ \frac{\partial E_{z1}}{\partial r}(r=h) &= \frac{\partial E_{z2}}{\partial r}(r=h), \\ E_{z2}(r=g) &= 0. \end{aligned} \tag{C.3}$$

Solving the above equations, one obtains,

$$\begin{aligned} s &= \frac{k\alpha H_1^{(1)}(kh) - k''\beta H_0^{(1)}(kh)}{k''\beta H_0^{(2)}(kh) - k\alpha H_1^{(2)}(kh)}, \\ \alpha &= H_0^{(1)}(k''g)H_0^{(2)}(k''h) - H_0^{(2)}(k''g)H_0^{(1)}(k''h), \\ \beta &= H_0^{(1)}(k''g)H_1^{(2)}(k''h) - H_0^{(2)}(k''g)H_1^{(1)}(k''h). \end{aligned} \tag{C.4}$$

Appendix D

Relation between the Input Power and the Gap Voltage

According to Eq. (5.4) of the reference [14], the cavity impedance(Z) seen from outside is

$$\frac{Z}{Z_0} \simeq \frac{1/Q_{ext}}{-i(\omega/\omega_r - \omega_r/\omega) + 1/Q_0 + \frac{1}{2\omega_r U}\int dV \vec{J}\cdot\vec{E}^*}, \tag{D.1}$$

where, Z_0 is the characteristic impedance in the waveguide, Q_{ext} is the external quality factor of the cavity, ω_r is the resonant frequency of the cavity, Q_0 is the unloaded quality factor of the cavity, U is the stored electromagnetic field energy in the cavity, $\vec{J}$ is the current density (peak value), and $\vec{E}$ is the electric field (peak value). The variable $\tilde{P}_b$ is defined as

$$\tilde{P}_b = \frac{1}{2}\int dV \vec{J}\cdot\vec{E}^*. \tag{D.2}$$

Assume that the radial component and azimuthal component of the velocity (v_r, v_ϕ) are much smaller than longitudinal component (v_z). Then, the current density($\vec{J}$) is

$$J_z(r,z,t) = \sum_{i=1}^{N} \frac{e}{2\pi r} v_i(z)\delta(r-r_i)\delta(z-z_i(t)), \tag{D.3}$$

where v_i is the z component of the i-th electron velocity, N is the number of electrons in one period. By making a fourier transform of the above equation,

J_z becomes

$$\begin{aligned} J_z(r,z,\omega) &= \frac{2}{T_0}\int_0^{T_0} dt \exp(i\omega t) J_z(r,z,t) \\ &= \frac{2e}{T_0}\sum_{i=1}^{N} \exp(i\omega t_i(z))\delta(r-r_i)/(2\pi r) \\ &= 2I_0 \left\langle \exp(i\omega t_i(z))\delta(r-r_i)/(2\pi r)\right\rangle_i , \end{aligned} \tag{D.4}$$

where $I_0 = eN/T_0$ is the beam current. Then, $\tilde{P}_b$ is

$$\tilde{P}_b = I_0 \int_{-\infty}^{\infty} dz \left\langle E_z^*(r_i,z)\exp(i\omega t_i(z))\right\rangle_i . \tag{D.5}$$

The motion of the electrons in the electric field ($Re(E_z\exp(-i\omega t))$) is

$$\begin{aligned} t_i(z) &= t_i(0) + \int_0^z dz'/v_i(z'), \\ mc^2\frac{d\gamma_i}{dz} &= eE_z = eRe\left(E_z(r_i,z)\exp(-i\omega t_i(z))\right) \\ v_i^2(z)/c^2 &= 1 - 1/\gamma_i^2(z), \end{aligned} \tag{D.6}$$

where γ is the relativistic factor. Using the above equations, the velocity of the i-th particle is

$$\begin{aligned} \frac{dv_i}{dz} &\simeq \frac{c^2}{v_i\gamma_i^3}\frac{d\gamma}{dz} = \frac{e}{mv_i\gamma_i^3} Re\left(E_z(r_i,z)\exp(-i\omega t_i(z))\right), \\ \rightarrow v_i(z) &\simeq v_i(0) + \frac{e}{m}\int_0^z \frac{dz'}{v_i(z')\gamma_i^3(z')} Re\left(E_z(r_i,z')\exp(-i\omega t_i(z'))\right) \end{aligned} \tag{D.7}$$

If the modulation by E_z is small, a 0-th order approximation for (v_i, t_i) is

$$\begin{aligned} v_i(z) &= v_0, \\ t_i(z) &= t_i(0) + z/v_0. \end{aligned} \tag{D.8}$$

Substituting the above equations to the right-hand side of Eq. (D.7), we obtain a first-order approximation for (v_i, t_i),

$$\begin{aligned} v_i(z) &= v_0 + \frac{e}{mv_0\gamma_0^3} Re\left(\exp(-i\omega t_i(0))\int_0^z dz' E_z(r_i,z')\exp(-i\omega z'/v_0)\right), \\ t_i(z) &= t_i(0) + \frac{z}{v_0} - \frac{e}{mv_0^3\gamma_0^3}\times \\ &\quad Re\left(\exp(-i\omega t_i(0))\int_0^z dz'\int_0^{z'} dz'' E_z(r_i,z'')\exp(-i\omega z''/v_0)\right) \end{aligned} \tag{D.9}$$

Substituting the above equations to Eq. (D.5), we obtain

$$\begin{aligned}
\tilde{P}_b &= I_0 \int_{-\infty}^{\infty} dz < E_z^*(r_i, z) \exp(i\omega(t_i(0) + z/v_0)) \times \\
&\quad [1 - i\omega \frac{e}{mv_0^3\gamma_0^3} Re(\exp(-i\omega t_i(0)) \times \\
&\quad \int_0^z dz' \int_0^{z'} dz'' E_z(r_i, z'') \exp(-i\omega z''/v_0))] > \\
&= I_0 \int_{-\infty}^{\infty} dz \exp(i\omega z/v_0) < E_z^*(r_i, z) \exp(i\omega t_i(0)) > \\
&\quad -i\omega \frac{I_0 e}{mv_0^3\gamma_0^3} \int_{-\infty}^{\infty} dz < E_z^*(r_i, z) \exp(i\omega z/v_0) \exp(i\omega t_i(0)) Re[\\
&\quad \exp(-i\omega t_i(0)) \int_0^z dz' \int_0^{z'} dz'' E_z(r_i, z'') \exp(-i\omega z''/v_0)] > . \quad \text{(D.10)}
\end{aligned}$$

In this case, a DC electron beam enters the cavity. The distribution of the parameter $t_i(0)$ should be uniform. Using

$$< \exp(i\phi) Re[\exp(-i\phi) A] >_\phi = \frac{A}{2}, \quad \text{(D.11)}$$

Eq. (D.10) becomes

$$\begin{aligned}
\tilde{P}_b &= I_0 \int_{-\infty}^{\infty} dz \exp(i\omega z/v_0) < E_z^*(r_i, z) \exp(i\omega t_i(0)) > \\
&\quad -\frac{ieI_0\omega}{2mv_0^3\gamma_0^3} \int_{-\infty}^{\infty} dz \int_{-\infty}^{z} dz' \int_{-\infty}^{z'} dz'' \\
&\quad < E_z^*(r_i, z) E_z(r_i, z'') \exp(i\omega(z - z'')/v_0)] > \\
&= I_0 \int_{-\infty}^{\infty} dz \exp(i\omega z/v_0) < E_z^*(r_i, z) \exp(i\omega t_i(0)) > \\
&\quad -\frac{ieI_0\omega}{2mv_0^3\gamma_0^3} \int_{-\infty}^{\infty} dz \int_{-\infty}^{z} dz' (z - z') \\
&\quad < E_z^*(r_i, z) E_z(r_i, z') \exp(i\omega(z - z')/v_0)] > . \quad \text{(D.12)}
\end{aligned}$$

In this equation, the origin(0) is moved to $-\infty$. The first term of the right-hand side is dominant when the electron beam is bunched. This term is 0 for the input cavity. The second term of the right-hand side corresponds to the beam conductance and susceptance.

Variable $\tilde{Q}_b$ is defined as

$$\frac{1}{\tilde{Q}_b} = \frac{\text{second term of} \tilde{P}_b}{\omega_r U} = \frac{P_w}{\omega_r U} \frac{V_g^2}{2P_w} \frac{2}{V_g^2} \tilde{P}_b = \left(\frac{R}{Q_0}\right) \left(\frac{2}{V_g^2} \tilde{P}_b\right), \quad \text{(D.13)}$$

where P_w is the cavity wall loss, V_g is the gap voltage, $R = V_g^2/(2P_w)$ is the shunt impedance, $Q_0 = \omega_r U/P_w$ is the unloaded quality factor. Variable $\tilde{Q}_b$ can be calculated from a frequency-domain code like SUPERFISH.

If the electric field distribution is

$$E_z = \begin{cases} E & 0 < z < d \\ 0 & \text{otherwise,} \end{cases} \tag{D.14}$$

$\tilde{Q}_b$ is calculated analytically as

$$\frac{1}{\tilde{Q}_b} = \left(\frac{R}{Q}\right) \frac{I_0}{V_0} \frac{1}{\gamma_0(\gamma_0+1)} \left(\frac{\sin(\theta_g/2)}{\theta_g/2} - i\frac{\cos(\theta_g/2)}{\theta_g/2}\right) \left(\frac{\sin(\theta_g/2)}{\theta_g/2} - \cos\frac{\theta_g}{2}\right), \tag{D.15}$$

where $V_0 = mc^2(\gamma_0 - 1)/e$ is the beam voltage, $\theta_g = \omega d/v_0$. In this equation, gap voltage(V_g) is defined as $-Ed$.

The reflection coefficient r from the cavity is

$$r = \frac{Z/Z_0 - 1}{Z/Z_0 + 1} = \frac{1/Q_{ext} - i2\Delta f/f_r - 1/Q_0 - 1/\tilde{Q}_b}{1/Q_{ext} + i2\Delta f/f_r + 1/Q_0 + 1/\tilde{Q}_b}, \tag{D.16}$$

where $\Delta f = f_r - f$.

If Q_{ext} is optimized so as to minimize r,

$$\frac{1}{Q_{ext,opt}} = \sqrt{\left(\frac{2\Delta f}{f_r} + Im\frac{1}{\tilde{Q}_b}\right)^2 + \left(\frac{1}{Q_0} + Re\frac{1}{\tilde{Q}_b}\right)^2}. \tag{D.17}$$

If Δf is optimized so as to minimize r,

$$\Delta f_{opt} = f_r - f = -\frac{f_r}{2} Im\frac{1}{\tilde{Q}_b}. \tag{D.18}$$

The reflected power(P_r) and transmitted power(P_t) are

$$P_r = |r|^2 P_{in}, P_t = (1 - |r|^2)P_{in}, \tag{D.19}$$

where P_{in} is the input power. The transmitted power(P_t) is the sum of the cavity-wall loss(P_w) and power transfer to the beam, $P_b = Re\tilde{P}_b$,

$$P_t = P_w + P_b. \tag{D.20}$$

From the definitions of Q_0 and $\tilde{Q}_b$,

$$P_w : P_b = \frac{1}{Q_0} : Re\frac{1}{\tilde{Q}_b}. \tag{D.21}$$

Then, P_b is

$$P_b = P_{in}\frac{4Re(1/\tilde{Q}_b)/Q_{ext}}{(1/Q_{ext} + 1/Q_0 + Re(1/\tilde{Q}_b))^2 + (2\Delta f/f_r + Im(1/\tilde{Q}_b))^2}. \tag{D.22}$$

The gap voltage(V_g) is

$$V_g = \sqrt{8P_{in}\left(\frac{R}{Q}\right)\frac{1/Q_{ext}}{(1/Q_{ext} + 1/Q_0 + Re(1/\tilde{Q}_b))^2 + (2\Delta f/f_r + Im(1/\tilde{Q}_b))^2}}. \tag{D.23}$$

Appendix E

Some Formulae for Poynting Vector

The poynting vector, $\vec{S}$, is defined as $\vec{E} \times \vec{H}$. If the material is isotropic, the following equation is obtained:

$$\frac{\partial}{\partial t}\frac{1}{2}\int dV(\vec{H}\cdot\vec{B}+\vec{E}\cdot\vec{D})+\int dV\vec{E}\cdot\vec{J}+\int d\vec{A}\cdot\vec{S}=0. \qquad \text{(E.1)}$$

From the above equation, we can consider the Poynting vector to be the energy flow density. In stable operation of the klystron, the electric field(E) and the magnetic field(H) are periodic functions of time with period T_0. These fields are expanded to the following Fourier series:

$$\begin{aligned} E &= \sum_{n=-\infty}^{\infty} E_n \exp(-in\omega t), \\ H &= \sum_{n=-\infty}^{\infty} H_n \exp(-in\omega t), \end{aligned} \qquad \text{(E.2)}$$

where $\omega = 2\pi/T_0$. Since the fields are real, we can derive $E_{-n} = E_n^*$ and $H_{-n} = H_n^*$. The components E_n and H_n are

$$\begin{aligned} E_n &= < E\exp(in\omega t) >_t, \\ H_n &= < H\exp(in\omega t) >_t . \end{aligned} \qquad \text{(E.3)}$$

Multiplying E by H, we obtain

$$S = \sum_{n=-\infty}^{\infty} \exp(-in\omega t) \sum_{m=-\infty}^{\infty} E_m H_{m-n}^*. \qquad \text{(E.4)}$$

By taking the average of S with time, we obtain

$$< S >_t = S_0 = \sum_{m=-\infty}^{\infty} E_m H_m^*. \tag{E.5}$$

Since the first harmonics of the fields E_1, H_1, E_{-1}, H_{-1} are much larger than the other harmonics in the cavity, S_0 can be approximated as $S_0 \simeq 2Re(E_1 H_1^*)$. The second harmonic of S is

$$S_2 = \sum_{m=-\infty}^{\infty} E_m H_{m-2}^* \simeq E_1 H_1. \tag{E.6}$$

Thus, if E_1 has the same phase as H_1, the energy flow can be estimated from S_2. In general, this is not true.

The electric field and magnetic field of TM0*0 are

$$\begin{aligned} E_z &= Re\left[(E_a H_0^{(1)}(kr) + E_b H_0^{(2)}(kr))\exp(-i\omega t)\right], \\ H_\phi &= -Re\left[ic\epsilon_0(E_a H_1^{(1)}(kr) + E_b H_1^{(2)}(kr))\exp(-i\omega t)\right]. \end{aligned} \tag{E.7}$$

The poynting vector, $< S_r >_t$, for this wave is

$$\begin{aligned} < S_r >_t &= - < E_z H_\phi >_t \\ &= -\frac{1}{2} Re\left[(E_a H_0^{(1)}(kr) + E_b H_0^{(2)}(kr))(ic\epsilon_0)(E_a^* H_1^{(2)}(kr) + E_b^* H_1^{(1)}(kr))\right] \\ &= \frac{-ic\epsilon_0}{4}(|E_a|^2 - |E_b|^2)(H_0^{(1)}(kr)H_1^{(2)}(kr) - H_0^{(2)}(kr)H_1^{(1)}(kr)) \\ &= \frac{c^2\epsilon_0(|E_a|^2 - |E_b|^2)}{\pi\omega r}. \end{aligned} \tag{E.8}$$

The energy flow(P) is

$$P = 2\pi r d < S_r >_t = \frac{2c^2 d}{\omega}\epsilon_0(|E_a|^2 - |E_b|^2), \tag{E.9}$$

where d is the width of the cell.

Appendix F

Derivation of Courant Stability Criterion

We will derive the Courant stability criterion for TM0 waves. Maxwell equations for TM0 waves with the cylindrical coordinates (r, ϕ, z) are

$$\begin{aligned} \mu\frac{\partial H_\phi}{\partial t} &= -\frac{\partial E_r}{\partial z} + \frac{\partial E_z}{\partial r}, \\ \epsilon\frac{\partial E_r}{\partial t} &= -\frac{\partial H_\phi}{\partial z}, \\ \epsilon\frac{\partial E_z}{\partial t} &= \frac{1}{r}\frac{\partial}{\partial r} r H_\phi. \end{aligned} \tag{F.1}$$

Substituting the difference quotients for derivatives, we obtain the following equations:

$$\begin{aligned} H_\phi^{n+1/2}(k+1/2, l+1/2) &= H_\phi^{n-1/2}(k+1/2, l+1/2) \\ &\quad -\frac{\Delta t}{\mu\Delta z}(E_r^n(k+1, l+1/2) - E_r^n(k, l+1/2)) \\ &\quad +\frac{\Delta t}{\mu\Delta r}(E_z^n(k+1/2, l+1) - E_z^n(k+1/2, l)), \\ E_r^n(k, l+1/2) &= E_r^{n-1}(k, l+1/2) \\ &\quad -\frac{\Delta t}{\epsilon\Delta z}(H_\phi^{n-1/2}(k+1/2, l+1/2) \\ &\quad -H_\phi^{n-1/2}(k-1/2, l+1/2)), \\ E_z^n(k+1/2, l) &= E_z^{n-1}(k+1/2, l) \end{aligned}$$

$$
\begin{aligned}
&+\frac{\Delta t}{\epsilon l \Delta r}((l+1/2)H_\phi^{n-1/2}(k+1/2,l+1/2) \\
&\quad -(l-1/2)H_\phi^{n-1/2}(k+1/2,l-1/2)) \\
\simeq\ & E_z^{n-1}(k+1/2,l) \\
&+\frac{\Delta t}{\epsilon \Delta r}(H_\phi^{n-1/2}(k+1/2,l+1/2) \\
&\quad -H_\phi^{n-1/2}(k+1/2,l-1/2)), \qquad \text{(F.2)}
\end{aligned}
$$

where $E_r^n(k,l+1/2)$ is the radial component of the electric field at $(z = k\Delta z, r = (l+1/2)\Delta r; time = n\Delta t)$, and so on. We assume that a plane wave propagates in space as follows:

$$
\begin{aligned}
H_\phi^{n+1/2}(k+1/2,l+1/2) &= H_\phi^{n+1/2}\exp(ikk_z\Delta z + ilk_r\Delta r), \\
E_r^n(k,l+1/2) &= E_r^n \exp(i(k-1/2)k_z\Delta z + ilk_r\Delta r), \\
E_z^n(k+1/2,l) &= E_z^n \exp(ikk_z\Delta z + i(l-1/2)k_r\Delta r), \qquad \text{(F.3)}
\end{aligned}
$$

Substituting the above equations into Eq. (F.2), we obtain

$$
\begin{aligned}
H_\phi^{n+1/2} &= H_\phi^{n-1/2}\left(1-\frac{4v^2\Delta t^2}{\Delta z^2}\sin^2\frac{k_z\Delta z}{2}-\frac{4v^2\Delta t^2}{\Delta r^2}\sin^2\frac{k_r\Delta r}{2}\right) \\
&\quad -E_r^{n-1}\frac{2i\Delta t}{\mu\Delta z}\sin\frac{k_z\Delta z}{2}+E_z^{n-1}\frac{2i\Delta t}{\mu\Delta r}\sin\frac{k_r\Delta r}{2}, \\
E_r^n &= E_r^{n-1}-H_\phi^{n-1/2}\frac{2i\Delta t}{\epsilon\Delta z}\sin\frac{k_z\Delta z}{2}, \\
E_z^n &= E_z^{n-1}+H_\phi^{n-1/2}\frac{2i\Delta t}{\epsilon\Delta r}\sin\frac{k_r\Delta r}{2}, \qquad \text{(F.4)}
\end{aligned}
$$

where $v = 1/\sqrt{\epsilon\mu}$. The above equations are rewritten with a matrix A.

$$
\begin{aligned}
\vec{x}_n &= A\vec{x}_{n-1}, \\
A &= \begin{pmatrix}
1 & 0 & -\frac{2i\Delta t}{\epsilon\Delta z}\sin\frac{k_z\Delta z}{2} \\
0 & 1 & \frac{2i\Delta t}{\epsilon\Delta r}\sin\frac{k_r\Delta r}{2} \\
-\frac{2i\Delta t}{\mu\Delta z}\sin\frac{k_z\Delta z}{2} & \frac{2i\Delta t}{\mu\Delta r}\sin\frac{k_r\Delta r}{2} & 1-\frac{4v^2\Delta t^2}{\Delta z^2}\sin^2\frac{k_z\Delta z}{2}-\frac{4v^2\Delta t^2}{\Delta r^2}\sin^2\frac{k_r\Delta r}{2}
\end{pmatrix}, \qquad \text{(F.5)}
\end{aligned}
$$

where $\vec{x}_n = (E_r^n, E_z^n, H_\phi^{n+1/2})^T$. Eigenvalues λ of the matrix A are,

$$
\lambda = 1, 1-\alpha \pm \sqrt{(1-\alpha)^2-1}, \qquad \text{(F.6)}
$$

where

$$\alpha = 2v^2\Delta t^2\left(\frac{\sin^2(k_z\Delta z/2)}{\Delta z^2} + \frac{\sin^2(k_r\Delta r/2)}{\Delta r^2}\right).$$

The absolute values of the eigenvalues λ should be 1 ($0 \leq \alpha \leq 2$) for any k_z, k_r in order that the simulation be stable. Thus, we find

$$v\Delta t \leq \frac{1}{\sqrt{(1/\Delta z)^2 + (1/\Delta r)^2}}. \tag{F.7}$$

This is the Courant stability criterion for TM0 waves.

Appendix G

Derivation of Eq. (4.8)

Assume that there is a TM0*0 wave on axis in a pillbox cavity. This wave propagates in the radial direction with velocity c. At the coupler($r = a$), this wave is reflected with reflection coefficient s. The wave returns to the axis. Thus, the wave is reduced by the factor $|s|$ in a round-trip time of $2a/c$. On the other hand, The amplitude reduces as $\exp(-\omega t/2Q)$ with time, where ω is the frequency and Q is the quality factor. We thus find

$$|s| = \exp(-\omega a/(Qc)). \tag{G.1}$$

Rearranging the above equation, we obtain

$$Q = -\frac{\omega a}{c \ln |s|}. \tag{G.2}$$

Appendix H

Estimation of the Kick Angle by the TE111 Mode in the Output Structure

In our case the velocity of the electrons is about $0.8c$ at the entrance of the output structure, and about 45% of the electron energy are converted to RF energy. For simplicity, we assume that the velocity(v) of the electrons does not have any transverse component and that v depends only on the longitudinal position(z). Dipole wakefunctions $W_{\parallel}, W_x$ are defined as

$$\begin{aligned} -W_{\parallel}(t_0)x_0 x &= \frac{1}{e}\int_{-\infty}^{\infty} dz E_z(x,z,t=t_0+\int^z \frac{dz}{v(z)}), \\ W_x(t_0)x_0 &= \frac{c}{e}\int_{-\infty}^{\infty} \frac{dz}{v(z)}(E_x - v(z)B_y)(x,z,t=t_0+\int^z \frac{dz}{v(z)}), \end{aligned} \quad \text{(H.1)}$$

where x_0, x are the transverse displacements of the leading particle and the trailing particle, respectively. Using the equation $\partial E_z/\partial x = \partial E_x/\partial z + \partial B_y/\partial t$, we obtain

$$\begin{aligned} & \frac{\partial}{\partial x}\int_{-\infty}^{\infty} dz E_z(x,z,t=t_0+\int^z \frac{dz}{v(z)}) \\ = & \int_{-\infty}^{\infty} dz \left(\frac{\partial E_x}{\partial z} + \frac{\partial B_y}{\partial t}\right)(x,z,t=t_0+\int^z \frac{dz}{v(z)}) \\ = & \int_{-\infty}^{\infty} dz \left(-\frac{1}{v(z)}\frac{\partial E_x}{\partial t_0} + \frac{\partial B_y}{\partial t_0}\right)(x,z,t=t_0+\int^z \frac{dz}{v(z)}) \end{aligned}$$

$$= -\frac{\partial}{\partial t_0}\int_{-\infty}^{\infty}\frac{dz}{v(z)}(E_x - v(z)B_y)(x,z,t=t_0+\int^z\frac{dz}{v(z)}). \quad \text{(H.2)}$$

From the above equation we find the Panofsky-Wenzel relation:

$$W_\parallel(t_0) = \frac{1}{c}\frac{d}{dt_0}W_x(t_0). \quad \text{(H.3)}$$

The impedances of the wake functions are defined as

$$\begin{aligned} Z_\parallel(\omega) &= \int_{-\infty}^{\infty} dt W_\parallel(t)\exp(i\omega t), \\ Z_x(\omega) &= -i\int_{-\infty}^{\infty} dt W_x(t)\exp(i\omega t). \end{aligned} \quad \text{(H.4)}$$

From the Panofsky-Wenzel relation we obtain

$$Z_\parallel(\omega) = \frac{\omega}{c}Z_x(\omega). \quad \text{(H.5)}$$

Based on an analogy of the impedance of a monopole field, $Z_\parallel$ is

$$\begin{aligned} Z_\parallel &= \frac{R_\parallel}{1 - iQ_0(\omega/\omega_r - \omega_r/\omega)}, \\ R_\parallel &= \frac{\left|\frac{\partial}{\partial x}\int E_z(x,z,t=t_0+\int^z\frac{dz}{v(z)})dz\right|^2}{2P}, \end{aligned} \quad \text{(H.6)}$$

where Q_0, ω_r, P are the unloaded quality factor, the resonant frequency of the dipole mode, the wall loss, respectively. The impedance Z_x is

$$\begin{aligned} Z_x &= \frac{R_x\omega_r/\omega}{1 - iQ_0(\omega/\omega_r - \omega_r/\omega)}, \\ R_x &= \frac{c\left|\frac{\partial}{\partial x}\int E_z(x,z,t=t_0+\int^z\frac{dz}{v(z)})dz\right|^2}{2P\omega_r} \\ &= \frac{c}{2P\omega_r}\left|\frac{\partial}{\partial x}\int_{-\infty}^{\infty} dz E_z(x,z)\exp\left(-i\omega\int^z\frac{dz}{v(z)}\right)\right|^2. \end{aligned} \quad \text{(H.7)}$$

The shunt impedances divided by the unloaded quality factor R_x/Q for XOUT#105 and XOUT#105m29 are shown in Figure H.1.

The TE111 mode is excited if the electron beam traverses the cavity with some tansverse displacement, or if the reflection coefficients at the two ends of the rectangular waveguides are different.

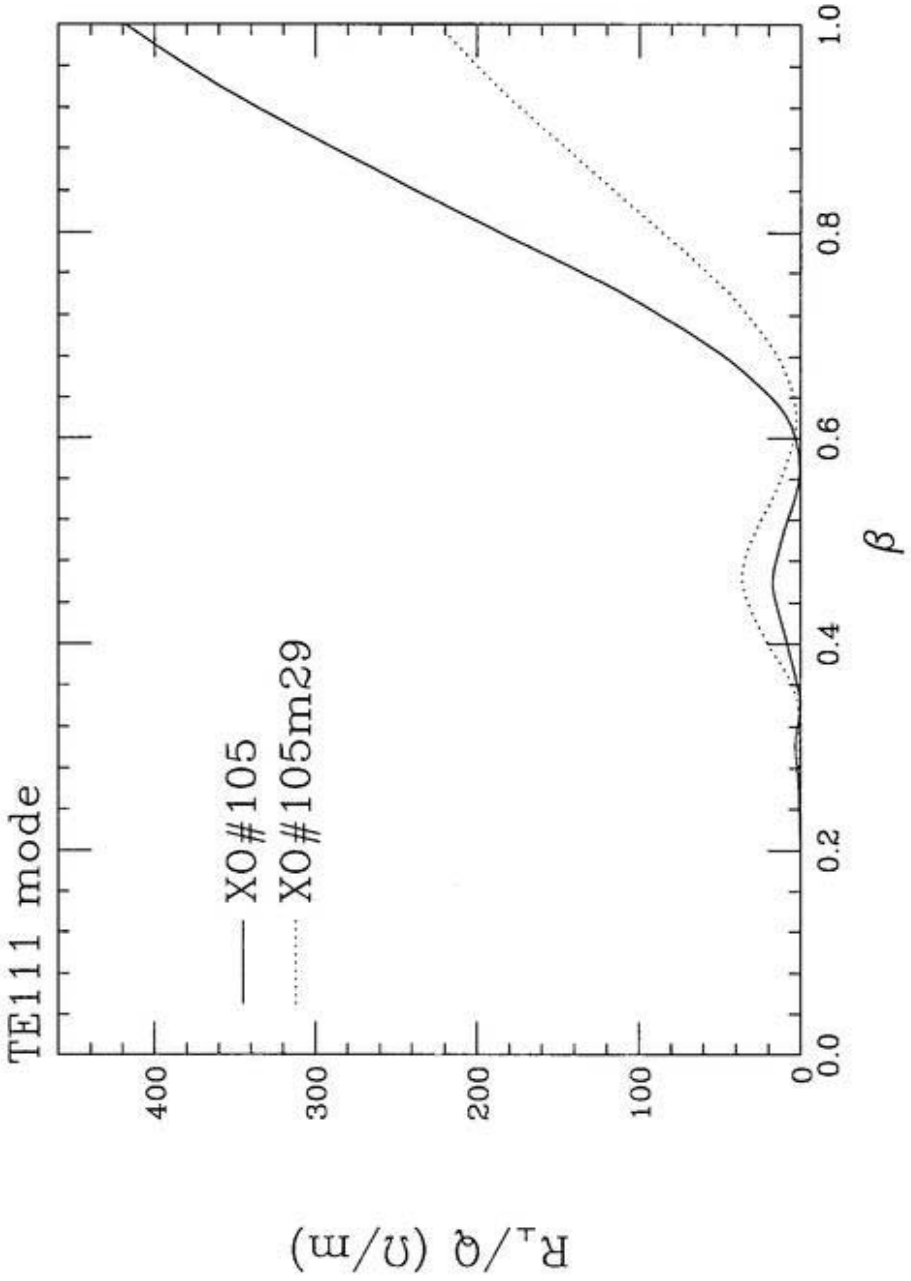

Figure H.1: Transverse shunt impedances of the TE111 modes of XOUT#105 and XOUT#105m29.

If an electron beam having a current $I\exp(-i\omega t)$ traverses the cavity with the tansverse displacement(x_0), the transverse momentum(Δp_x) is

$$\Delta p_x = \frac{1}{c}\int eI\exp(-i\omega t)W_x(t)x_0 dt = -ieIx_0 Z_x^*(\omega)/c. \tag{H.8}$$

The transverse kick angle(x') is

$$x' \leq \frac{(\Delta p_x)_{max}}{p} \leq \frac{2I}{pc/e}\frac{(R_x/Q_0)x_0}{\sqrt{(1/Q_L)^2+(2\Delta f/f)^2}}. \tag{H.9}$$

From a HFSS calculation, the loaded quality factor(Q_L) is about 160. The current(I) is 490 A. The cathode voltage is 550 kV. If the efficiency is 50%, the average electron beam energy at the collector is 275 kV. In this case pc/e = 600 kV. For XO#105, Δf = 200 MHz, $R_x/Q \leq 420\Omega$/m. For XO#105m29, Δf = 500 MHz, $R_x/Q \leq 224\Omega$/m. We assume that the transverse displacement of the beam x_0 is 1mm. Substituting these values to the above equation, we obtain

$$x' \leq \begin{cases} 19\text{mrad} & (\text{XO\#105}) \\ 4.2\text{mrad} & (\text{XO\#105m29}). \end{cases} \tag{H.10}$$

There are some reflections from the RF windows and the dummy loads. The reflection was estimated to be at most 0.16. If the output power is 120 MW, reflected power(P_{in}) is less than 3 MW. The transmitted power(P_t) into the output structure is estimated to be

$$P_t = \frac{P_{in}}{1+(Q_{ext}\Delta f/f)^2} \leq \begin{cases} 93\text{kW} & (\text{XO\#105}) \\ 15\text{kW} & (\text{XO\#105m29}). \end{cases} \tag{H.11}$$

The transverse kick is

$$\begin{aligned} x' &\leq \frac{e}{p}\sqrt{\frac{2P_t(R_x/Q)Q_{ext}}{\omega_r}} \\ &\leq \begin{cases} 17\text{mrad} & (\text{XO\#105}) \\ 5.0\text{mrad} & (\text{XO\#105m29}). \end{cases} \end{aligned} \tag{H.12}$$

For XO#105m29, the kick angle is so small that the electrons may not hit the wall until they reaching the collector.

Bibliography

[1] M. Abramowitz and I. A. Stegun, "Handbook of Mathematical Functions",Dover, (1972).

[2] Y.H. Chin, "Modeling and Design of Klystron", LINAC98, (1998).

[3] S. H. Gold and G. S. Nusinovich, "Review of high-power microwave source research", Rev. Sci. Instrum. 68, 3945-3974 (1997).

[4] "JLC Design Study", KEK Report 97-1, 364-372 (1997).

[5] S. Kazakov, "One method of output structure simulation", RF93, 161-166 (1993).

[6] W. D. Kilpatrick, Rev. Sci. Instrum. 28, 824 (1957).

[7] T. L. Lavine et al.,"Transient analysis of multicavity klystrons", SLAC-PUB-4719 (1988).

[8] Bruce Goplen et al., "MAGIC USER'S MANUAL", Mission Research Corporation, MRC/WDC-R-409 (1997).

[9] S. Matsumoto et al., "Simulation study of the bunching section of X-band klystrons", LINAC98, (1998).

[10] S. Michizono et al., "Electron gun simulation using MAGIC", LINAC98, (1998).

[11] H.Mizuno, J. Odagiri and T. Higo, "X-band klystron diode test for Japan Linear Collider", Proc. 14th International Conference on High Energy Accelerators, 1125 (1989).

[12] T. Shintake, "Nose-Cone Removed Pillbox Cavity for High-Power Klystron Amplifiers", IEEE Transactions on Electron Devices, vol. 38 no. 4 917, (1991).

[13] T. Shintake, "FCI (Field Charge Interaction) program for high power klystron simulations", KEK-PREPRINT-89-18, (1989).

[14] J. C. Slater, "Microwave Electronics", D. Van Nostrand Co., Inc, (1950).

[15] S. Yu, "Particle-in-cell simulations of high power klystrons" , SLAC/AP-34, (1984).

[16] V.E. Teryaev, "DISKLY Code for Calculation and Optimization of Klystrons"

[17] http://www.cst.de

[18] G. A. Westenskow and T. L. Houck, IEEE Trans. Plasma Sci. 22, 750 (1994).

[19] P. B. Wilson, SLAC-PUB-3674 (1985).